DISSERTATION

THE EFFECTS OF POINT DEFECTS AND MICROSTRUCTURE ON THE PSEUDO-ELASTICITY OF $THCR_2SI_2$-TYPE CRYSTALS

Submitted by

Ian Nathaniel Bakst

Department of Mechanical Engineering

In partial fulfillment of the requirements

For the Degree of Doctor of Philosophy

Colorado State University

Fort Collins, Colorado

Fall 2018

Doctoral Committee:

Advisor: Christopher R. Weinberger

Kaka Ma
James R. Neilson
Donald W. Radford

ABSTRACT

THE EFFECTS OF POINT DEFECTS AND MICROSTRUCTURE ON THE PSEUDO-ELASTICITY OF $THCR_2SI_2$-TYPE CRYSTALS

Ternary intermetallic compounds with the $ThCr_2Si_2$-type structure, which are known for their high-temperature superconductivity, have recently garnered interest due to the discovery of a pseudo-elastic mechanical response to compression along the c-axis. However, the effects of point defects and doping on this response remain unknown. In this work, these effects are investigated with density functional theory (DFT) in conjunction with continuum-scale models. DFT simulations of hydrostatic and uniaxial compression of pure $ThCr_2Si_2$-type crystals were conducted. The magnetic phase transition of $CaFe_2As_2$ was reproduced, while $LaRu_2P_2$ exhibited a continuous transition into its collapsed tetragonal phase. The two-phase DFT data was used to build a continuum-scale, thermodynamically-driven composite model which predicts the pseudo-elastic response of a large sample under displacement control and load control scenarios. Strain along the c-axis was shown to be the critical parameter in predicting crystal collapse. Then, DFT simulations of defected or doped unit cells were conducted to investigate their energetics and mechanical responses to compression. In some cases, the addition of vacancies effectively suppressed the pseudo-elastic response of the crystals. Simulations of crystals doped with varying concentrations revealed alterations of the mechanical properties as well. Tunable variability of the phase change with respect to dopant concentration was predicted in disordered doped structures, while multiple phase changes were predicted in ordered doped structures. Composite models were then built with the DFT data to predict the response of a sample comprised of multiple microstructures. The models predict a wide range of variability in the mechanical behavior and provide insight into how impurities and defects can be used to tune the response of these materials.

ACKNOWLEDGEMENTS

This work would not be possible without the vision and guidance of my advisor, Dr. Christopher Weinberger. Thanks to the members, past and present of the Advanced Computational Materials Engineering (ACME) Lab at CSU, especially Matthew Guziewski and Hang Yu. We've been through the trenches together, and I'm proud to call you my friends. Thanks to the members of my committee: Dr. Kaka Ma, Dr. James Neilson, and Dr. Donald Radford. Their input helped make this work the best it could be.

Experimental investigations of $CaFe_2As_2$ and $LaRu_2P_2$ presented in this work were performed at the University of Connecticut. Microcompression experiments were performed by Dr. Seok-Woo Lee and his team of graduate students: Keith J. Dusoe, and Keara G. Frawley, and John T. Sypek. Transition Electron Microscopy was performed by Dr. Mark Aindow and his graduate student, Sriram Vijayan.

This work utilized the RMACC Summit supercomputer, which is supported by the National Science Foundation (awards ACI-1532235 and ACI-1532236), the University of Colorado Boulder and Colorado State University. The RMACC Summit supercomputer is a joint effort of the University of Colorado Boulder and Colorado State University. We gratefully acknowledge the support of NVIDIA Corporation with the donation of the Titan X Pascal GPU used for this research.

Some of the results presented in this document were previously published in the following articles:

• Bakst, I. N., Sypek, J. T., Neilson, J. R., Lee, S. W., & Weinberger, C. R. Modeling pseudoelastic behavior in small-scale $ThCr_2Si_2$-type crystals. *Computational Materials Science* **150**, 86–95 (2018).

• Bakst, I. N., Dusoe, K. J., Drachuck, G., Neilson, J. R., Canfield, P. C., Lee, S. W., & Weinberger, C. R. Effects of point defects on the mechanical response of $LaRu_2P_2$. *Acta Materialia* **160**, 224–234 (2018).

• Frawley, K.G., Bakst, I., Sypek, J.T., Vijayan, S., Weinberger, C.R., Canfield, P.C., Aindow,

M. & Lee, S.W. A Nanoindentation study of the plastic deformation and fracture mechanisms in single-crystalline $CaFe_2As_2$. *JOM* **70**, 1–7 (2018).

DEDICATION

To Katie, you helped me find the strength to continue at times I thought I couldn't. And to my loving family, you have seemingly endless wells of experience, wisdom and patience.

TABLE OF CONTENTS

LIST OF TABLES

LIST OF FIGURES

Chapter 1

Introduction

1:2:2 intermetallic compounds with the $ThCr_2Si_2$-type crystal structure have garnered recent interest due to their superconducting properties. Dozens of these compounds exhibit superconductivity at temperatures as high as 38 K [1]. Efforts to increase their superconducting critical temperatures (T_c) have led to studies of compression and doping of these materials. Doping is highly effective in increasing superconductive critical temperatures and several investigations involving doping of these materials have uncovered alterations to their electronic properties [2, 3]. Similarly, studies of the introduction of point defects via proton irradiation have revealed similar electronic changes. Hydrostatic compression has also been shown to increase the critical temperature.

When compressed along the c-axis, these materials may undergo phase changes which facilitate shape memory effects and pseudo-elasticity. Both magnetic and nonmagnetic 1:2:2 compounds can exhibit this pseudo-elasticity, and the inter-relationship between electronic and mechanical properties is complex. To this point, very little work has investigated this inter-relationship, and the effect which point defects may have on the mechanical properties of $ThCr_2Si_2$-type crystals. In that light, this work seeks to address the following questions:

1. What chemical factors are responsible for phase changes in $ThCr_2Si_2$-type crystals?

2. How does the compression response of a single unit cell translate into the response of a macro-scale sample?

3. What are the effects of point defects (vacancies and interstitials) on the mechanical response of $ThCr_2Si_2$-type crystals?

4. What are the effects of alloying and doping on the mechanical response of $ThCr_2Si_2$-type crystals?

Chapter 2

Background

2.1 The $ThCr_2Si_2$ Crystal Structure

The 1:2:2 intermetallic compounds which have the $ThCr_2Si_2$ crystal structure are a widely studied class of materials. These compounds were first discovered in 1963 [4] and with over 700 reported compounds [5], it has been suggested that more compounds form this crystal structure than any other known structure [6]. Interest was furthered by the discovery of superconductivity within this class of materials with the initial discovery occurring in $CeCu_2Si_2$ [7], followed shortly thereafter by discovery in the lanthanum-based compounds [8]. Two sub-classes of these compounds, the iron-pnictides and the iron-chalcogenides, are of particular importance because they have notably high superconducting critical temperatures (as high as 38 K) [1]. This has garnered significant interest since these materials form a class of superconductors with over 30 known examples [9, 10]. It was later discovered that it is possible to enhance the superconductivity in these compounds through the application of hydrostatic pressure [11], including increasing the superconducting temperature of $LaRu_2P_2$ from 3.8 K to 5.8 K under hydrostatic compression [12]. However, it was found that above a certain pressures, the superconductivity disappears entirely [13]. $LaRu_2P_2$ had the highest superconducting temperature ($T_c = 4$ K) of the 1:2:2 compounds before the discovery of superconductivity in doped iron-pnictides [14, 15]. $BaFe_2As_2$, when doped with potassium, has been observed to exhibit superconductivity as high as 38 K [1].

Further investigations of this behavior [16] uncovered phase transitions which were suggested by Hoffmann and Zheng [17], who highlighted the importance of the vertical bond length between $[Mn_2P_2]$ layers in AMn_2P_2 compounds. They pointed out that some compounds exist in crystal structures with P–P distances greater than the standard P–P covalent bond length, while others have distances which are shorter. This crystal structure, shown in Figure 1(a), has a tetragonal unit cell with its vertical c-axis at least twice as long as its a-axis, and can be thought of as alternating layers

of A cations and B_2X_2 anion cages [17]. These crystals are typically comprised of a low-valency metal (such as an alkali metal, alkaline earth metal, or a rare earth metal), a transition metal, and a nonmetal or metalloid. Note that the layered structure creates an X–X bond length that can be equal to or exceed the covalent bond length. This suggests that it is possible in some of these compounds to create covalent bonds between the X atoms by compressing the crystal structure along its c-axis. If the competition between the Coulombic interactions and covalent bonding is such that a local minima exists at the covalent bond length, then a phase transition is possible resulting in a collapsed version of the $ThCr_2Si_2$ crystal structure. This c-axis collapse can give rise to potential shape memory effects, and a pseudo-elastic (sometimes referred to as superelastic) mechanical response to compression along the c-axis [12, 16, 18, 19].

The conventional unit cell of the $ThCr_2Si_2$-type crystal structure is a body-centered tetragonal cell with 10 atoms (Figure 1(a)). However, the structure can be represented with a primitive unit cell of only 5 atoms (Figure 1(c)). This unit cell is triclinic and contains one A-type atom, and two B- and X-type atoms. Thus, all A-type sites are symmetrically equivalent, and due to the symmetry of the primitive cell, all B-type sites are symmetrically equivalent and all X-type sites are symmetrically equivalent. Some compounds, such as $CaFe_2As_2$ (which will be discussed in more detail in Section 2.1.1), exist in a distorted form of this crystal structure. Magnetism can cause a small distortion of the lattice along the $\langle 110 \rangle$ direction of the tetragonal unit cell. These distortions cause the conventional unit cell to be a face-centered orthorhombic cell containing 20 unit cells (Figure 1(b)). The space groups and Wyckoff positions of both the tetragonal and orthorhombic unit cells are tabulated in Table 1.

2.1.1 Phase Changes in $CaFe_2As_2$

In the iron-based $ThCr_2Si_2$ compounds, antiferromagnetic ordering of the magnetic moments on the iron atoms is commonly observed at low temperatures [11]. Magnetic ordering has been observed for iron-arsenides with this structure including $CaFe_2As_2$ [11, 20], $BaFe_2As_2$ [20, 21], $SrFe_2As_2$ [3, 21], and KFe_2As_2 [22, 23]. $CaFe_2As_2$ (Figure 2) is arguably the most well-studied

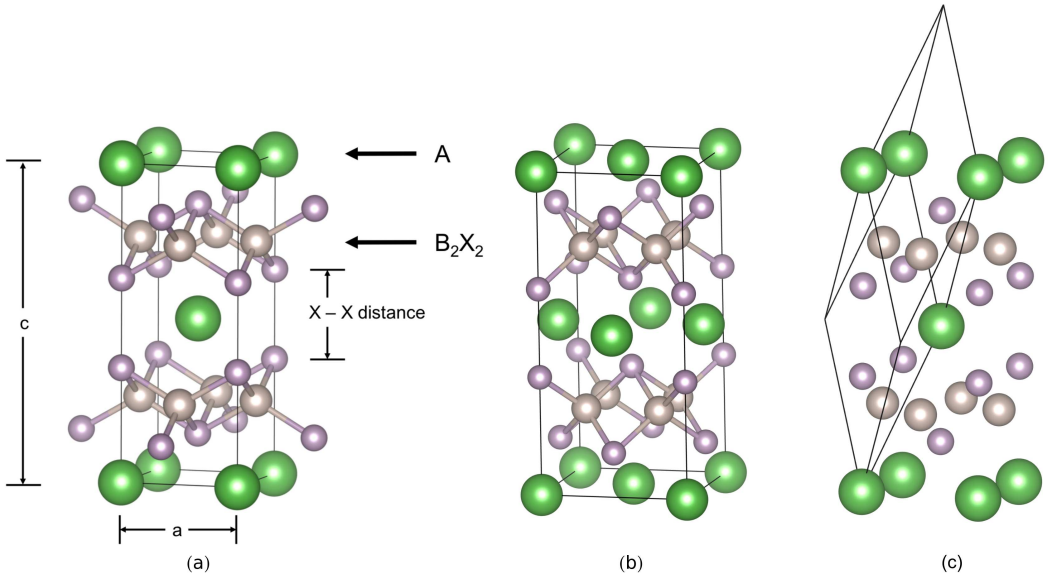

Figure 1: (a) The $ThCr_2Si_2$ crystal structure has a tetragonal unit cell with alternating layers of A and B–X. The original identified structure has a tetragonal unit cell, whose c-axis is at least twice as long as the side-length [4]. The distance between vertically-stacked X atoms is instrumental determining if the compound can exhibit a pseudo-elastic response. (b) Many compounds, including $CaFe_2As_2$, exist in a distorted variant of this lattice with an orthorhombic cell of 20 atoms. (c) The crystal structure can be described by its primitive unit cell which contains only 5 atoms.

of these compounds [11, 24, 25]. The ordering of the magnetic moments causes the diagonals of the base of the tetragonal cell (Figure 1(a)) to expand unequally. The resulting lattice distortion changes the crystal structure from body-centered tetragonal to a face-centered orthorhombic (Figure 3(b)). Above the Néel temperature, the magnetic moments randomize, eliminating the structural differences between the a and b axes of the orthorhombic crystal, resulting in a phase change from low temperature orthorhombic back to the tetragonal crystal structure. Three different phases of $CaFe_2As_2$ have been identified as a function of temperature and pressure, as shown in Figure 3(a). At low temperatures and pressures, antiferromagetic ordering dominates and the crystal structure is orthorhombic. Above the Néel temperature, which is roughly 170 K for $CaFe_2As_2$ [16, 27, 28], the material becomes paramagnetic and the crystal structure transforms to tetragonal. However, at high pressures, the crystal structure collapses along the c-axis and the tetragonal unit cell becomes significantly shorter [29] and the crystal becomes non-magnetic. Sim-

Table 1: Crystal symmetry parameters and atomic Wyckoff positions of the two possible conventional unit cells of $ThCr_2Si_2$-type crystals.

Structure	Space Group	Atomic (Wyckoff) Positions
Tetragonal	I4mm	A1 (0.0, 0.0, 0.0) B1 (0.0, 0.5, 0.25) X1 (0.0, 0.0, -0.36)
Orthorhombic	Fmm2	A1 (0.0, 0.0, 0.0) B1 (0.25, 0.25, 0.25) X1 (0.36, 0.0, 0.0)

ilar magnetic ternary compounds also exhibit similar magnetic phase transitions such as $BaFe_2As_2$. Interestingly, this compound undergoes two phase transitions as a function of stress (uniaxial and hydrostatic) [30].

2.2 Shape Memory Alloys

The traditional origin of pseudo-elasticity arises from shape memory effects (SMEs) which are commonly observed responses of shape memory alloys (SMAs). SMAs are a special class of materials which can undergo stress-induced diffusionless phase transformations, commonly referred to as martensitic phase transformations. At low temperatures, these materials exist in a twinned-martensite phase. This twinned-martensite phase is a result of cooling from the high-symmetry austenite phase after formation. Upon loading, the part accommodates the applied strain through detwinning of this martensite phase. When the crystal is unloaded, the SMA remains in the detwinned-martensite state until heat is applied. If the SMA is brought above its phase-transition temperature, the detwrinned-martensite transitions to austenite, which brings the part back to its original undeformed shape.

Past yield, the primary mechanism by which these alloys accommodate the strain is not by slip, but instead by a phase transformation in which coordinated atoms move slightly, but do not diffuse. Nickel-titanium alloys (often called Nitinol), are the classic SMAs. The stable NiTi crystal structure is B2, which can be thought of as a BCC unit cell where the center atom is one element, while the corner atom is the other (Figure 4a). Under stress, the crystal shears into a similar

Figure 2: A crystal of $CaFe_2As_2$ utilized in a nanoindentation study of plastic deformation [26].

structure with an orthorhombic unit cell, known as the B19 structure (Figure 4b). While these phases may be similar, the transition between them is an avenue to accommodate strain without plastic deformation. Upon heating (with stress no longer applied), the thermal energy facilitates a phase transformation back to the original B2 phase, and thus the part “remembers" its original shape. This is the mechanism behind the shape memory effect.

This effect has been known for years and is useful in the development of solid-state actuators. Above a critical temperature, there is enough thermal kinetic energy for the material to return to its original phase upon unloading. If the loading and unloading take place above this critical temperature, the phase transition happens instantaneously, and the observed stress-strain response has a softening region, with high recoverable strains. While, highly anisotropic, recoverable strains for NiTi alloys (in certain crystallographic directions) have been reported as high as 13%. This was reported for tension in the $\langle 100 \rangle$ direction of Ni(36.8%)Al alloys [32]. Meanwhile, NiTi has been observed to exhibit recoverable strains as high as 10.5% [33].

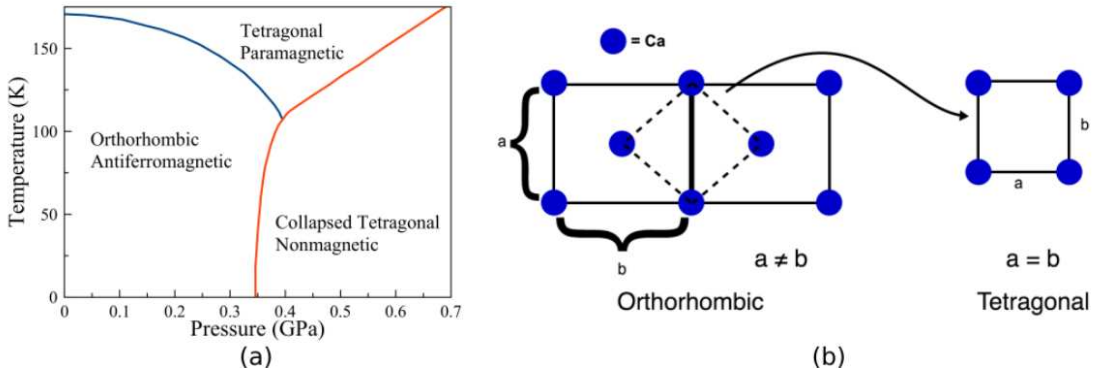

Figure 3: The pressure-temperature phase diagram of $CaFe_2As_2$ [16] (a) shows the low-temperature, low-pressure orthorhombic phase, the high-temperature, low-pressure tetragonal phase, and the high-pressure collapsed tetragonal phase. (b) Upon the loss or randomization of the magnetic moments, the a and b axes of the orthorhombic unit cell will become equal in length, resulting in a transition to a tetragonal unit cell (viewed down the c-axis of the crystal).

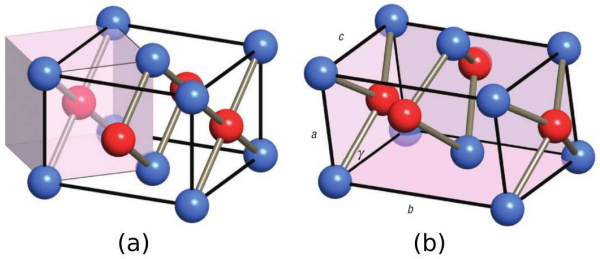

Figure 4: The martensitic phase transformation between the B2 structure (a) and the orthorhombic B19 structure (b) is responsible for the shape memory effects of NiTi (reproduced from [31]).

2.2.1 Dimensional Stability

These shape memory effects, are not entirely reversible. Classic shape memory alloys often exhibit fatigue damage after several shape-memory cycles. This definition of fatigue is somewhat adapted from its definition for conventional materials [34, 35]. Fatigue in SMAs can occur by one or more of multiple mechanisms. The part may fail by conventional fracture, it may lose its mechanical or shape memory properties due to thermal (phase transition) cycling, or it may lose these properties through thermal cycling under applied stress [36]. This lack of dimensional stability significantly reduces the operating life and reliability of SMAs.

2.3 Pseudo-Elasticity

Pseudo-elasticity, also known as superelasticity, is the large-strain elastic response of a material enabled by a phase transition and is often associated with a shape memory behavior. The largest class of pseudo-elastic and shape memory materials are shape memory alloys (SMAs) which undergo a martensitic phase transformation under applied stress [37, 38] which facilitates the pseudo-elastic response. Upon unloading at low temperatures, the SMA is kinetically limited from returning to its original phase (in observable timeframes) and thus the material remains in the deformed configuration. However at sufficiently high temperatures, there is enough thermal energy present for the material to transition back into its original phase upon unloading giving rise to a shape-memory behavior. In contrast, if the loading and unloading are both done at sufficiently high temperatures, there is no barrier for the reverse transformation and the material is able to directly transform when the load is removed without external stimuli. 1:2:2 superconductors behave in a similar fashion, albeit through a rather unique phase transition and thus many of the tools used to describe SMAs can be used to understand these materials as well.

2.4 The Pseudo-Elastic Response in $ThCr_2Si_2$ Crystals

Interest in the response of $ThCr_2Si_2$ crystals to applied stress was first by Zheng and Hoffmann [17]. This groundbreaking work investigated the electronic band structure within the crystal. By analyzing the band structure between the B–X layers, along with Nobel Prize-winning intuition, one could speculate that there are competing bonding forces between the vertically stacked X atoms. Specifically looking at the case of $[Mn_2P_2]$ layers, the Coulombic repulsion between P atoms competes with the attraction of bonding at the P–P bond length of 2.8 Å [17]. From this perspective, it was suggested that compression of $ThCr_2Si_2$ crystals along the c-axis may result in interesting properties.

The compression of $ThCr_2Si_2$ crystals has also been investigated as an avenue to increase superconducting critical temperature. Hydrostatic compression tests of $CaFe_2As_2$ were successful in increasing the superconducting critical temperature [39]. Further experimental and computa-

tional investigations of the compression of $CaFe_2As_2$ revealed a pseudo-elastic response caused by a magnetic phase change [16, 18]. Computational investigations of $CaFe_2As_2$ compressed uniaxially along the crystallographic c-axis showed that the phase transition was achieved at lower stresses than under hydrostatic compression [30].

Efforts to increase the superconducting critical temperature of $LaRu_2P_2$ by applying hydrostatic pressure were successful in increasing T_c by 40% [13]. At or above applied hydrostatic pressures of 2.1 GPa, T_c dropped below 1.5 K. Foroozani et al. postulate that at this high hydrostatic pressure, the P−P distance is shortened and a covalent bond forms between the phosphorus atoms, which is responsible for the disappearance of superconductivity. A later study of the hydrostatic compression of $LaRu_2P_2$ characterized a tetragonal-collapsed-tetragonal phase transition [19]. Similar computational studies have also shown this crystal collapse [12]. Such a response was predicted, in theory, by Zheng and Hoffmann [17]. Their groundbreaking work highlighted the potential for phase transitions due to the vertical distance between phosphorus atoms. Specifically, if the distance between phosphorus atoms (depicted in Figure 1) were to be reduced from 3.0 Å (in uncompressed $LaRu_2P_2$) to 2.8 Å, covalent bonding may become present, perhaps inducing a collapsed phase. Furthermore, it is the bonding or antibonding properties of the P–P interaction are responsible for the variability in their distance.

There have been a number of studies, both experimental and theoretical, that have attempted to both characterize and explain the observed phase transitions in $CaFe_2As_2$. Kreyssig et al. [40] conducted hydrostatic pressure experiments and reported that the orthorhombic to collapsed tetragonal phase transition at 50 K occurs at hydrostatic pressures of 0.3 GPa. Furthermore, they noted that at a fixed hydrostatic pressure of 0.63 GPa, there is a transition from the collapsed tetragonal to the tetragonal phase at 170 K. A study by Canfield et al. [16] explored these transitions further, and built the temperature-pressure phase diagram of $CaFe_2As_2$ (Figure 3a). They too, observed a structural and magnetic phase transition at 170 K. In that study, it was also found that the transition temperature from antiferromagnetic to paramagnetic (the Néel temperature) decreases with increasing pressure. Furthermore, above pressures of about 350 MPa, the antiferromagnetic

phase ceases to exist at all. Above this pressure, the transition temperature between the tetragonal phase, and the collapsed tetragonal phase increases with temperature. In other words, at higher temperatures, higher pressures are required to collapse the crystal.

Early density functional theory (DFT) simulations by Zhang et al. focused on the simulating the phase transition using constant pressure simulations and concluded the critical pressure was 5.3 GPa [11] at 0 K, dramatically higher than experiments. Colonna et al. [41] revisited the phase transition using a volume controlled simulation instead, and found the transition to be much closer to experiments, around 0.6 GPa. Widom et al. [42] conducted a similar investigation but argued that the phase transition was a first-order enthalpic transition, rather than being associated with an instability, with a reported phase transition pressure of 0.36 GPa. In addition, Tomic et al. [20] conducted uniaxial stress-controlled DFT simulations and demonstrated that the uniaxial stress required to drive the transformation was significantly less than the required hydrostatic stress, indicating that these compounds should be more susceptible to uniaxial loading. The theoretical work has demonstrated that there can be multiple interpretations of the cause of the phase transition, either an instability driven phase transition or an enthalpic one, and that the nature of the applied load will impact the response of these compounds.

In contrast to $CaFe_2As_2$, $LaRu_2P_2$ is non-magnetic and thus is unlikely to have a phase diagram as complex as $CaFe_2As_2$. Nevertheless, hydrostatic compression experiments have demonstrated nonlinearities in its mechanical response under pressure [13, 19] which has been attributed to a tetragonal to collapsed-tetragonal transition [19]. DFT simulations have demonstrated that, in contrast to $CaFe_2As_2$, that there is no abrupt phase transition [12] and that the nature of the non-linear pressure-volume curves may have very different origins in $LaRu_2P_2$ than in $CaFe_2As_2$.

The most recent experimental work by Sypek et al. [18, 43] has investigated $CaFe_2As_2$ under uniaxial loading and demonstrated a clear pseudo-elastic response of the material. Single crystals of $CaFe_2As_2$ were grown in tin flux and a micropillar was milled with a gallium focused ion beam (FIB) such that the axis of the pillar was aligned with the crystallographic c-axis. Another micropillar was milled so that its axis was aligned with the crystallographic [031] direction. A

flat-head nanoindentor was then used to compress the micropillars uniaxially. These experiments also demonstrated that the phase transition can be induced by uniaxial loading along the c-axis and that it cannot be achieved by off-axis uniaxial compression. In that study, $CaFe_2As_2$ was observed to have a recoverable c-axis strain as high as 11.3% [43]. Reproduced compression data of these two compounds is shown in Figure 5.

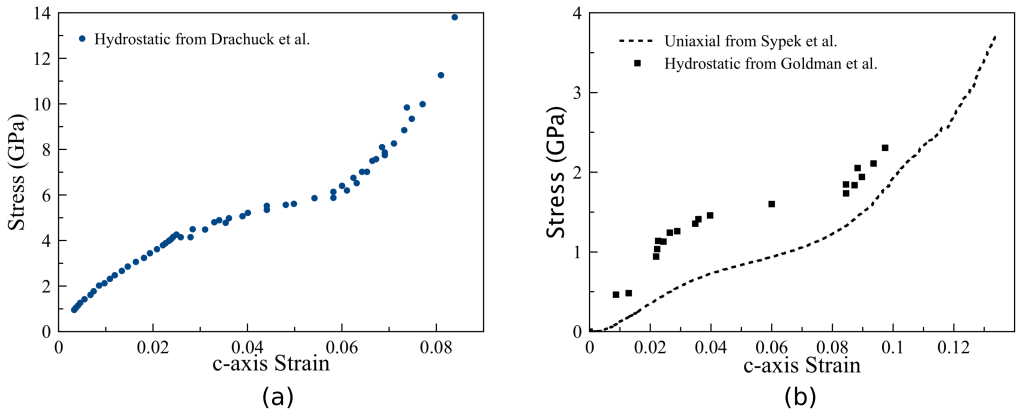

Figure 5: Experimental compression data available in the literature of $LaRu_2P_2$ (a) and $CaFe_2As_2$ (b). The hydrostatic $LaRu_2P_2$ data is reproduced from [19]. The hydrostatic $CaFe_2As_2$ data is reproduced from [44] and the uniaxial $CaFe_2As_2$ data is reproduced from [43].

In contrast to SMAs, the phase change, or crystal collapse, which facilitates the pseudo-elastic response of $ThCr_2Si_2$ is fully dimensionally stable. There are no degeneracies in the response, and thus there is far less fatigue damage over the course of shape-memory cycles. While the stress-strain response is hysteretic for other reasons, the stress-strain curve does not “walk" like those of SMAs [43] (Figure 6).

2.5 Doping and Defects in $ThCr_2Si_2$-type Crystals

The superconductive properties of $ThCr_2Si_2$-type crystals have been shown to be particularly sensitive to the presence of point defects. The introduction of substitutional defects via doping has been utilized in efforts to increase their superconducting critical temperatures. Introducing electronic holes in the iron arsenides with this structure ($CaFe_2As_2$, $SrFe_2As_2$, $BaFe_2As_2$), through

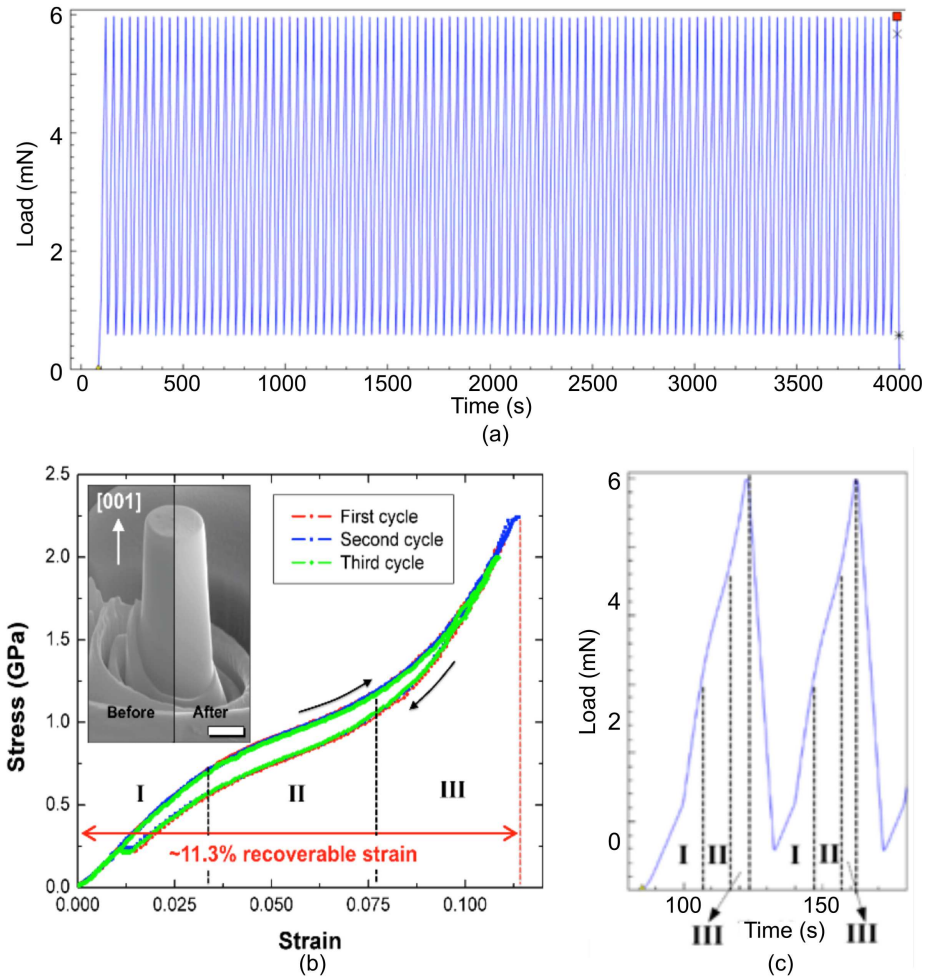

Figure 6: The cyclic uniaxial compression (a) along the c-axis of a $CaFe_2As_2$ micropillar shows hysteresis (b), but no degradation of the response over time. (c) The profile of each cyclic loading. Reproduced from [43].

doping with lower valency metals, has been shown to increase T_c. For example, doping $CaFe_2As_2$ with sodium in place of calcium has been shown to increase the superconductive critical temperature up to 20K [45]. Likewise, while neither $BaFe_2As_2$ nor KFe_2As_2 are superconductors at any temperature, doping 40% of barium sites with potassium induces superconductivity with a T_c up to 38 K [1]. Additionally, replacing the iron with cobalt has a similar effect on the critical temperature of iron arsenides [46–48]. The optimal cobalt concentration in $BaFe_2As_2$ was found to be 7.4% [49]. Another study highlighted that the superconductive properties of doped $CaFe_2As_2$ are particularly sensitive to dopant concentration. Doping $CaFe_2As_2$ with both lanthanum (in place of

calcium) and phosphorus (in place of arsenic) yielded a dramatic T_c increase [50], up to 45 K. Superconductivity was found to exist in a range of lanthanum concentrations between 12% and 18% and a phosphorus concentration of 6%. However, no superconductivity was found at a phosphorus concentration of 3%. These examples demonstrate the high sensitivity of the electronic properties to changes in the concentration of substitutional defects.

The effects of substitutional defects on electronic properties have been well documented. Similarly, it would be expected that vacancies and interstitials would also have an effect on the electronic properties of $ThCr_2Si_2$ crystals. Vacancies and interstitials in 1:2:2 intermetallics have been investigated experimentally for their effects on superconductivity. These defects were induced in $BaFe_2As_2$ doped with cobalt via proton irradiation by Nakajima et al. [51]. They found that the superconducting critical temperature decreased due to the introduction of these defects, since the defects act as nonmagnetic scattering points. However, the critical current density was enhanced in the regions of irradiation [52]. Similar investigations also revealed that Frenkel pairs in cobalt-doped $BaFe_2As_2$ affect the electronic response to an applied magnetic field [46]. Point defects of all kinds: substitutions, vacancies and interstitials, can alter the T_c in 1:2:2 compounds, demonstrating the sensitivity of these compounds to the presence of point defects.

2.6 Electronic Structure

Density functional theory (DFT) is a simulation technique part of a broader class of simulation methods known as *ab initio* (latin for “from the beginning") methods. In this work, DFT is used to calculate the electronic structure of a simulation box containing a specified number of ionic cores and electrons. This overview of the fundamentals of DFT is by no means exhaustive. Further reading on electronic structure calculation can be found in any of several textbooks [53–55]. All of the calculations in this work utilize a commercial DFT code suite: the Vienna *Ab initio* Simulation Package, or VASP [56, 57]. An outline of the methods utilized is presented here.

2.6.1 Schrödinger's Equation

The time-dependent Schrödinger's Equation for a single, non-relativistic particle:

$$i\hbar\frac{\partial}{\partial t}\psi(r,t) = \hat{\mathcal{H}}\{\psi(r,t)\} \tag{2.1}$$

We can write the momentum operator of a particle as $p = i\hbar\nabla$. Recall that the Hamiltonian operator ($\hat{\mathcal{H}}$) is the kinetic energy + the potential energy such that:

$$\hat{\mathcal{H}} = \hat{T} + \hat{V} = \frac{p^2}{2m} + \hat{V}(r,t) = \frac{-\hbar^2}{2m}\nabla^2 + \hat{V}(r,t) \tag{2.2}$$

From there we can write Schrödinger's Equation as:

$$i\hbar\frac{\partial\psi}{\partial t} = -\frac{\hbar^2}{2m}\nabla^2\psi + \hat{V}\psi \tag{2.3}$$

Time-Independent Schrödinger's Equation

If the wave function comes from a stationary state, e.g. atomic orbitals, then the Hamiltonian is not dependent on time. In this case, $\psi(r,t) = A(t)\psi(r)$ and $E\psi = \hat{\mathcal{H}}\psi$. The wave function is still a function of time, but only in its amplitude. So for a single, non-relativistic particle:

$$E\psi = (\hat{T} + \hat{V})\psi = \left[\frac{-\hbar^2}{2m}\nabla^2 + \hat{V}(r)\right]\psi(r) \tag{2.4}$$

2.6.2 From Quantum Mechanics to Density Functional Theory

For many-body electronic structure calculations, the nuclei of the molecules or clusters are treated as fixed. This is known as the Born-Oppenheimer Approximation. This generates a static external (from the perspective of the electrons) potential V through which the electrons are moving. The stationary electronic state is then defined as a wavefunction ψ that satisfies the many-electron, time-dependent Schrödinger equation.

$$\hat{\mathcal{H}}\psi = \left[\hat{T} + \hat{V} + \hat{U}\right]\psi = \sum_{i}^{N}\left[\frac{-\hbar^2}{2m}\nabla_i^2 + \sum_{i}^{N} V(r_i) + \sum_{i<j}^{N} U(r_i, r_j)\right]\psi \tag{2.5}$$

Here, $\hat{T}$ is the kinetic energy, $\hat{V}$ is the potential energy from the external field of positively charged nuclei, and $\hat{U}$ is the electron–electron interaction energy. The $\hat{U}$ term is not separable into single-particle equations since the interaction term is complicated.

There are many possible ways to solve this equation using Slater determinants. The simplest version is the Hartree-Fock method, which is also known as the self-consistent field (SCF) method.

Formulation of the Fock Matrix

The Fock operator for the ith electron is given by:

$$\hat{F}(i) = \frac{1}{2}\nabla_i^2 - \sum_{\alpha}\frac{z_\alpha}{r_{i\alpha}} + \sum_{j=1}^{N/2}(2J_j(i) - K_j(i)) \tag{2.6}$$

where the first two terms are the non-interaction terms of the Hamiltonian for the given electron: kinetic energy and static potential energy, respectively. Here, z_α is the charge of the αth nucleus and $r_{i\alpha}$ is the distance between the electron and that nucleus. The term $\hat{J}_j\{i\}$ is the Coulomb operator, which defines the repulsion of electron i by electron j as:

$$\hat{J}_j\{\psi_i\} = \psi_i \int |\psi_j|^2 \frac{1}{|r_{ij}|} dr_j \tag{2.7}$$

The electron exchange energy $\hat{K}_j\{i\}$ is represented by:

$$\hat{K}_j\{\psi_i\} = \psi_j \int \frac{\psi_j^* \psi_i}{|r_{ij}|} dr_j \tag{2.8}$$

There is no classical analog to this phenomenon. This represents the asymmetry of the wavefunctions. It plays a “what if" scenario, calculating the energy from replacing the two particles. This also addresses the antisymmetry of the Slater determinant.

The Fock operator is then used on relevant wavefunctions producing and eigenvalue-like expression:

$$\hat{F}\psi_i = \varepsilon_i \psi_i \tag{2.9}$$

Eigenfunctions which satisfy this equation are the basis functions for the electron orbitals. The Hartree-Fock method iteratively solves this formulation through the following steps:

1. Input coordinates and charges of atomic nuclei, as well as number of electrons in the system
2. Make an initial guess for the electronic orbital basis functions
3. Construct the Fock Matrix
4. Diagonalize the Fock Matrix to solve for the new basis functions
5. Check for convergence of the basis functions. If not converged, repeat from Step 3

This method is computationally expensive, and has numerical stability issues.

2.6.3 Density Functional Theory

Finding a solution to the many-body Schrödinger's Eq. with the electron-electron interaction is a very complicated problem. It would be more convenient if we could turn this into a series of single-body problems. Among other computational difficulties, it is also impossible to experimentally probe the individual wavefunctions of a system of electrons. In order to make this approximation, we must deal with the electron density. The electronic density of a normalized N-electron wavefunction is:

$$\rho(\bar{x}) = N \sum_s \int \cdots \int |\psi(\bar{x}, \bar{x}_2, \cdots, \bar{x}_N, s)|^2 d\bar{x}_2 \cdots d\bar{x}_N \tag{2.10}$$

This represents the electron density at point $\bar{x}$ based on the wavefunctions of all electrons and both spin up and spin down possibilities (s). There are some interesting, and perhaps obvious consequences to using the electron density. First, it is experimentally observable, which makes

it useful for comparing calculations to experimental data. Secondly, as we move away from the center of interest, electron density vanishes, $\rho(r \to \infty) = 0$. Also, integrating the electron density over all of space gives the total number of electrons, $\int \rho(\bar{r}) d^3r = N$.

Thomas-Fermi Model

Based on the uniform electron gas (also called the homogeneous electron gas, or *jellium*), the kinetic energy can be written as:

$$T = \frac{3h}{10m_e}\left(\frac{3}{8\pi}\right)^{2/3} \int n(\bar{r})^{5/3} d^3r \tag{2.11}$$

Here, $\bar{r}$ the spatial position vector, and n is the electron density. Additionally, the potential energy has two parts. An attraction to positively charged nuclei:

$$V(r) = \int -n(\bar{r}) \frac{Z(e^-)^2}{r} d^3r \tag{2.12}$$

and repulsion between electrons:

$$U = \frac{1}{2}(e^-)^2 \int \frac{n(r)n(r')}{|r - r'|} d^3r d^3r' \tag{2.13}$$

By this model, the entire system can be represented in terms of only the electron density. Minimizing the energy given by these expressions theoretically leads to a solution of the appropriate electron density. Unfortunately, this is a poor approximation of real systems, especially for their kinetic energy. Additionally there is no term which considers the electron exchange (Pauli exclusion principle). However, we do know how to get the kinetic energy from ψ. If a relation between ψ and $n(\bar{r})$ were known, then a more accurate result could be found.

Hohenberg-Kohn Theorem

Using the electron density as a substitute for all of the individual wave functions was mostly hopeful conjecture following the Thomas-Fermi model. The Hohenberg-Kohn theorem moved

this substitution from conjecture to reality, providing a proof that the electron density *uniquely* describes the many-electron system, and that also, the energy of the system is a functional of the electron density: $E = E[n]$. Formally, the theorem asserts 3 points:

1. In the ground state, the electron density uniquely determines the external potential of the nuclei, $V_n = f(n)$.

2. In any quantum state, the external potential uniquely determines the many-electron wavefunction $\psi = f(V_n)$.

3. In any quantum state, the total energy E is a functional of the many-body wavefunction $E = f(\psi)$.

The second and third points are straightforward; however, the first is not.

$$\hat{E} = \int n(r)V_n(r)dr + \langle\psi|\hat{T} + \hat{U}|\psi\rangle \tag{2.14}$$

assuming that ψ is the ground-state wavefunction for potential V_n with energy E and density n. We also assume another potential V_n' has the same density n but with a different wavefunction ψ' and energy E'. Only $\hat{T}$ and $\hat{U}$ are dependent on ψ. Since ψ is not the ground state of $\hat{\mathcal{H}}'$, then we know that the following must be true:

$$\langle\psi|\hat{\mathcal{H}}'|\psi\rangle > E' \rightarrow \langle\psi|\hat{T} + \hat{U}|\psi\rangle + \int n(r)V_n'(r)dr > E' \tag{2.15}$$

and thus:

$$E - E' > \int \left[Vn(r) - Vn'(r)\right] n(r)dr \tag{2.16}$$

Inversely, we get:

$$\langle\psi'|\hat{\mathcal{H}}|\psi'\rangle > E', \quad E' - E > \int \left[V_n(r) - V_n'(r)\right] n(r)dr \tag{2.17}$$

If we add these two inequalities together, we arrive at $0 > 0$, which is not possible. So we can conclude that the two “ground states" we hypothesized are, in fact, the same ground state. Furthermore, we can conclude that the electron density of the ground state does, indeed, uniquely define the system.

Kohn-Sham Equations

Given the energy operator of a system to be:

$$\hat{E} = \int n(r)V_n(r)dr + \langle\psi(n)|\hat{T} + \hat{U}|\psi(n)\rangle \tag{2.18}$$

which can be rewritten as:

$$E(r) = \int n(r)V_n(r) - \sum_i \left[\int \frac{\nabla^2}{2}\chi_i(r)d^3r + \frac{1}{2}\iint \frac{n(r) - n(r')}{|r - r'|}d^3rd^3r' + E_{\text{XC}}\right] \tag{2.19}$$

Here, E_{XC} is the still unknown value that represents the electron exchange discussed before, as well as the electron correlation term. This term states that if an electron is at point $\bar{r}$, there is a reduced likelihood that another electron will be in the vicinity. For a long time, there was much debate over how the exchange-correlation term should be calculated. Now one of the most common approaches, the Local Density Approximation (LDA) calculates the exchange-correlation term as a function of the electron density. This approach was originally proposed by Kohn and Sham along with their equations, but was largely overlooked for decades. The exchange-correlation energy of a system is approximated to be a sum of the exchange energy E_{X} and the correlation energy E_{C} as $E_{\text{XC}} \approx E_{\text{X}} + E_{\text{C}}$.

E_{X} uses the model of a free electron gas, and yields:

$$E_{\text{X}} = -\frac{3}{4}\left(\frac{3}{\pi}\right)^{1/3} n^{4/3}V \tag{2.20}$$

E_{C} however, is only known for upper and lower limits which correspond to infinitely weak and strong correlations, respectively.

$$E_{\mathrm{C}} = \begin{cases} A\ln(r_s) + Br_s(C\ln(r_s) + D) & \text{Upper Limit} \\ \frac{1}{2}\left(\frac{g_0}{r_s} + \frac{g_1}{r_s^{3/2}} \cdots\right) & \text{Lower Limit} \end{cases} \tag{2.21}$$

where r_s is the representative radius calculated by $\frac{4}{3}\pi r_s = \frac{1}{n}$.

This formulation of the Hamiltonian converges on a solution to the eigenvalue problem:

$$\hat{\mathcal{H}}\chi_i = \varepsilon_i\chi_i \tag{2.22}$$

2.6.4 Nuts and Bolts of DFT Calculations

DFT attempts to find solutions which satisfy the time-independent Schrödinger's equation:

$$\hat{H}\psi = E\psi \tag{2.23}$$

In plain words, this states that if the system is stationary, the Hamiltonian operation ($\hat{H}$) on the many-body electron wave function (ψ) is proportional to the wave function itself. Furthermore, the proportionality is, in fact, the energy of the state (E) [58]. Here the Hamiltonian operator can be thought of as the kinetic energy of each electron wave function ($\hat{T}$), and the potential energy of each electron, which itself is comprised of the potential energy in reference to atomic nuclei ($\hat{V}$), and the potential energy between electrons ($\hat{U}$). Thus, the time-independent Schrödinger's equation can be expressed as:

$$\hat{H}\psi = \left[\hat{T} + \left(\hat{V} + \hat{U}\right)\right] = \left[\sum_i^N \frac{-\hbar}{2m}\nabla_i^2 + \sum_i^N V(\mathbf{r}_i) + \sum_i^N \sum_{i<j} U(\mathbf{r}_i, \mathbf{r}_j)\right]\psi = E\psi \tag{2.24}$$

Since it is impossible to distinguish which electron is which, a more useful description is the point-wise electron density n, which can be expressed as:

$$n(\mathbf{r}) = 2\sum_i \psi_i^*(\mathbf{r})\,\psi_i(\mathbf{r}) \tag{2.25}$$

Hohenberg and Kohn stated that in the ground state, the energy E can be expressed as a functional of the electron density: $E = E\left[n\left(\mathbf{r}\right)\right]$. The energy functional can be written as a functional of the individual wave functions, and divided into parts that we know, and parts that we don't know:

$$E\left[\{\psi_i\}\right] = E_{\text{known}}\left[\{\psi_i\}\right] + E_{\text{XC}}\left[\{\psi_i\}\right] \tag{2.26}$$

The contributions to the electron energy that we know include: the kinetic energy, the interactions between the electrons and the nuclei, the interactions between electrons, and the interactions between nuclei. This can be written as:

$$E_{\text{known}}\left[\{\psi_i\}\right] = -\frac{\hbar^2}{m}\sum_i \int \psi_i^* \nabla^2 \psi_i d^3r + \int V\left(\mathbf{r}\right) n\left(\mathbf{r}\right) d^3r + \frac{e^2}{2}\int\int \frac{n\left(\mathbf{r}\right) n\left(\mathbf{r}'\right)}{|\mathbf{r}-\mathbf{r}'|} d^3r d^3r' + E_{\text{ion}} \tag{2.27}$$

The unknown term, $E_{\text{XC}}\left[\{\psi_i\}\right]$, is called the exchange-correlation (XC) functional, which incorporates quantum mechanical effects such as correcting the non-physical self-interaction and Pauli exclusion effects. Kohn and Sham further made the problem more manageable by showing that the electron density can be solved through a set of simultaneous equations, one for each electron. These are known as the Kohn-Sham equations and they resemble the time-independent Schrödinger's equation:

$$\left[-\frac{\hbar^2}{2m}\nabla^2 + V\left(\mathbf{r}\right) + V_H\left(\mathbf{r}\right) + V_{\text{XC}}\left(\mathbf{r}\right)\right]\psi_i\left(\mathbf{r}\right) = \varepsilon_i \psi_i\left(\mathbf{r}\right) \tag{2.28}$$

Where the exchange-correlation term is some functional derivative of the exchange-correlation energy with respect to electron density, as such:

$$V_{\text{XC}}\left(\mathbf{r}\right) = \frac{\delta E_{\text{XC}}\left(\mathbf{r}\right)}{\delta n\left(\mathbf{r}\right)} \tag{2.29}$$

2.6.5 Exchange-Correlation Functionals

The interactions between electrons are by far the most computationally expensive part of DFT calculations. There have been many proposed ways of calculating this term, however in these studies, we mainly employ two XC functionals: the local density approximation and the generalized gradient approximation.

Local Density Approximation

The local density approximation (LDA) is one of the simplest methods of calculating the exchange-correlation term. It is also one of the first methods to be effective in calculating XC functional. The XC term is calculated at each point as a functional of the electron density at that point [59]. Since the exchange correlation energy for a homogeneous electron gas ($\epsilon_{\text{XC}}^{\text{HEG}}$) is known exactly, the XC term can be *approximated* by on the XC energy of a homogeneous electron gas evaluated at the *local density*.

$$E_{\text{XC}}^{\text{LDA}}\left[n\left(\mathbf{r}\right)\right] = \int n\left(\mathbf{r}\right)\epsilon_{\text{XC}}^{\text{HEG}}\left(n\left(\mathbf{r}\right)\right)d\mathbf{r} \tag{2.30}$$

Simulations utilizing the LDA XC functional are known to overbind the unit cell, predicting lattice constants somewhat smaller than experimentally observed values [60].

Generalized Gradient Approximation

Efforts to improve upon the LDA method led to a class of higher-order XC functionals known as generalized gradient approximations (GGA). The GGA class of methods adds one higher order term to the XC functional. In these methods, the pointwise interaction energy is a function of the local electron density, as well as the gradient of the electron density at that point.

$$V_{\text{XC}}^{\text{GGA}}\left(\mathbf{r}\right) = V_{\text{XC}}\left[n\left(\mathbf{r}\right), \nabla n\left(\mathbf{r}\right)\right] \tag{2.31}$$

One of the most widely-used GGA methods was developed by Perdew, Burke, and Erzerhof and thus bears their names [61]. The PBE (for short) exchange-correlation functional can often offer

better predictions than LDA. The PBE XC is expected to underbind unit cells, providing lattice constants which are somewhat larger than those experimentally measured [62].

Higher-Order Functionals

Continuing this trend of expansion results in higher-order XC functionals. With each building on the last to create better approximations. This advancement has been described as “Jacob’s Ladder" because with each step in improving the XC functional, we are closer to the “holy grail" of solving Schrödinger’s equations exactly [63]. While these higher-order approximations were not used in this work, they are worth mentioning. The next rung on the ladder is achieved by expanding the approximation to the second derivative of the local density:

$$V_{\text{XC}}^{\text{Meta-GGA}}\left(\mathbf{r}\right) = V_{\text{XC}}\left[n\left(\mathbf{r}\right), \nabla n\left(\mathbf{r}\right), \nabla^2 n\left(\mathbf{r}\right)\right] \tag{2.32}$$

This class of XC functionals is known as “Meta-GGA" and there are several different approaches to their formulations.

2.6.6 Hubbard U Correction

Density functional theory exhibits the systematic problem of electron self-interaction. Since the potential energy of an electron is calculated from the electron density at each point, the density to which that same electron contributes, these XC functionals calculate an electron’s self-repulsion, which is nonphysical. Such an interaction becomes particularly debilitating for highly localized electrons, such as those in f orbitals. This is, however, not an artifact of the Hartree-Fock method, and a combination of the two methods could be beneficial to mitigating this issue. Such a suite of methods have been developed, and numerous formulations have been implemented. One of the simplest implementations of these methods uses one weighting parameter, $(U - J)$, to correct the XC energy:

$$E_{\text{LDA}+U} = E_{\text{LDA}} + \frac{(U-J)}{2}\sum_{\sigma}\left[\left(\sum_{m_1} n^{\sigma}_{m_1,m_2}\right) - \left(\sum_{m_1,m_2} \hat{n}^{\sigma}_{m_1,m_2}\hat{n}^{\sigma}_{m_2,m_1}\right)\right] \tag{2.33}$$

This parameter is on the order of unity and must be chosen, usually by finding the value of $(U - J)$ which best approximates some known physical value.

2.6.7 Pseudopotentials

Since the simulation of individual electrons is rather costly (the computational cost scales approximately $\mathcal{O}(N_{e^-}^3)$) [64, 65], reducing the number of electrons needed in the simulation goes a long way toward increasing the speed of a DFT calculation. Furthermore, simulating waves which are confined to relatively small length scales, such as the core electrons, require increased computational efforts. For these reasons, it may be beneficial to only simulate the valence electrons involved with bonding. However, it would be incorrect to assume that the core electrons (those in the inner shells) do not have a measurable effect on the valence electrons. These core electrons shield the positive charges of the atomic nuclei to which they are attached. These effects are accounted for by defining a fixed electron density near the ionic center. These "frozen-core" fields are known as pseudopotentials. The potentials are "pseudo" since they do not represent how an electron interacts with an lone atomic nucleus, but instead how it interacts with a nucleus surrounded by a specified set of core electrons. There are a few types of pseudopotentials, but the most commonly used are ultra-soft pseudopotentials (USPP) and projector augmented-wave pseudopotentials (PAW) [66]. This study will exclusively employ PAW pseudopotentials.

2.6.8 K-Space Sampling

Since the solutions to Schrödinger's equations are the electron plane-waves in periodic supercells, it is useful to solve for these waves in reciprocal space. The reciprocal space vectors, **k**, must satisfy Bloch's theorem:

$$\phi_{\mathbf{k}}(\mathbf{r}) = \exp(i\mathbf{k}\cdot\mathbf{r})\, u_{\mathbf{k}}(\mathbf{r}) \tag{2.34}$$

Here, the function $\exp(i\mathbf{k}\cdot\mathbf{r})$ is a plane wave, which is periodic over the simulation cell. It is easier to evaluate this integral in reciprocal space, or *k*-space, than in 3-dimensional real space. Just like real space, the reciprocal lattice has associated basis vectors in reciprocal space, known

as reciprocal lattice vectors. They are defined such that:

$$\mathbf{b}_1 = 2\pi \frac{\mathbf{a}_2 \times \mathbf{a}_3}{\mathbf{a}_1 \cdot (\mathbf{a}_2 \times \mathbf{a}_3)}, \mathbf{b}_2 = 2\pi \frac{\mathbf{a}_3 \times \mathbf{a}_1}{\mathbf{a}_2 \cdot (\mathbf{a}_3 \times \mathbf{a}_1)}, \mathbf{b}_3 = 2\pi \frac{\mathbf{a}_1 \times \mathbf{a}_2}{\mathbf{a}_3 \cdot (\mathbf{a}_1 \times \mathbf{a}_2)} \tag{2.35}$$

This means that the magnitudes of the reciprocal lattice vectors, $|b_i|$, are inversely related to the magnitudes of the real-space lattice vectors by: $\frac{2\pi}{|a_i|}$.

The primitive unit cell in reciprocal space is known as the Brillouin zone, and contains a great deal of information regarding band theory. The volume of the Brillouin zone is given by:

$$V_{\text{BZ}} = \frac{(2\pi)^3}{V_{\text{cell}}} \tag{2.36}$$

Since DFT is solving for the solutions of integrals of plane-wave functions, it is easier to compute them in k-space. For speed, the k-space integration is performed with quadrature, and the domain is meshed to provide integration points. While there are many ways to choose these points, one of the most common, and the one used exclusively in this work, is the Monkhorst-Pack k-space meshing algorithm [67].

2.6.9 Forces from Electronic Structure

Solving for the electronic ground state is all well and good, but in order for these simulations to be useful, we need to be able to calculate forces on the ions, and stresses in the crystal. The forces on a particle at point $\mathbf{R}$ in a quantum-mechanical system is given by the derivative of the energy at that point:

$$\mathbf{F} = -\nabla_{\mathbf{R}} \langle E \rangle \tag{2.37}$$

In our system, $\langle E \rangle = \langle \psi | \hat{\mathcal{H}} | \psi \rangle$, and our wavefunctions are normalized. Thus we can use the Hellman-Feynman Theorem to calculate the derivative of the total energy with respect to a given parameter (λ) as [68]:

$$\frac{\partial E}{\partial \lambda} = \langle \psi | \frac{\partial \hat{\mathcal{H}}}{\partial \lambda} | \psi \rangle \tag{2.38}$$

Since in our DFT simulations, we are dealing with the Kohn-Sham Hamiltonian of the electronic density:

$$\hat{\mathcal{H}}_{\mathbf{R}} = -\frac{1}{2}\nabla^2_{\mathbf{r}} + V_{e-e}(\mathbf{r}) + V_{\text{ion}-e}(\mathbf{r},\mathbf{R}) + V_{\text{XC}}(\mathbf{r}) + V_{\text{ion–ion}}(\mathbf{R}) \tag{2.39}$$

we can see that for the force on a given ionic nucleus, there are only contributions from the inter-ionic Coulombic forces and the interaction between ions and electrons from the pseudo-potential. To calculate the stress tensor in the simulation cell, the derivative of energy is taken with respect to cell geometry parameters.

2.6.10 Structural Relaxation

The relaxation of the crystal, ionic coordinates and cell size and shape, is a fundamental tool to this work. The computation of the structural minimum is accomplished in VASP with the Conjugate Gradient (CG) method [69,70]. This method iteratively seeks to find the minimum of a system of equations described by: $f(x) = \frac{1}{2}x^{\mathrm{T}}Ax - x^{\mathrm{T}}b$. The minimum of this linear system of equations is the solution to: $Ax = b$. The initial direction towards solving is taken to be the residual of system of equations at the chosen starting point:

$$d_{(0)} = r_{(0)} = b - Ax_{(0)} \tag{2.40}$$

$$x_{(i+1)} = x_{(i)} + \alpha_{(i)}d_{(i)} \tag{2.41}$$

The magnitude of search along that vector is based on the residual:

$$\alpha_{(i)} = \frac{r^{\mathrm{T}}_{(i)}r_{(i)}}{d^{\mathrm{T}}_{(i)}Ad_{(i)}} \tag{2.42}$$

After each step, a new residual is computed, the next direction is chosen, and the process is repeated.

$$r_{(i+1)} = r_{(i)} - \alpha_{(i)}Ad_{(i)} \tag{2.43}$$

$$\beta_{(i+1)} = \frac{r_{(i+1)}^{\mathrm{T}} r_{(i+1)}}{r_{(i)}^{\mathrm{T}} r_{(i)}} \tag{2.44}$$

$$d_{(i+1)} = r_{(i+1)} + \beta_{(i+1)} d_{(i)} \tag{2.45}$$

This is repeated until some convergence criterion is met. The strength of CG minimization, over, for example, Steepest Descent, is that each successive search direction is orthogonal to all previous search directions. So the solution to a linear system of equations with an nth order basis set should only take n steps.

Of course, this would not be useful to us if it *only* solved linear systems of equations. This method can be generalized for a nonlinear system of equations, where the solution is found to be where the gradient of the function is zero:

$$\nabla_x f(x) = 2A^{\mathrm{T}}(Ax - b) = 0 \tag{2.46}$$

The initial step (Δx_0) is chosen by computing the steepest descent of the initial position (x_0):

$$\Delta x_0 = -\nabla_x f(x_0) \tag{2.47}$$

The step length (α) is chosen along that step direction which minimizes the function by:

$$\alpha_0 = \min_{\alpha} f(x_0 + \alpha \Delta x_0) \tag{2.48}$$

The position is then updated by that step length in that direction:

$$x_1 = x_0 + \alpha_0 \Delta x_0 \tag{2.49}$$

This process is then repeated. However, in subsequent iterations, the search direction (s_n) is updated to be a conjugate to previous directions as:

$$s_n = \Delta x_n + \beta +_n s_{n-1} \tag{2.50}$$

For the second iteration, $s_0 = \Delta x_0$. There are many methods of computing β, one of the most common being the Fletcher-Reeves formula [71]:

$$\beta_n^{\text{FR}} = \frac{\Delta x_n^{\text{T}} \Delta x_n}{\Delta x_{n-1}^{\text{T}} \Delta x_{n-1}} \tag{2.51}$$

The line search now finds the step size which minimizes the function in the s_n direction:

$$\alpha_n = \min_{\alpha} f(x_n + \alpha s_n) \tag{2.52}$$

2.6.11 Periodicity

Since DFT can only simulate a small number of atoms, it is advantageous to simulate periodic domains. A periodic domain is one that repeats in each direction forever. The conditions of the one cell of the simulation is also the conditions of every other cell repetition. This simulates an infinite medium, as shown in Figure 7.

2.6.12 Hydrostatic and Uniaxial Compression

The majority of this study, as a thesis in mechanical engineering, focuses on the mechanical properties of materials, i.e. how they respond to applied stress and strain. There are two loading scenarios in particular which are investigated here: hydrostatic compression and uniaxial compression. Hydrostatic compression, depicted in Figure 8(a), is compression in all directions with the same intensity. This can often be achieved by submerging the sample in a compressed fluid, in which case the pressure of the fluid acts on the sample in all directions, indiscriminately. Uniaxial compression (Figure 8(b)), as the name implies, is compression on only one (uni) axis (axial). The uniaxial compression which is most interesting to us in these crystals is along the c-axis. The stress states of hydrostatic and uniaxial compression are:

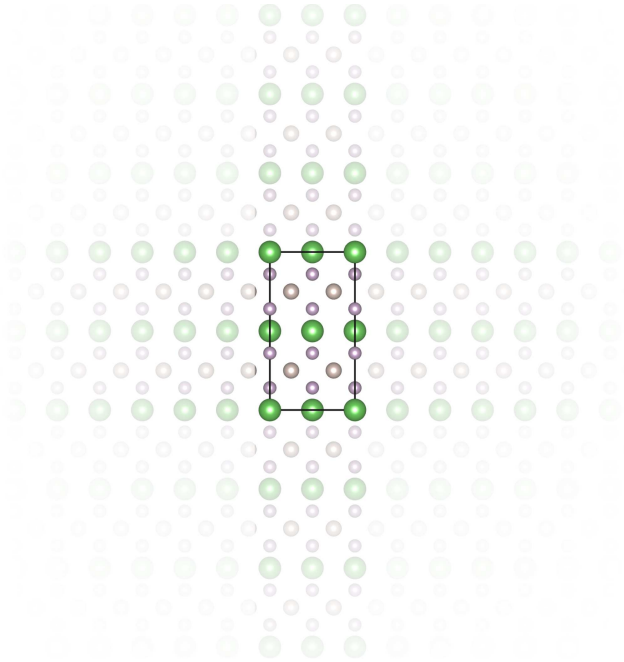

Figure 7: Periodic simulations repeat a representative cell in every direction, thus representing an infinite medium. The conditions of the simulation cell are repeated for all other cells in the infinite medium.

$$\sigma_{\text{hyd}} = \begin{bmatrix} P & 0 & 0 \\ 0 & P & 0 \\ 0 & 0 & P \end{bmatrix}, \sigma_{\text{uni}} = \begin{bmatrix} 0 & 0 & 0 \\ 0 & 0 & 0 \\ 0 & 0 & P \end{bmatrix} \tag{2.53}$$

VASP does not natively support the simulation of an arbitrary stress state, such as uniaxial compression. In order to achieve this stress state, an iterative loop of DFT simulations must be performed. Simulations in VASP have a limited set of cell-geometry control states during ionic relaxation:

1. Cell lattice parameters and volume are relaxed.

2. Cell lattice parameters are relaxed, cell volume is held fixed.

3. All cell lattice parameters are held fixed.

The first condition simulates full relaxation with no applied stress. The second condition can be used to impose a strain-controlled hydrostatic stress state. However to achieve a non-hydrostatic,

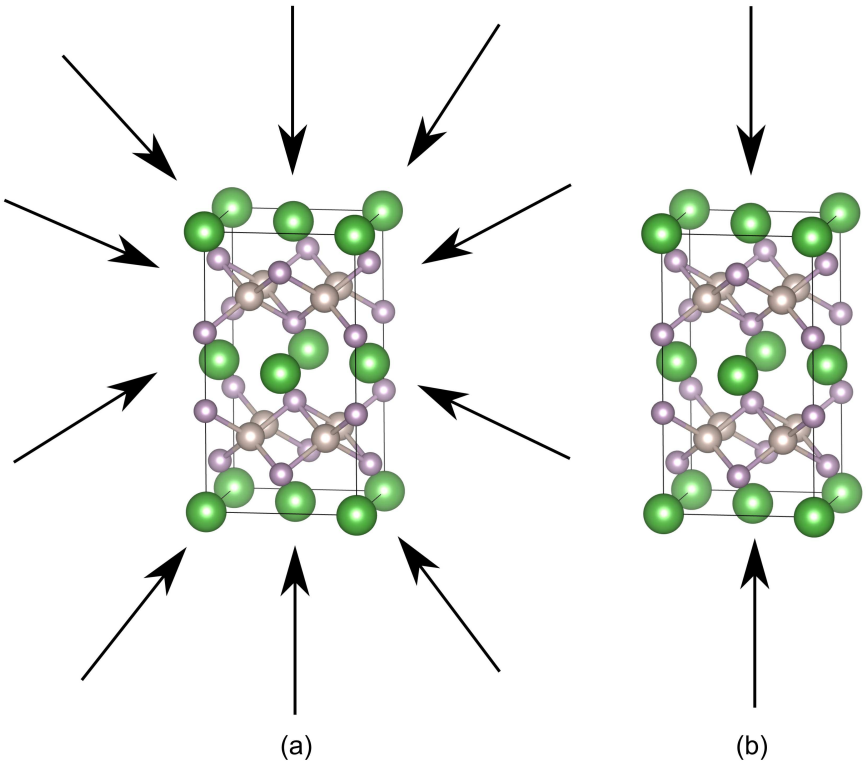

Figure 8: (a) Hydrostatic compression is an equal compression of a material in all directions. (b) Uniaxial compression is compression along only one axis. Both loading scenarios were investigated in this study, and the uniaxial compression was always along the crystal's c-axis.

nonzero stress state, the third condition must be utilized along with an iterative wrapper. The procedure, depicted in flowchart form in Figure 9, requires prior knowledge of the elastic constants for optimal convergence. A uniaxial strain is first specified, and the simulation box is deformed in accordance with Hooke's law. A DFT ionic relation is then performed while the box dimensions are kept fixed. Following the relaxation, the stresses in the lateral axes are reported, and if they are not zero (within a specified tolerance), the simulation box lengths in those directions are adjusted in accordance with the elastic constants to bring the stresses closer to zero. The simulation cell with updated dimensions is run again and this loop is repeated until the lateral stresses are eliminated.

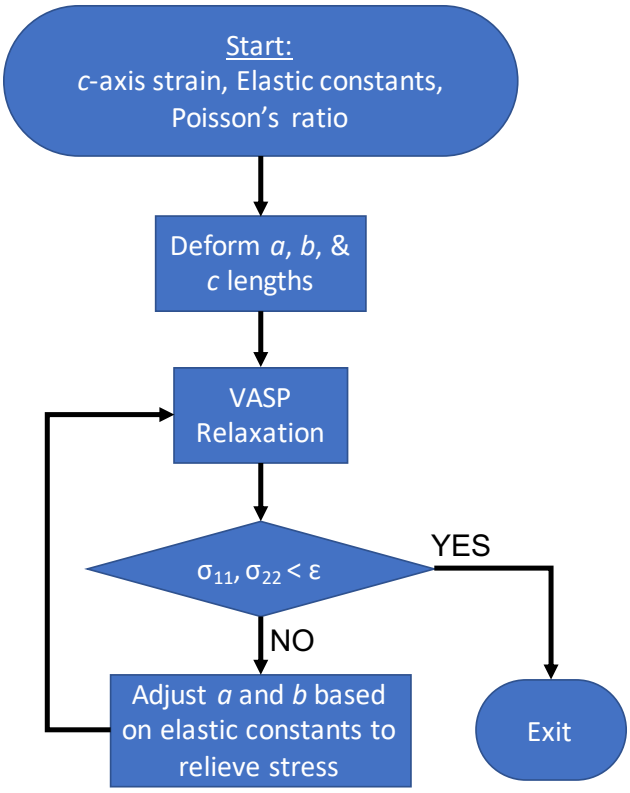

Figure 9: Flowchart of the wrapper algorithm required to simulate uniaxial compression in VASP. The ionic relaxation in VASP is performed by keeping the simulation cell box lengths constant, and relaxing the ionic positions inside

2.7 Evolutionary Crystal Structure Algorithms

The bulk of this study involves the evaluation of stoichiometries of ternary intermetallic compounds which have not previously been reported. These concentration ratios may not be in literature because a set of ternary compounds may not be well studied, or the stoichiometry is due to high concentrations of defects. However, for reference, it is important to find the lowest energy structures of these stoichiometries.

With this goal in mind, the USPEX evolutionary algorithm is utilized [72–74]. USPEX searches for the “fittest" structure through a generational competitive selection process as follows: An initial set of structures is generated, through a combination of user-provided “seed" structures, or randomly generated structures. These are all relaxed with DFT, and their energies are calculated. Then, in user-defined ratios, a certain top percentage of structures are carried through to the next

generation, while the lineage of the others is ended. The structures which are carried through are mutated slightly (randomly) to see if a slightly lower state can be generated. The next generation is then filled out with new random structures. This continues for a pre-defined number of generations, or if a particular structure is the lowest energy structure for many generations.

This algorithm can be used for a single concentration or chemistry may be a changeable variable. In this work, USPEX is used in a targeted fashion; only one stoichiometry is investigated at a time.

2.8 Special Quasirandom Structures

Special quasirandom structures (SQSs) are useful in representing substitutionally random structures by a relatively small, repeatable structure [75]. For an alloy of metal A and metal B, a single representative structure with an appropriate arrangement of atoms A and B can be analyzed instead of sampling all possible spatial combinations of A and B in the unit cell for a given composition. This concept can also be applied to “alloys" of atoms and vacancies. Representative SQSs can be constructed with appropriately chosen vacant sites to simulate a random distribution of vacancies at a given concentration. The SQSs utilized in this study were generated by the alloy theoretic advanced toolkit (ATAT) [76–89].

In this formulation, SQSs are generated by implementing a cluster expansion of the primitive unit cell of the parent structure. In a stochastic process, the results of the cluster expansion are evaluated by an objective function. The SQS which best minimizes this function is the most likely to give have equivalent properties to a truly random structure. The complete methodology to how ATAT computes SQSs can be found in [80].

2.9 Homogenization Theory

In this work, we are motivated to predict the responses of heterogeneous materials, that is, materials consisting of two or more phases, with distinct mechanical responses. The goal of any homogenization theory is to compute the effective elastic response of the composite material of

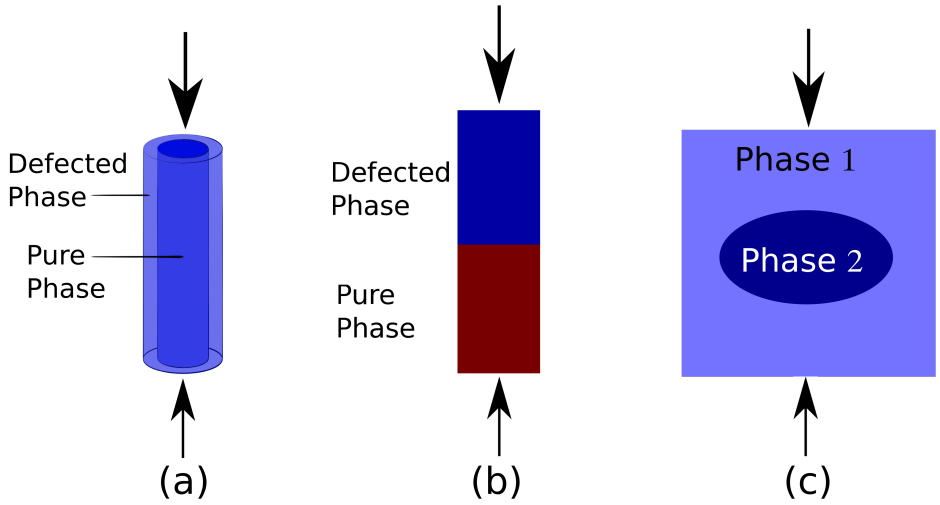

Figure 10: The three homogenization models employed in this work. (a) A simple iso-strain model, (b) a simple iso-stress model, and (c) Eschelby's ellipsoidal coherent inclusion. The inclusion model can be explored in two different configurations, since it matters which phase is chosen for the matrix and inclusion.

the form:

$$\sigma^*_{ij} = \bar{C}_{ijkl}\varepsilon^*_{kl} \tag{2.54}$$

where σ^* and ε^* are the total observed stress and strain in the composite and $\bar{C}$ is the effective elastic constant tensor. There are many methods of approaching this problem. In this work, we employ techniques based on homogenization theory of materials with constant phase-fractions. Specifically, we construct iso-strain, iso-stress, and Eshelby's inclusion models, which are depicted in Figure 10.

2.9.1 Iso-Strain and Iso-Stress

One of the simplest ways to achieve the goal of homogenization of mechanical properties is to consider them in a simple weighted average of the two phases. This is the root of the iso-stress and iso-strain composite models. These models form theoretical bounds for the possible mechanical behavior of the composite. For the iso-stress model, it is possible, though not at all necessary, to envision this model as having two concentric phases shown in Figure 10(a). Under the assumptions of an iso-strain model, the strains in each phase, however dispersed or divided, are the same:

$$\varepsilon^{(1)} = \varepsilon^{(2)} = \varepsilon \tag{2.55}$$

While the macroscopic stress is a volume average of the stresses in the two phases:

$$V\sigma = V^{(1)}\sigma^{(1)} + V^{(2)}\sigma^{(2)} \tag{2.56}$$

or:

$$\sigma = \phi^{(1)}\sigma^{(1)} + \phi^{(2)}\sigma^{(2)} \tag{2.57}$$

where $\phi^{(1)}$ and $\phi^{(2)}$ are the volume fractions of the pure and defected regions, respectively. The prediction of the overall stress-strain response, i.e. $\sigma(\varepsilon)$, requires just the individual stress-strain responses of the two phases and their volume fractions.

Alternatively, the composite can be modeled using an iso-stress model, which can be envisioned as two regions stacked on one another (Figure 10(b)). This results in the stresses in each phase being equal to the applied stress:

$$\sigma^{(1)} = \sigma^{(2)} = \sigma \tag{2.58}$$

and thus, the macroscopic strain is a volume average of the strains in the two phases.

$$V\varepsilon = V^{(1)}\varepsilon^{(1)} + V^{(2)}\varepsilon^{(2)} \tag{2.59}$$

Since the two phases are assumed to have the same cross sectional area, their volume fractions reduce to their length fractions, and the overall strain reduces to:

$$\varepsilon = \phi^{(1)}\varepsilon^{(1)} + \phi^{(2)}\varepsilon^{(2)} \tag{2.60}$$

2.9.2 Eshelby's Inclusion Composite Model

The iso-strain and iso-stress models are indeed the simplest models that can be used as they do not typically include the added effects of coherency. These homogenization models can be

improved by solving a more complicated elasticity problem that includes the interaction of the matrix and the inclusion, but must assume some geometry to do so.

In composite theory, the dilute model can be used to predict the effective elastic constants as [90, 91]:

$$\bar{C} = C^M + \phi(C^I - C^M) : \mathcal{A}^I \tag{2.61}$$

Where $\mathcal{A}^I$ is the strain concentration tensor which relates the macroscopic applied strain to the average inclusion strain, C^M is the matrix elastic constants, C^I is the inclusion elastic constants and ϕ is the volume fraction of the inclusion.

The strain localization tensor requires the use of a theory that enables one to determine the average strain field experienced by the inclusion. The most widely used, and expedient, is the Eshelby inclusion method, in which the inclusion is approximated as an ellipsoid (Figure 10(c)), which results in a constant strain inside the inclusion. In this case, the strain localization tensor is:

$$\mathcal{A}^I = \mathbb{A}^I : (\mathbb{A}^I - \mathcal{S}^{I,\infty})^{-1} \tag{2.62}$$

$$\mathbb{A}^I = (C^M - C^I)^{-1} : C^M \tag{2.63}$$

where $\mathcal{S}^I$ is the Eshelby tensor. For anisotropic materials, the simplest method to represent the Eshelby tensor is through the auxiliary tensor, $\mathcal{D}$, as:

$$\mathcal{S}^{I,\infty}_{ijkl} = -\frac{1}{2} C_{lkmn} \left(\mathcal{D}_{iklj} + \mathcal{D}_{jkli}\right) \tag{2.64}$$

The auxiliary tensor is defined as [92]:

$$\mathcal{D}_{ijkl} = -\frac{1}{4\pi} \int_0^{\pi} \int_0^{2\pi} (zz)^{-1}_{ij} z_k z_l \sin\Phi d\Theta d\Phi \tag{2.65}$$

In the case studied here, it is acceptable to assume the inclusion is a sphere since we have no other information and this makes the integration of (Eq. 2.65) easy using Lebedev integration [93–96]. Assuming the orientation of the crystals and their elastic equations, Eq. 2.65 can be integrated

to produce the auxiliary tensior, the Eshelby tensor, and eventually the localization tensor to predict the effective elastic constants.

In our problem, further complications arise since at least one of the materials is not linear elastic. In this case, we compute the effective tangent elastic constants using the aforementioned dilute approximation and the Eshelby tensor for a spherical inclusion. This was done by first computing the tangent elastic constants along the whole strain path, and splining the data to create a continuous set of elastic constants. Meanwhile, the elastic stiffness tensor of the defected phase was assumed to be constant with respect to strain (linear elastic).

As with the iso-strain models constructed for this study, the overall strain (ε^0) was specified, and the resulting stress in the composite was calculated. The model marches in overall strain, and the effective elastic tensor ($\bar{C}$) is calculated. This is done by first iteratively solving for the individual strains in each phase. Initial guesses were provided for the individual phases' strains. For the first strain step, the iso-strain condition was provided as the initial guess, while in subsequent strain steps, the previous solution was provided as an initial guess. These strains, particularly the strain in the pure phase were used to calculate the strain localization tensor ($\mathcal{A}^I$) which, in turn was used to calculate the strain in the inclusion by:

$$\varepsilon^I = \mathcal{A}^I : \varepsilon^0 \tag{2.66}$$

and the strain in the matrix was then be calculated by:

$$\varepsilon^M = \frac{1}{1-\phi}(\varepsilon^0 - \phi\varepsilon^I) \tag{2.67}$$

These individual strains were then used to calculate the strain localization in the inclusion, and thus the loop was repeated. The individual strains were considered converged when the difference in the individual strains calculated by successive iterations was less than 1×10^{-4}.

With the individual strains calculated, the effective stiffness tensor and the effective compliance tensor were calculated for a given total strain, and the uniaxial stress increment $d\sigma$ was calculated

by:

$$d\sigma = \frac{1}{\bar{S}_{3333}(\varepsilon^0)} \tag{2.68}$$

which, due to the employment of tangent modulus homogenization, can be integrated up to the stress at a given strain by:

$$\sigma(\varepsilon^0) = \int_0^{\varepsilon^0} d\sigma \tag{2.69}$$

2.10 Overview

In this thesis we attempt to answer the questions posed in Chapter 1. Through DFT modeling, knowledge of thermodynamics, continuum-scale theories, and homogenization techniques, we characterize the mechanical responses of $ThCr_2Si_2$-type crystals, as well as the impact of point defects on these responses. Point defects can include vacancies, interstitials, and substitutional defects (doping). The effects of these defects were investigated in isolation, such that there is no convolution of the effects of multiple types of defects.

In Chapter 3, we investigate the pseudo-elastic responses of pure $ThCr_2Si_2$-type crystals. We study the responses of two compounds as case studies: $CaFe_2As_2$, and $LaRu_2P_2$. $CaFe_2As_2$ exhibits a magnetic phase transition during compression, while $LaRu_2P_2$ has a smooth phase transition during compression. The hydrostatic and uniaxial responses of single unit cells of these compounds, simulated with DFT, were built up to continuum scales to predict the pseudo-elastic response of a sample. These models predicted the compression-induced phase transition in a sample of the material under load-control and displacement-control conditions. The outputs of these models were compared to experiments which showed good agreement. The chemical and bonding origins of pseudo-elasticity in $CaFe_2As_2$, $LaRu_2P_2$, and other related compounds were further explored with electronic structure calculations, revealing evidence of bonding between pnictogen atoms under compression.

Then, in Chapter 4, we analyze how point defects, specifically vacancies and interstitials can influence the mechanical response of $ThCr_2Si_2$-type crystals. We accomplish this by first simulating the properties and energetics of isolated defects, which requires the compilation of ternary

phase diagrams for each of the chemical systems for our two case studies. We then simulate defects at high concentrations, including their crystal structures and mechanical responses. We predict that high concentrations of vacancies can induce a crystal collapse which suppresses the pseudo-elastic response of the pure material. Experimental investigations of defected samples point to a segregation of these defected structures in the sample. Composite models representing this segregation of defects were constructed to explain the mechanical responses observed experimentally.

In Chapter 5, we investigate what effects doping $CaFe_2As_2$ might have on its pseudo-elastic properties. First, doping $CaFe_2As_2$ with strontium or barium (in place of calcium) was simulated. The mechanical responses of a random distribution of dopants, as well as ordered layered superstructures were simulated. In the randomly-ordered structures, the strains and stresses at which the phase transition occurs varied nearly linearly with dopant concentration. In the ordered superstructures, we saw different regions of the material respond to compression independently, sometimes resulting in multiple phase transitions. Then, doping $CaFe_2As_2$ with cobalt in place of calcium was investigated. Concentrations of cobalt above a critical point suppressed the magnetism of $CaFe_2As_2$ and induced a crystal collapse, similar to vacancies studied in Chapter 4.

Ineastic deformation in these materials was investigated in Chapter 6. Cleavage simulations were performed for $CaFe_2As_2$ and $LaRu_2P_2$ on several possible cleave planes and chemistries. It was found that the planes normal to the c-axis, in line with layered nature of the crystal, required the least energy to cleave in both $CaFe_2As_2$ and $LaRu_2P_2$. This suggests a preferred slip and fracture plane, which is congruent with previous studies of inelastic deformation in these materials. Conclusions from this study, as well as proposed future work can be found in Chapter 7.

Chapter 3

Mechanical Response of Pure $ThCr_2Si_2$-type Crystals

In order to simulate the stress-strain responses of macro-scale $ThCr_2Si_2$-type crystals, DFT simulations of these crystals under hydrostatic and uniaxial compression were run. Since DFT is very computationally expensive, simulating large numbers (greater than a few hundred) of atoms is prohibitively expensive. For this reason, the compression of single unit cells of $ThCr_2Si_2$-type crystals were simulated. The stress-strain and energetics data from these compression simulations was scaled up to the continuum scale via multi-phase composite models.

3.1 Compression Simulations of $CaFe_2As_2$

In simulating the compression of $CaFe_2As_2$, an important aspect which must be captured is the magnetic phase transition. According to the magnetic phase diagram, the ground state of $CaFe_2As_2$ is its antiferromagnetic, orthorhombic phase. While experiments at room temperature start with the paramagnetic, tetragonal phase of $CaFe_2As_2$, this cannot be effectively simulated by DFT. Due to the short box-lengths of the simulation cell, and the periodic nature of the simulations, any magnetic moments form a repeated pattern, which is by definition, NOT paramagnetism. For this reason, the initial simulated phase of $CaFe_2As_2$ is the antiferromagnetic, orthorhombic phase. This approximation (studying the AF phase instead of the paramagnetic phase) should be well within DFT accuracy since the difference in the a and b lattice constants of the orthorhombic phase is only about 1%.

3.1.1 Magnetic Ordering of $CaFe_2As_2$

It is very important that the DFT simulations accurately capture this magnetism. Simulations of $CaFe_2As_2$ utilizing the LDA XC-functional could not solve for the antiferromagnetic ordering of the Fe magnetic moments [41]. This was confirmed by our own calculations. For this reason, we turned to the PBE XC-functional for magnetic calculations.

While the antiferromagnetic ordering of $CaFe_2As_2$ has been previously observed and well documented [44], all possible magnetic orderings within a single orthorhombic unit cell (including nonmagentic and ferromagnetic) were simulated to ensure that the reported ordering was, in fact, the ground state predicted by DFT. The antiferromagnetic orderings are depicted in Figure 11. Simulations confirm that the antiferromagnetic stripe commonly reported is indeed the ground state. The nonmagnetic state solved for the shorter collapsed-tetragonal phase and an energy of -6.110 eV per atom. The magnetic moments of the ferromagnetic state dropped to zero and the nonmagnetic cT phase was found also with an energy of -6.110 eV per atom. The antiferromagnetic checkered pattern (Figure 11(a)) and the horizontal layered pattern (Figure 11(b)) did not retain their magnetic moments either, settling on the cT phase with an energy of -6.110 eV per atom. The vertical layered antiferromagnetic pattern (Figure 11(c)) kept its magnetic moments, with magnetic moment magnitude of 1.68 μ_B per iron atom. The energy of this configuration was -6.105 eV per atom. The vertical striped antiferromagnetic pattern (Figure 11(e)) also solved for the collapsed tetragonal, nonmagnetic state, with an energy of -6.110 eV per atom. The horizontal striped pattern (Figure 11(d)) kept its magnetic ordering and solved for spins of 1.83 μ_B per iron atom. The energy of this configuration was -6.115 eV per atom, which was the lowest of all configurations tested. This helped instill confidence in DFT's ability to simulate $CaFe_2As_2$ moving forward.

3.1.2 Selection of the Exchange-Correlation Functional

As shown in Section 3.1.1, we found the antiferromagnetic horizontal stripe pattern, with magnetic moments of ± 1.83 μ_{B}, to have the lowest energy, which is in line with previous investigations [44]. It is worth noting that these magnetic moments are much greater than the 0.805 μ_{B} observed experimentally [97]. It has been shown that the more accurate magnetic moments can be computed through the Hubbard U correction of the GGA-PBE XC functional (GGA+U) [98, 99]. In order to match the experimentally observed magnetic moments, an effective U_{eff} of -1.037 eV (taking the Dudarev approach [100]) was successful in predicting the experimental magnetic mo-

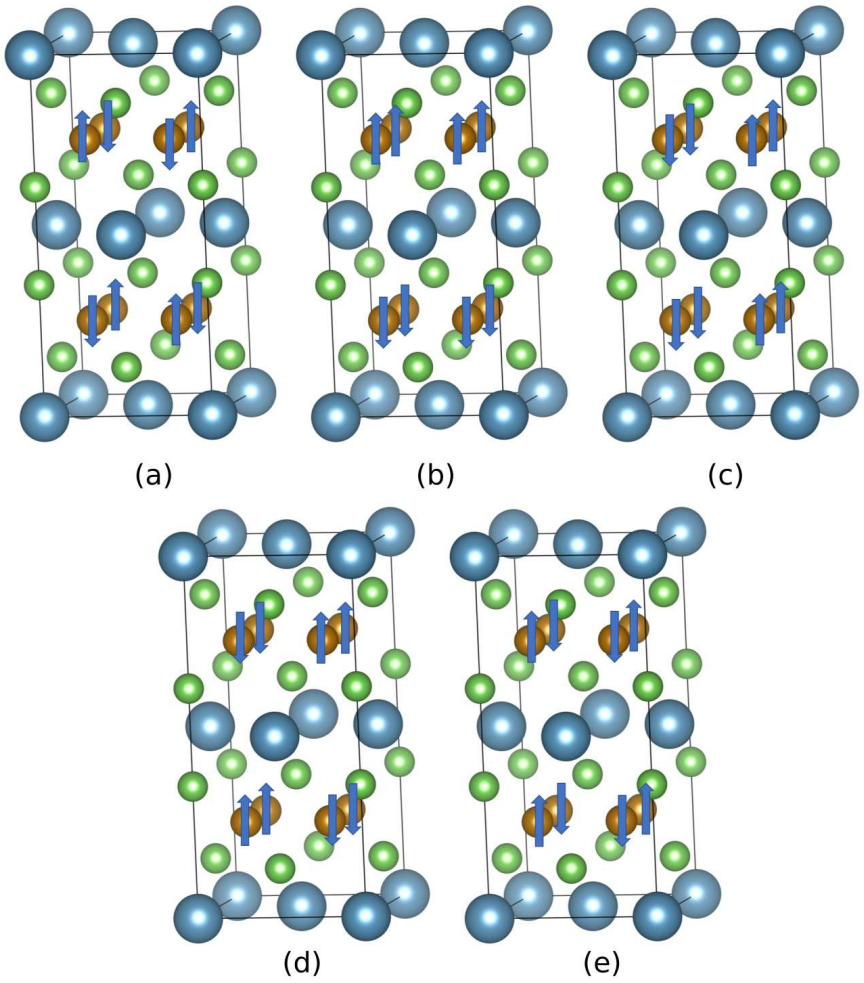

Figure 11: Antiferromagnetic (AF) orderings which were tested to determine/confirm the AF ground state of $CaFe_2As_2$. The ferromagnetic (not pictured), along with the checkered (a), horizontal layered (b), and vertical stripe (e) AF orderings, all solved for a nonmagnetic state. The vertical layering (c) solved for nonzero magnetic moments, but a higher energy than the nonmagnetic states. The horizontal stripe pattern (d) kept its magnetic moments and had a lower energy than all other states.

ments. However, this is only achieved without relaxing the crystal. When relaxing the crystal, which is crucial for this study, simulations U_{eff} less than -0.25 could not stabilize the magnetic moments. Thus, the lowest magnetic moment which could be stabilized in a relaxed crystal was $\pm 1.47\ \mu_B$. This relaxed crystal had lattice constants of: $a = 5.59$, $b = 5.49$, and $c = 11.36$, which deviated further from the reported experimental values as compared with simulations that do not include the U correction. Furthermore, structurally relaxed simulations of the antiferromagnetic and nonmagnetic phases with a $U_{eff} = -0.25$ predict the nonmagnetic collapsed-tetragonal phase

to be energetically preferred over the antiferromagnetic orthorhombic phase. We know this to be physically untrue. This demonstrates that the Hubbard U correction, as applied to the PBE XC functional, indeed can be useful in predicting the correct magnetic moments in $CaFe_2As_2$. However, its predictions of the mechanical and energetic properties, which are critical to this study, agree less with experimentally observed values. Another interesting point to make is that this negative value of $U_{eff} = U - J$ represents overscreening such that Hund's rule coupling (J) is stronger than the correction for self-interaction (U). This approach, as well as a negative U_{eff} has been previously employed to capture the correct magnetic moments of the irons in ternary iron arsenides [98].

Table 2: Lattice constants of $CaFe_2As_2$ and $LaRu_2P_2$ observed in experimental studies and predicted in this work utilizing DFT. Experimental lattice constants for $CaFe_2As_2$ are from work by Ni et al. [28] and experimental lattice constants for $LaRu_2P_2$ are from work by Jeitschko et al. [8].The GGA-PBE XC functional was employed for $CaFe_2As_2$, while the LDA XC functional was employed for $LaRu_2P_2$.

Compound	Length	Experiments	DFT
$CaFe_2As_2$	a	5.542 Å	5.60 Å
	b	5.465 Å	5.49 Å
	c	11.644 Å	11.48 Å
$LaRu_2P_2$	a	4.031 Å	3.99 Å
	c	10.675 Å	10.52 Å

Adding the U correction to the LDA XC functional (LDA+U) can, indeed, stabilize the magnetic moments of the iron atoms. However, only large magnetic moments (greater than those stabilized by PBE) can be achieved in a relaxed crystal. The smallest of which was 2.18 μ_B (with a $U_{eff} = 2$) and had a c-axis length of 10.85 Å. Since this deviates significantly from the experimental lattice parameters and a provides a gross overestimation of the magnetic moments, further use of the LDA+U is not examined in this work. The Hubbard U corrections to LDA and PBE XCs demonstrate that applying this correction cannot improve the accuracy of the predictions of

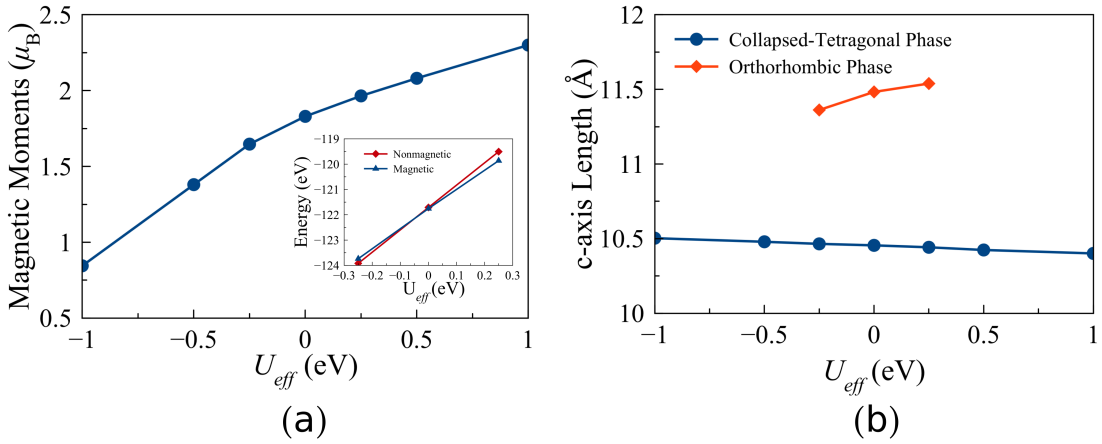

Figure 12: (a) Magnetic moments and (b) c-axis lengths of $CaFe_2As_2$ as computed with the GGA+U XC-functional. The magnitude of the magnetic moments of the iron atoms can be manipulated by controlling the U parameter. However, the orthorhombic phase can only be structurally stabilized for a small range of U values. While applying a negative U_{eff} can decrease the magnetic moments, the magnetic phase may not be energetically favored (a) insert.

the phase transitions in $CaFe_2As_2$. However, based on these results it is clear that uncertainty in these parameters amounts to a few percent error in predicting transition properties.

3.1.3 $CaFe_2As_2$ Compression Simulation Results

The compression of $CaFe_2As_2$ unit cells offers insight into the mechanical response which has not be previously reported. While $CaFe_2As_2$ has been investigated extensively in hydrostatic loading [11, 20, 30, 42] and partially in uniaxial loading [20, 30], those results lack the fidelity to fully parameterize the response. The compression simulations performed for our work are strain-controlled to provide a more complete view of the stress-strain response of $CaFe_2As_2$. With that in mind, Figures 13 and 14 plot the response of the $CaFe_2As_2$ under uniaxial and hydrostatic loading, respectively.

In the case of uniaxial loading (Figure 13(a)) the orthorhombic structure loads elastically up to about 5% where it then softens until reaching a maximum around 6% strain. At approximately 7.75% strain the magnetic moments disappear and the structure collapses into the collapsed tetragonal structure. Further straining of the structure elastically loads the collapsed tetragonal structure.

These results are the first to provide a full stress-strain response of the $CaFe_2As_2$ material under uniaxial straining, which is key in developing continuum thermodynamic material models of these materials. Similarly, energy versus c-axis strain (Figure 13(b)), lattice constants (Figure 13(c)), and magnetic moment (Figure 13(d)) are also functions of the uniaxial strain, showing clear phase instabilities at the critical strain. On the surface, this contrasts the macroscopic observation of a first-order phase transition. However, in simulating of a single unit cell under fully periodic boundary conditions at 0 K, a phase change would not be expected until the first phase became energetically unstable.

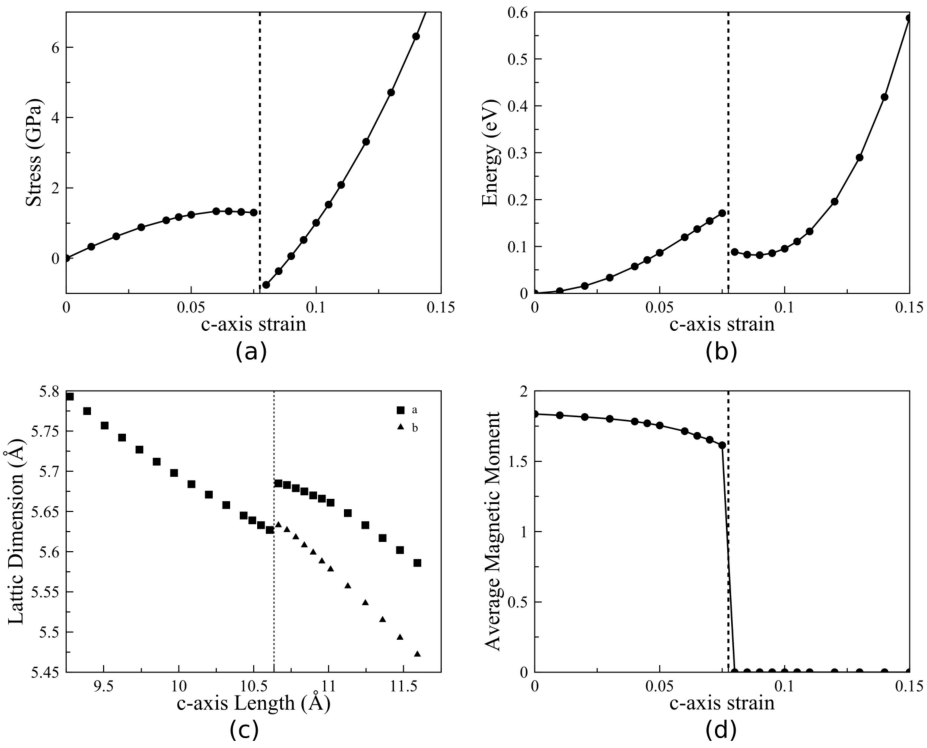

Figure 13: Stress-strain (a) and energy-strain (b) response of a single $CaFe_2As_2$ unit cell. Note the abrupt phase transition resulting in negative stress at the transition strain. The a and b lattice constants abruptly converge upon c-axis compression (c).

The uniaxial behavior can be contrasted with the hydrostatic results (Figure 14) which illustrates a similar discontinuity in the pressure-volume curve. However, if the results are plotted as a function of the c-axis strain (Figure 14(a)), there is an interesting phenomenon not previously

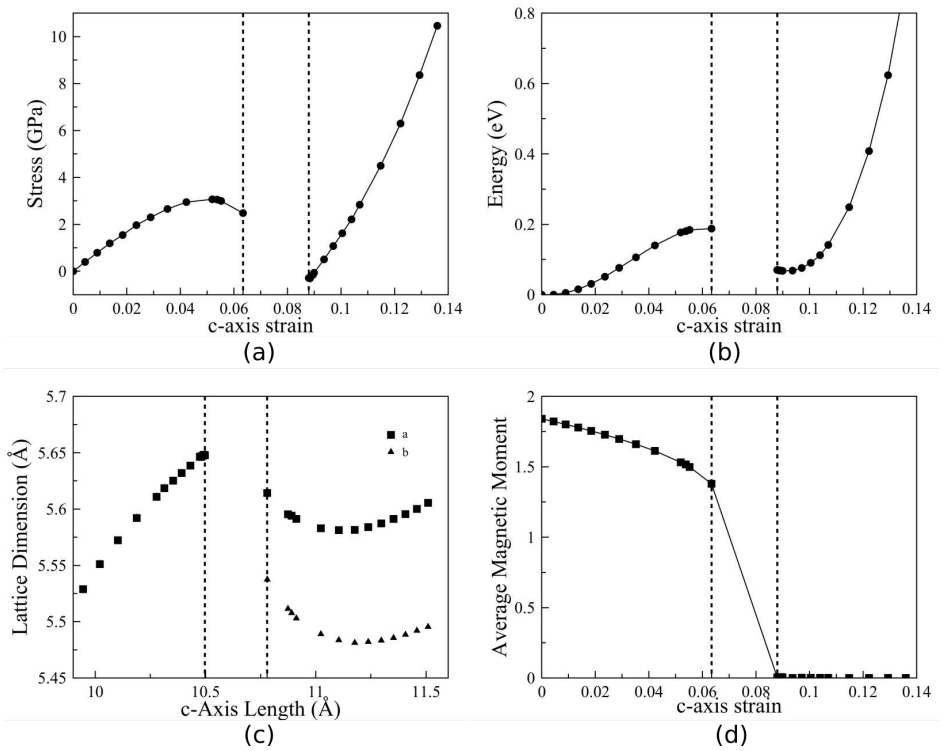

Figure 14: Stress-strain (a) and energy-strain (b) response of a single $CaFe_2As_2$ unit cell under hydrostatic compression. Here, the phase change causes a jump in c-axis strain, leaving a range of strains inaccessible. There is a region of inaccessible c-axis lengths across the phase change (c). The magnetic moments abruptly drop to 0 at the phase change.

reported. There is a forbidden zone of c-axis values, or essentially a c-axis gap. The plot of hydrostatic stress versus c-axis strain appears in shape similar to the uniaxial case with a linear increase in stress up to 5% strain and a softening between 5% and 6.5% strain. The c-gap prevents any results being investigated between roughly 6.3% and 8.8% strain, over which the magnetic moments disappear and the phase transition occurs. What is further interesting is that the midpoint of the gap is roughly 7.6%, which is the c-axis strain at which the phase transition sharply occurs in uniaxial loading. This observation is consistent with our other results and findings of other groups [30] and suggests that it is the c-axis strain that controls the collapse of the crystal structure.

3.2 Compression Simulations of $LaRu_2P_2$

A similar compound, $LaRu_2P_2$, was investigated for its possible pseudo-elastic mechanical response. Previous studies have indicated the presence of a collapse along the c-axis similar to that of $CaFe_2As_2$. Both DFT simulations [12, 13] and experimental compression [12, 19] have been performed previously. The nature of this mechanical response was investigated in more depth in this thesis.

3.2.1 Selection of the Exchange-Correlation Functional

The compression of $LaRu_2P_2$ revealed a pseudo-elastic response which is characteristically different than that of $CaFe_2As_2$. While more discussion on these findings will be presented in the following sections, the XC-functional was chosen based on geometric and mechanical parameters. The pseudo-elastic behavior, based on strain in the c-axis, is obviously the most important feature to be extracted from these simulations. The XC-functional was chosen based on its ability to predict the c-axis length of the crystal and the pseudo-elastic transition strains. These parameters were

Table 3: Geometric and pseudo-elastic parameters produced by both the local density approximation (LDA) and generalized gradient approximation Perdew-Burke-Ernzerhof (PBE) exchange correlation functionals. LDA does a much better job of reproducing the c-axis length of the conventional unit cell and the pseudo-elastic transition strains in hydrostatic compression. Experimental data is from Drachuck et al. [19].

Method	a	c (Å)	ε_1	ε_1
PBE	4.05	10.91	0.055	0.090
LDA	3.99	10.52	0.025	0.058
Experiments	4.03	10.68	0.024	0.065

computed for both the LDA and PBE XC-functionals and compared against hydrostatic compression experiments conducted by Drachuck et al. [19]. LDA predicts an equilibrium c-axis length of 10.52 Å, while PBE predicted 10.91 Å. LDA also predicted the transition strains to be 2.5% and 6.5%, while PBE predicted 5.5% and 9.0%. As highlighted in Table 3, the values predicted by LDA were much closer to experiments than those predicted by PBE. For this reason, LDA was used as the XC-functional for all $LaRu_2P_2$ investigations in this work.

3.2.2 $LaRu_2P_2$ Compression Simulation Results

Since $LaRu_2P_2$ is not magnetic, its unstressed crystal structure is the classic tetragonal $ThCr_2Si_2$ structure. This initial unit cell was compressed incrementally up to high strains (10%) in the same procedure as the $CaFe_2As_2$. Both uniaxial compression (Figure 15) and hydrostatic compression (Figure 16) were performed. In this case, there is no obvious (1st-order) phase transition. The stress, energy and lattice constants appear as smooth functions of the applied strain in both compression cases. However, it is interesting to note the stress-strain curves have softened regions (Figure 15(a), 16(a)) with a local maximum and minimum, while the energy has two associated points of inflection, but no local energy minimum (Figure 15(b), 16(b)). The max stress and min stress are observed to occur at 4% and 5% c-axis strain, respectively, for both uniaxial and hydrostatic loading conditions, again highlighting the role of the c-axis length in controlling the nature of the mechanical response.

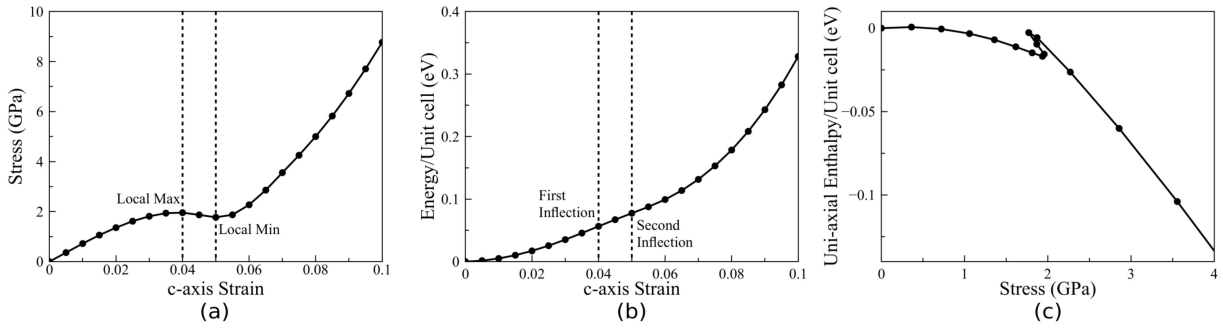

Figure 15: The uniaxial stress-strain response (a) of $LaRu_2P_2$ shows a softened region bounded by two more conventional regions. Since this strain is recoverable, it suggests that there is a phase change present. However, the energy-strain response (b) does not have a local minimum which would indicate an obvious phase bifurcation. A discontinuity in the uniaxial enthalpy-stress response (c) highlights the two "phases" with distinct mechanical characteristics.

While there was no local energy minimum observed in $LaRu_2P_2$ and thus no indication of two true thermodynamics phases, there was an observed discontinuity in another thermodynamic potential. Under uniaxial loading, an enthalpy-like thermodynamic potential (per unit cell) defined as $H^* = E - Fc$ should be considered. Here, E is the energy per-unit-cell, F is the applied load

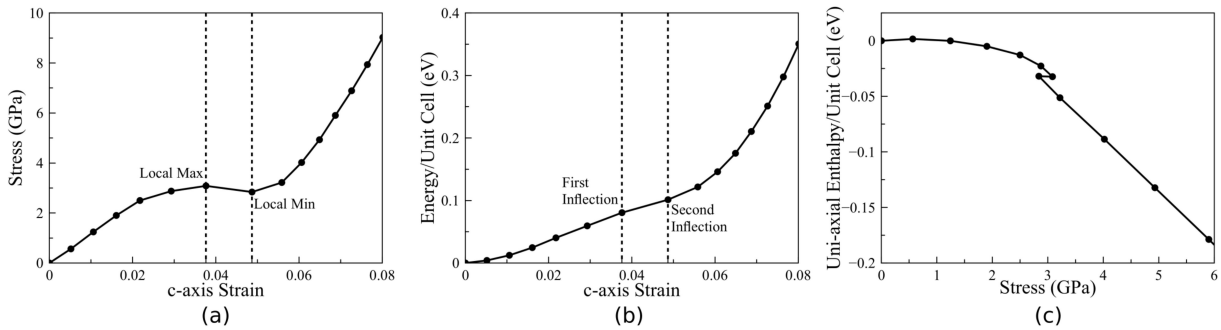

Figure 16: Like the uniaxial compression, hydrostatic stress-strain response (a) of $LaRu_2P_2$ shows a softened region but there is no local energy minimum (b). The uniaxial enthalpy-stress response (c) shows a discontinuity similar to the one observed in the uniaxial compression.

(stress $\times$ currrent area) and c is the unit-cell c-axis length. Plotting this "uniaxial enthalpy" vs. load reveals a discontinuity (Figure 15(c), 16(c)) which highlights two potential "phases" in which $LaRu_2P_2$ could exist under load-control. While subtle, there is a small section of overlap which allows the uniaxial enthalpy to be multi-valued under load-control conditions. This implies a strain discontinuity during load-control experiments. This behavior is also observed in the hydrostatic response of $LaRu_2P_2$.

3.2.3 Evolution of the Elastic Constants of $LaRu_2P_2$

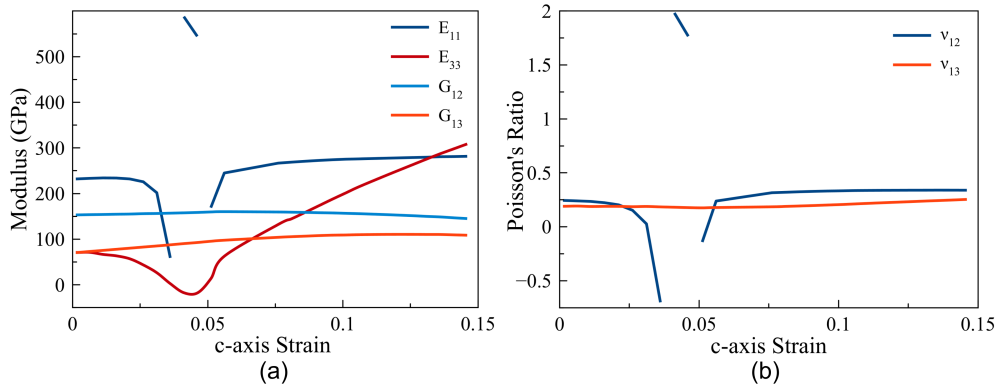

Figure 17: The evolution of the 6 tetragonal elastic constants during the uniaxial compression of $LaRu_2P_2$. E_{11} and ν_{12} exhibit a discontinuity during the crystal collapse.

It is interesting to look at how the elastic constants change through the mechanical response of the crystal. This was accomplished by computing the elastic constants for the $LaRu_2P_2$ unit cell at each point along the uniaxial compression curve. While some elastic constants responded with smooth changes throughout the compression, others experienced discontinuities. The elastic constants plotted against strain can be seen in Figure 17. Of the 6 elastic constants for crystal cells with tetragonal symmetry, three evolved in uneventful ways. The two shear moduli (G_{12} and G_{13}) and ν_{13} hardly change throughout the compression. Meanwhile, ν_{12} and E_{11} experience discontinuities during the collapse transition, between 4% and 5% c-axis strain. The Young's modulus in the c-direction, E_{33}, is continuous and decreases during the crystal collapse, corresponding to the softening observed in the stress-strain response. The modulus does indeed dip below 0, which is expected as the stress-strain curve has a negative slope here. This discontinuity in the elastic constants is indicative of a 2nd-order phase transition. This is in contrast to $CaFe_2As_2$ which exhibits a 1st-order phase transition. The elastic constants are the 2nd derivative of energy with respect to volume, and there is discontinuity in the E_{11} and ν_{12}.

3.3 Discussion

The DFT simulations of individual unit cells highlight properties of the observed crystal collapse. For a given compound, both the hydrostatic and uniaxial loading scenarios show a collapse at consistent c-axis strains. A unit cell of $CaFe_2As_2$ under uniaxial loading collapses at 7.5% c-axis strain while the collapse in hydrostatic loading occurs for c-axis strains between 6.4% and 8.4% with a mean of 7.4%, consistent with the uniaxial case.

It is important to note that the phase transition in $CaFe_2As_2$ corresponds with an abrupt loss of magnetism in the crystal. While the magnetic nature of the phase transition has been previously reported, it has also been suggested that phase transitions in $ThCr_2Si_2$-type crystals are due, in part, to the bonding between vertically stacked pnictogen atoms under compression [17]. Similarly, the local maximum of the $LaRu_2P_2$ unit cell is 4.0% and 3.8% for uniaxial and hydrostatic loadings respectively, and the local minimum is 5.0% and 4.9% respectively. This consistency supports the

hypothesis that the c-axis strain is the critical parameter of the phase transition. However, these observations leave one important question: does the consistency of c-axis collapse appear in a continuous phase transition observed in the experiments?

3.4 Bonding Between Pnictogen Atoms

Both $CaFe_2As_2$ and $LaRu_2P_2$ experience a softening when compressed along their c-axes. Studies of other 1:2:2 intermetallic compounds with the $ThCr_2Si_2$-type crystal structure have also been shown to exhibit softening as well. It was suggested by Hoffmann and Zheng that this softening is caused, in part, by the bonding of pnictogen (Nitrogen, Phosphorus, Arsenic, etc.) atoms across A-atom layers [17]. Since our investigations rely heavily on electronic structure calculations, we can explore the bonding nature of these crystals under pressure. To investigate this, we employed several analytical methods, including Bader charge analysis, the electron localization function, and Crystal Orbital Hamilton Populations, to characterize the interactions of the pnictogen atoms. Indicators of bonding between these atoms should shed light on the origins of the observed softening.

3.4.1 Bader Charge Analysis

The literature has highlighted the importance of the B–X layers in the phase-change mechanism of these materials. In addition to bonding between these layers, $CaFe_2As_2$ also exhibits magnetic phases. Upon collapse, all magnetic moments also vanish. Since the crystal is often described as alternating layers of Ca cations and Fe_2As_2 anions, it is interesting to see if there is any charge transfer between the As and Fe atoms in conjunction with the collapse of the magnetic moments on the Fe atoms. There may also be charge transfer from the Ca layers to the B–X layers.

If these materials were to form Pn–Pn covalent bonds in the cT phase, as has been suggested, one would expect some transfer of electrons to/from the pnictogen atoms in the cell. The electronic structure would need to change in ordinance with the new sharing of electrons between pnictogen atoms. One way to investigate this is through Bader Charge Analysis (BCA). The division of

atoms is not well defined in DFT simulations. Since the individual electrons are simulated as wave functions within the simulation cell, they are not tied to or defined to have any particular parent atomic nucleus. Additionally, DFT operates with the electronic density, which is a superposition of all the wavefunctions. When looking for bonding, electrons must be *shared* between atoms, and thus, must be assigned to atoms in some capacity. Richard Bader developed a method to assign electrons to atoms by analyzing the charge density computed in the DFT simulation [101]. He postulated that a surface of minimum charge density, and thus zero charge gradient, between ionic center points would define a boundary between atomic volumes. Within each volume bound by these surfaces, one can integrate to a total electron population associated with that atom.

It is important to note that the accuracy of the integration is dependent on the mesh by which the charge density is reported. In order to assure that the results of Bader Charge Analysis (BCA) are reliable, it is important to take special care in choosing the FFT mesh which the charge density is reported.

Furthermore, it is often suggested that these materials exist in alternating layers of A cations and B_2X_2 anion cages [17]. This ionic charge distribution can be validated with BCA. Unstressed and stressed crystals of both $CaFe_2As_2$ and $LaRu_2P_2$ were relaxed and BCA was performed to determine the electronic distribution within the crystal. The layered ionic nature of the crystals was confirmed with BCA. It was calculated that the A atoms indeed had a positive overall charge. In unstressed $CaFe_2As_2$ and $LaRu_2P_2$, calcium atoms each have a charge of $+1.39$ and lanthanum atoms have a charge of $+1.52$, respectively. This similarity in charge makes sense considering that calcium and lanthanum have electronegativities of 1.0 and 1.1, respectively [102].

The B–X cages were also shown to have an overall negative charge (equal in overall magnitude to the A-layer charge). However, the distribution of charge within the cage differed between the two compounds. The iron atoms in unstressed $CaFe_2As_2$ had charges of $+0.20$, while the ruthenium atoms in unstressed $LaRu_2P_2$ had charges of -0.21. Likewise, the arsenic atoms had charges of -0.90 while the phosphorus atoms had charges -0.55 in the unstressed crystals. This charge distribution can also be rationalized in the context of the elements' electronegativities. Arsenic and

phosphorus have similar values, 2.18 and 2.19, respectively [102]. However, iron and ruthenium have the most significant discrepancy in this comparison, iron has an electronegativity value of 1.83, while ruthenium has a value of 2.2 [102]. This suggests that ruthenium would be charged significantly more negatively than iron, which agree with the results from BCA.

BCA of the stressed crystals shows that there is little charge transfer to/from the A atoms upon compression. Stressed calcium atoms had charges of $+1.37$, which is an overall change of -0.02. However, there is an overall charge transfer from the iron atoms. In the unstressed (and antiferromagnetic) crystal, iron atoms have a charge of $+0.20$, while when stress is applied, that charge drops to $+0.03$. This “gain" of 0.17 of a fundamental charge may explain how the iron atoms lose their magnetic moments upon crystal collapse.

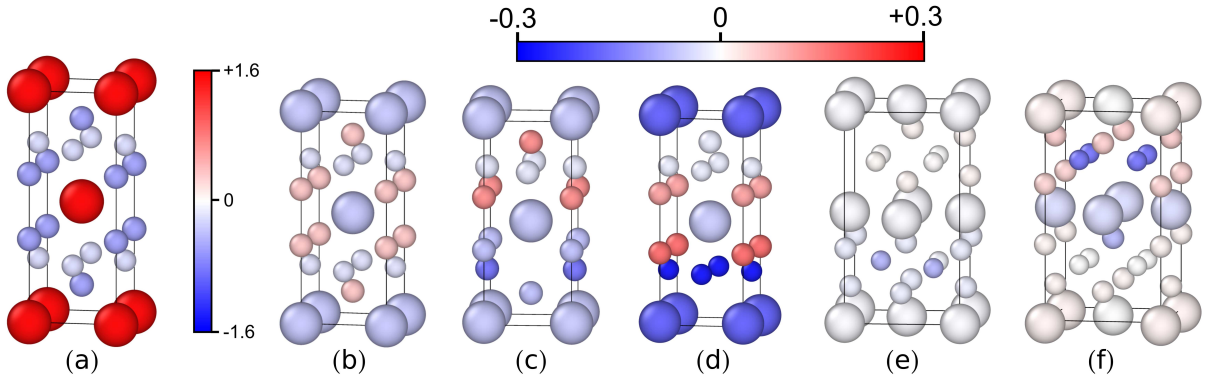

Figure 18: The results of Bader Charge Analysis on $LaRu_2P_2$. (a) The uncompressed charge distribution predicts positively charged La atoms and a negatively charged Ru–P cages. (b) Compressing $LaRu_2P_2$ into its collapsed state yields a slight electron transfer from the P atoms to the Ru atoms. Removing one out of every four ruthenium atoms (c), or one of every four phosphorus atoms (d) causes a charge redistribution as well as a crystal collapse. Removing one of every eight ruthenium atoms (e), or phosphorus atoms (f) induces a much less dramatic charge redistribution.

Likewise, in $LaRu_2P_2$, lanthanum atoms also had an overall positive charge. In the unstressed crystal each had a charge of $+1.52$, while in a stressed crystal, they each had a charge of $+1.46$. This difference of -0.06 However, the charge difference on the ruthenium atoms in $LaRu_2P_2$ was not as pronounced as that of the iron atoms in $CaFe_2As_2$. Ruthenium atoms in an unstressed crystal had an overall charge of -0.21, while in the stressed crystal, they had a charge of -0.26.

The phosphorus atoms also experienced a less dramatic charge transfer (-0.55 to -0.43) than the analogous arsenic atoms in $CaFe_2As_2$. This lack of charge transfer, when compared to $CaFe_2As_2$, may explain the lack of first order phase transition.

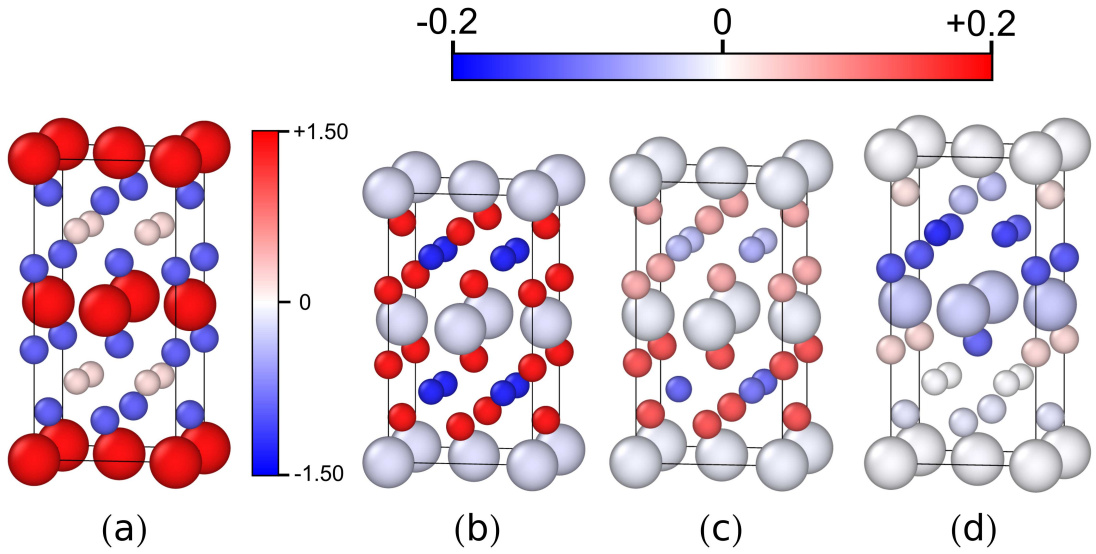

Figure 19: The results of Bader Charge Analysis on $CaFe_2As_2$. (a) The charge distribution of the uncompressed orthorhombic phase predicts positively charged Ca atoms and a negatively charged Fe–As cages. The arsenic atoms are initially negatively charged, while the iron atoms are initially positively charged. (b) When compressed into the collapsed-tetragonal phase, charge shifts from the arsenic atoms to the iron atoms. (c) Removing one of every eight iron atoms induces a similar charge shift within the cage as compressing the crystal, and this structure is significantly shorter than the unstressed, pristine crystal. (d) Removing one of every eight arsenic atoms does not collapse the crystal, and other atoms near the vacancy take on negative charge.

Defected $LaRu_2P_2$ structures were also analyzed with BCA. These structures, which are explained in more detail in Section 4.1, included supercells with ruthenium vacancies and supercells with phosphorus vacancies. Supercells where 1 of 4 ruthenium or phosphorus atoms were removed (25%), and 1 of 8 were removed (12.5%) were relaxed and BCA was performed on them. In the defected structures, the lanthanum charge was not significantly changed, but the charges on the ruthenium atoms was changed. Regardless of whether a ruthenium vacancy or a phosphorus vacancy was simulated, the charge on one of the remaining ruthenium atoms changed. In the 25% vacancy structures, one of the ruthenium atoms had a charge of -0.43 (compared to -0.22 in the

pristine crystal), and in the 12.5% vacancy structures, one of the ruthenium atoms had a charge of -0.33. Meanwhile, the charge on the phosphorus atoms remained unchanged. This makes sense considering the nonmetal nature of phosphorus in contrast to the metallic nature of ruthenium.

Defected $CaFe_2As_2$ structures were analyzed with BCA to investigate the effect of defects on the charge of the atoms. In a similar manner to the $LaRu_2P_2$ defect structures, 1 of 8 iron atoms, or 1 of 8 arsenic atoms (12.5%) were removed. These structures were relaxed and BCA was performed to calculate the change in charge from the non-defected, uncompressed state. The results of the BCA can be seen in Figure 19. They highlight that in the compressed state, there is a clear charge transfer of 0.17 e^- from the arsenic atoms to the iron atoms (Figure 19(b)). The removal of one iron atom (12.5% vacancy concentration), induces a similar charge transfer in both the defected cage, and the cage without a defect. This charge transfer is accompanied by a reduction in the c-axis length of the crystal, from 11.52 Å to 10.65 Å. However, the charge transfer which is due to an arsenic vacancy is quite different. The surrounding atoms, regardless of element, take on extra negative charge. Some phosphorus atoms very far away from the vacancy take on a slightly more positive charge. The c-axis length of this crystal is also relatively unchanged, 11.53 Å, from the pure, uncompressed crystal.

3.4.2 Electron Localization Function

A useful measure of bonding is the electron localization function (ELF). The ELF is the probability of finding a given electron, provided its opposite-spin paired electron is known to be there [103]. The result is a measure of how localized the electrons are. High ELF values are attributed to lone pairs and bonded pairs, while low ELF values indicate regions with low probability of finding a second electron at all. Investigations of compounds with the $ThCr_2Si_2$ crystal structure with ELF have shown bonding between the transition metal atoms [104].

ELF values were calculated for the uncompressed unit cells and the collapsed unit cells. We find that the regions surrounding the pnictogen atoms of ELF > 0.5, which correspond to some degree of electron pairing, do not overlap. It is likely that here we have opposing lone pairs.

Table 4: Charges on atoms in $LaRu_2P_2$ and $CaFe_2As_2$ structures analyzed with Bader Charge Analysis.

Structure	Charge					
	A	Δ	B	Δ	X	Δ
$LaRu_2P_2$ (unstressed)	$+1.52$	$-$	-0.21	$-$	-0.55	$-$
$LaRu_2P_2$ (stressed)	$+1.46$	-0.06	-0.24	-0.03	-0.49	0.06
$LaRu_{1.5}P_2$ (Ru vac)	$+1.46$	-0.06	-0.36	-0.15	-0.62	-0.07
			-0.23	-0.02	-0.42	$+0.13$
$LaRu_2P_{1.5}$ (P vac)	$+1.46$	-0.06	-0.47	-0.26	-0.57	-0.02
	$+1.34$	-0.18	-0.23	-0.02	-0.39	$+0.16$
					-0.45	$+0.10$
$LaRu_{1.75}P_2$ (Ru vac)	$+1.51$	-0.01	-0.29	-0.08	-0.57	-0.02
			-0.22	-0.01	-0.54	$+0.01$
			-0.21	± 0.00		
$LaRu_2P_{1.75}$ (P vac)	$+1.48$	-0.04	-0.36	-0.15	-0.62	-0.07
	$+1.51$	-0.01	-0.21	± 0.00	-0.54	$+0.01$
	$+1.53$	$+0.01$			-0.50	$+0.05$
$CaFe_2As_2$ (orthorhombic)	$+1.39$	$-$	$+0.20$	$-$	-0.90	$-$
$CaFe_2As_2$ (collapsed tetragonal)	$+1.37$	-0.02	$+0.03$	-0.17	-0.72	$+0.18$
$CaFe_{1.75}As_2$ (Fe vac)	$+1.28$	-0.11	$+0.09$	-0.11	-0.77	$+0.13$
			$+0.10$	-0.10	-0.84	$+0.06$
			$+0.14$	-0.06		
			$+0.16$	-0.04		
$CaFe_2As_{1.75}$ (As vac)	$+1.36$	-0.03	$+0.07$	-0.03	-1.03	-0.13
	$+1.39$	± 0.00	$+0.20$	± 0.00	-1.00	-0.10
					-0.95	-0.05
					-0.90	± 0.00
					-0.89	$+0.01$
					-0.85	$+0.05$

Meanwhile in the collapsed crystal state, these regions do overlap. This would suggest that some level of bonding is occurring between these atoms.

3.4.3 Crystal Orbital Hamilton Population

The crystal orbital Hamilton population (COHP, read “co-hop") calculates the bonding-or-antibonding attribute of the electron bands [105, 106]. A negative COHP value indicates that that electron state is a bonding state, while a positive COHP value indicates that an electron at that state is in an antibonding state. COHPs near zero do not contribute to bonding between the atoms for which the COHP was calculated. When searching for ground state bonding, the COHP level up

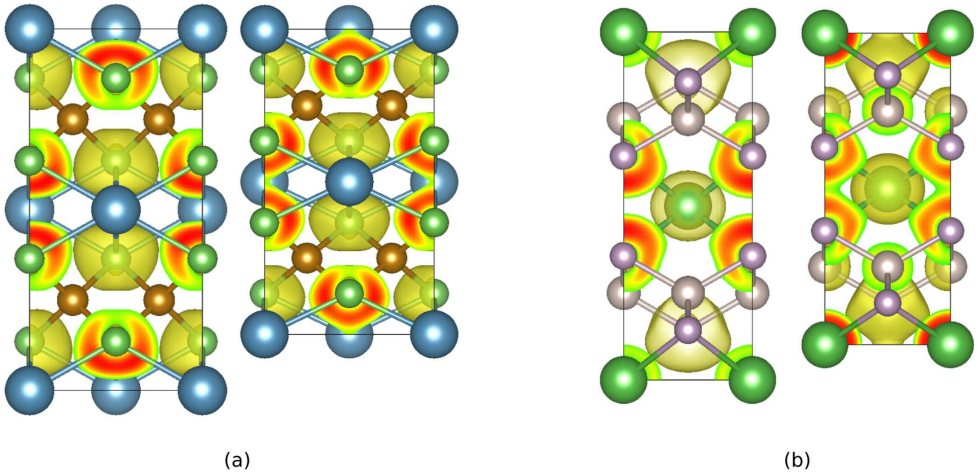

Figure 20: The electron localization function 0.5 iso-surfaces highlight the bonding between the pnictogen atoms upon crystal collapse.s

to, and at the Fermi level is the focus. If the states near the Fermi level have a negative COHP, the two atoms are most likely bonded. Meanwhile a positive COHP at the Fermi level would be indicative that the two atoms are not well bonded. All COHP calculations in this work are performed with the LOBSTER (Local-Orbital Basis Suite Towards Electronic-structure Reconstruction) code developed by Maintz et al [107].

Another useful measure of bonding is the crystal orbital hamiltonian population (COHP) [105]. The most telling COHP values are in the region of energy bands leading up to the fermi level (e_f). COHP values in this region indicate the bonding state of electrons occupying these energy levels (the valence electrons at ground state). Negative COHP values imply electrons are in bonding states, while positive COHP values imply electrons are in antibonding states.

The COHPs between vertically aligned pnictogen atoms were calculated for $LaRu_2P_2$ and $CaFe_2As_2$ at various key strains.The unstressed state COHP was calculated for both compounds. COHPs were also calculated for the strain states immediately before and immediately following the $CaFe_2As_2$ phase change. COHPs were calculated for the local minimum and local maximum of the stress-strain $LaRu_2P_2$ curves.

The unstressed states of both $LaRu_2P_2$ and $CaFe_2As_2$ show a fair amount of antibonding near the fermi level (Figure 21). When the orthorhombic cell is strained just before the phase change,

this antibonding is also observed. Very near the fermi level, the COHP values increased, indicating a strengthening of antibonding. However, upon transitioning to the collapsed phase, the COHP values near the fermi level decrease dramatically. There is a large band of bonding states, and only a small, slightly-antibonding band at the fermi level. Although the COHPs do not prove that the As atoms are perfectly covalently bonded, this highlights that the As atoms are measurably more bonded in the collapsed state than in the orthorhombic state.

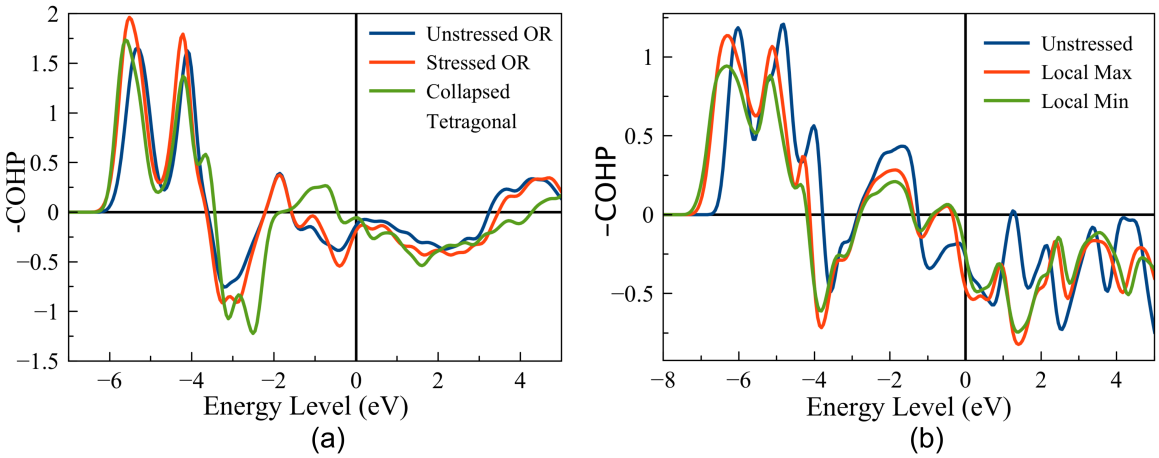

Figure 21: The evolution of the COHP between arsenic atoms in $CaFe_2As_2$ (a) and phosphorus atoms in $LaRu_2P_2$ (b) clearly shows a decrease in anti-bonding as the crystal collapses.

Likewise, the stressed $LaRu_2P_2$ unit cells show a striking decrease in antibonding bands. Both the local minimum and maximum have a band of bonding and only a small band antibonding right at the fermi level. This is indicative of an increase in P bonding along the c direction. Furthermore, there is slightly more bonding and slightly less antibonding at the local minimum compared to the local maximum. This implies that the local minimum is slightly more bonded than the local maximum.

The analysis of the COHPs between pnictogen atoms agrees with the results of the ELF calculations. In the collapsed state, the pnictogen atoms have some degree of covalent bonding. This bonding transition must contribute to the softening of the crystals.

3.5 Elemental Contributions to the Crystal Collapse

The nature of the phase changes of $CaFe_2As_2$ and $LaRu_2P_2$ are strikingly different. While both result in a macroscopic pseudo-elastic effect, $CaFe_2As_2$ undergoes an abrupt phase change due to the loss of magnetic moments, but $LaRu_2P_2$ exhibits no such magnetism or abrupt phase change. Certain intuition would point to the fact that the cause may be the magnetism of iron, in contrast to the lack of magnetism of ruthenium. However, while much study is left to be completed in this area, the iron-arsenides have been reported to have stronger magnetism than iron phosphides. Additionally, the As–As bond length (2.46 Å [108]) is significantly shorter than the P–P bond length (2.8 Å [13]). This shorter bond length may facilitate a more drastic crystal collapse. The iron in $CaFe_2As_2$ is magnetic when the crystal is not compressed. In the orthorhombic phase, the magnetic moments are arranged in an antiferromagnetic pattern and in the tetragonal phase, the moments are random and the crystal is paramagnetic. Only in the collapsed-tetragonal phase do the moments disappear, indicating that the phase change is both structural and magnetic. Between the B–X layers are layers of A cations. Upon crystal collapse the B–X layers are closer together, which would mean less space for the cations. Calcium, which has an ionic radius of 0.99 Å [109], exhibits a single, well-defined phase change. Meanwhile, lanthanum whose ionic radius is 20% larger than calcium (1.18 Å [109]), does not. Perhaps the larger size of lanthanum makes a phase change more difficult.

To investigate the individual elemental contributions to the mechanical response, compounds of all combinations of elements were simulated to provide direct comparisons. To state this more explicitly, $CaFe_2As_2$, $CaFe_2P_2$, $LaRu_2As_2$, $CaRu_2P_2$, $LaFe_2As_2$, $LaFe_2P_2$, $LaRu_2As_2$, and $LaRu_2P_2$ were all simulated in hydrostatic compression. This allows for the direct comparison of, for example, the roles of arsenic and phosphorus. The resulting stress-strain curves, as well as the magnetic moments, and the distances between select atoms in the crystal were analyzed.

Some of these compounds have been previously reported. The synthesis of $LaRu_2As_2$ has been accomplished [110] and has been studied with DFT for its ground-state crystallographic properties [111]. $LaFe_2P_2$ was synthesized to highlight the superconducting properties of $LaRu_2P_2$ in

comparison [112, 113]. $LaFe_2As_2$ has been reported to exhibit antiferromagnetic ordering similar to that of the other iron-arsenides, and has been studied as a pure compound [114] and as an

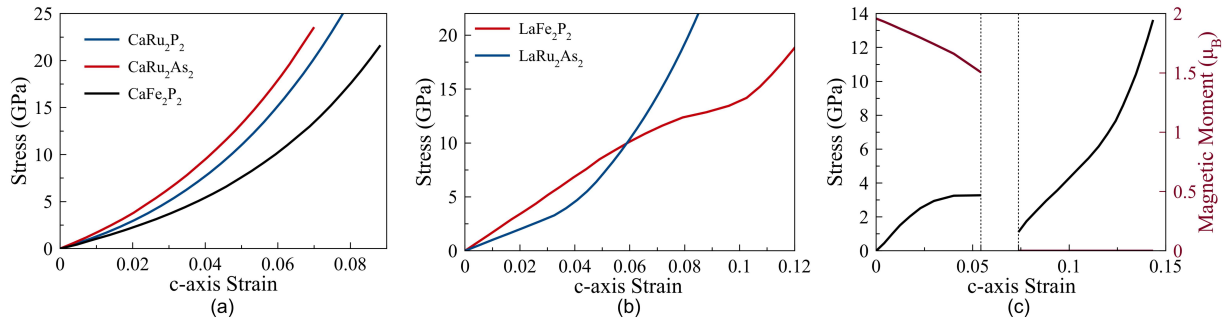

Figure 22: The hydrostatic stress-strain curves of the ternary intermetallic combinations of Ca, La, Fe, Ru, As and P. (a) The stress-strain responses of the Ca-based compounds which are not $CaFe_2As_2$ are elastic with no phase change. (b) The nonmagnetic La-based compounds ($LaFe_2P_2$ and $LaRu_2As_2$) exhibited characteristic continuous pseudo-elastic behavior. (c) The magnetic compound, $LaFe_2As_2$, exhibited a discontinuity in its stress-strain response upon the magnetic collapse of the crystal.

The stress-strain responses of the $LaRu_2As_2$, $CaRu_2P_2$, and $CaFe_2P_2$ are all devoid of characteristics indicative of pseudo-elasticity, shown in Figure 22(a). However, the La-based compounds have interesting stress-strain responses. The response of $LaFe_2P_2$ exhibits clear softening around the 8% strain mark, followed by stiffening after 10% strain. The response of $LaRu_2As_2$ has a linear stress-strain response until 4% strain, and then exhibits a stiffer response for higher strains. These responses can be seen in Figure 22(b). $LaFe_2As_2$, the only magnetic compound of the six investigated, exhibits a magnetic collapse at a c-axis strain of approximately 5.5%. The crystal transitions to its collapsed tetragonal state, with a c-axis gap similar to that observed in $CaFe_2As_2$, at about 7.5%. Unlike $CaFe_2As_2$, upon transition, the collapsed tetragonal phase is in a state of compression (Figure 22(c)).

Looking into the internal geometry of the crystal, we can characterize how the strain is distributed throughout the crystal. The vertical distance between the B and X layers of the cage is a measure of how much strain is accommodated within the cages. Likewise, the vertical distance between pnictogens of different cages can highlight the collapse of the crystal. Interestingly, abrupt

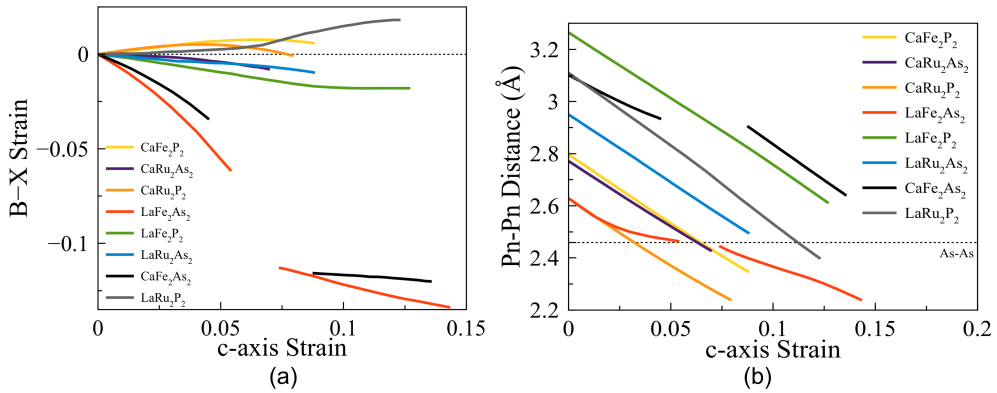

Figure 23: Distances between select atoms during the compression of the ternary intermetallic compounds. (a) The strain between the B and X layers within the cage as a function of total c-axis strain, and (b) the distance between vertically-stacked pnictogen atoms as a function of c-axis strain.

phase transitions with a crystal collapse are accompanied by a jump in the B–X vertical distance (Figure 23(a)). Compounds which do not exhibit such a crystal collapse have continuous B–X distances, as well as a linear relationship between Pn–Pn distance and c-axis strain (Figure 23(b)). Leading up to the collapse, the Pn–Pn distance is nonlinear for $CaFe_2As_2$ and $LaFe_2As_2$, both compounds which exhibit an abrupt collapse. After collapse, the Pn–Pn distances respond differently to c-axis strain. It is interesting to note that $LaFe_2As_2$ exhibits a crystal collapse when the distance between As atoms is the As–As single-bond distance [108].

3.6 Multi-Phase Pseudo-Elastic Composite Model

While the DFT simulations performed in Section 3.1 and Section 3.2 outline the behavior of single unit cells of $CaFe_2As_2$ and $LaRu_2P_2$, respectively, and their fundamental dependence on c-axis deformation, it is critical to model these materials through their continuous phase transitions in large-scale samples. To this end, techniques used to model phase transitions in conventional shape memory materials are adapted to 1:2:2-superconductors. The fundamental idea behind this model, the details of which follow, is to find the equilibrium phase fractions of the two potential co-existing phases by minimizing the appropriate thermodynamic potential.

3.6.1 Construction of the Model

The continuum model considers a hypothetical mass of the material, capable of containing either or both phases and assumes that any secondary phase nucleates at point on the sample with a phase boundary perpendicular to the compression direction. As the compression is increased, the secondary phase grows consume the volume, while maintaining this phase boundary orientation. Thus any cross section perpendicular to the compression is composed of exactly one phase. The mass fraction of the first phase $\phi^{(1)}$ and the mass fraction of the second phase $\phi^{(2)}$ together, must account for the entirety of the modeled sample. Thus, conservation of mass yields the relationship:

$$\phi^{(1)} + \phi^{(2)} = 1 \tag{3.1}$$

The total length of the sample along the c-axis direction is always the sum of the c-axis lengths of the two individual phases:

$$L = L^{(1)} + L^{(2)} \tag{3.2}$$

The strain of the fraction of the sample in a given phase is referenced from the original (unstressed, orthorhombic) length of that material. This distinction is important since the collapsed tetragonal phase of $CaFe_2As_2$ has its own zero-stress c-axis length. The strains in each phase, by this definition, can be expressed by:

$$\varepsilon^{(i)} = \frac{L^{(i)} - \phi^{(i)} L_0}{\phi^{(i)} L_0} \tag{3.3}$$

So the total length can be represented as a function of the phase fractions and the individual strains as:

$$L = (\varepsilon^{(1)} + 1)\phi^{(1)} L_0 + (\varepsilon^{(2)} + 1)\phi^{(2)} L_0 \tag{3.4}$$

Furthermore, the total strain of the part as a function of the phase fractions and the individual strains can be expressed as:

$$\frac{L - L_0}{L_0} = \varepsilon = \varepsilon^{(1)}\phi^{(1)} + \varepsilon^{(2)}\phi^{(2)} \tag{3.5}$$

Equilibrium must also hold, and thus the stress in both phases is assumed to be equal:

$$\sigma = \sigma^{(1)} = \sigma^{(2)} \tag{3.6}$$

which will hold true if the area of the base of the unit cell remains roughly constant during the phase change.

3.6.2 Load Control vs. Displacement Control

The exact mechanical response of these materials depends on what is controlled during compression. In an experiment, what is controlled is either the applied load or the enforced displacement. Thermodynamically, the system should evolve to minimize different thermodynamic potentials for these different loading scenarios. A strain-controlled compression would correspond to the minimization of the total strain energy (u), while a uniaxial load-controlled compression would correspond to the minimization of the total uniaxial enthalpy (h^*). On a per-mass basis, these potentials are:

$$u = e^{(1)}\phi^{(1)} + e^{(2)}\phi^{(2)} \tag{3.7}$$

$$h^* = e^{(1)}\phi^{(1)} + e^{(2)}\phi^{(2)} - \sigma\varepsilon\frac{L_0}{L} \tag{3.8}$$

Under hydrostatic loading, the load-controlled compression would correspond to the minimization of the true enthalpy:

$$h = h^{(1)}\phi^{(1)} + h^{(2)}\phi^{(2)} = e^{(1)}\phi^{(1)} + e^{(2)}\phi^{(2)} + \sigma\left(V^{(1)} + V^{(2)}\right) \tag{3.9}$$

The last piece of the model is the phase fraction. To solve for this, polynomial splines were fit to the DFT data to obtain continuous expressions of the energies and stresses of each phase as functions of strain ($e^{(1)}(\varepsilon^{(1)})$, $e^{(2)}(\varepsilon^{(2)})$, $\sigma^{(1)}(\varepsilon^{(1)})$, $\sigma^{(2)}(\varepsilon^{(2)})$). From these equations and the individual-phase data from DFT, functions were defined which calculate the total strain-energy or uniaxial enthalpy, and stress with inputs of phase fraction and total strain. These thermodynamic potential functions

first calculate the stress which, for the given phase fraction, yields strains for each phase that satisfy Eqn. 3.5 for the provided total strain. The individual energies of each phase are calculated with the individual strains of each phase, and the appropriate thermodynamic potential is then calculated. For a specified total strain, the phase fraction which minimizes the appropriate thermodynamic potential, as calculated by the defined functions, is determined using, specifically, the golden-section search algorithm [115]. In order to build a full stress-strain curve, the strain is sequentially increased and the stress is determined for each point.

It is important to note that this model does not account for all aspects of phase change phenomena. For simplicity, there are several approximations made. The energy barrier of nucleating the secondary phase is ignored; secondary phases can nucleate without energy penalty. Strain mismatches between the phases and phase-boundary energy were ignored for this model. It is true that the nucleation of the second phase will produce these phenomena; they were neglected for this preliminary study.

The composite models allow us to understand the manifestation of the c-axis collapse in bulk stress-strain responses and make connections between the behavior of a single unit cell and the macroscopic responses of the bulk crystal. To this end, eight models were constructed to provide insight into the responses of $CaFe_2As_2$ and $LaRu_2P_2$. Each compound was modeled under both hydrostatic and uniaxial compression and both load-control and displacement-control scenarios were investigated for both compounds and loading scenarios. The stress-strain outputs of all eight composite models are shown in Figure 24.

Qualitatively for both compounds, these materials are stiffer under hydrostatic loading than uniaxial loading as measured agains the c-axis strain. Furthermore, within in the phase transition region, the load-control stress is consistently greater than the displacement-control stress and typically rises at a greater rate. The transition region for $CaFe_2As_2$ is much larger than the transition region for $LaRu_2P_2$ which is consistent with the unit cell responses of these materials and suggests there exists a wider range of strains for which the two phases exist in $CaFe_2As_2$ as compared to $LaRu_2P_2$.

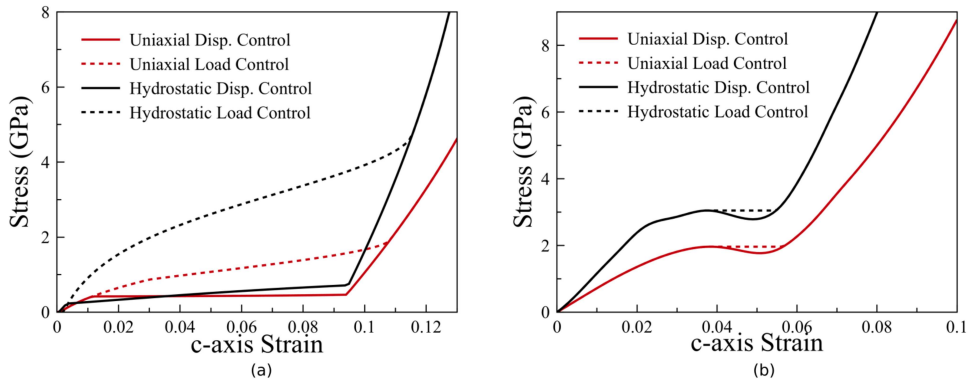

Figure 24: The uniaxial stress and hydrostatic stress vs. c-axis strain curves calculated by the composite model of $CaFe_2As_2$ (a) and $LaRu_2P_2$ (b) for all loading and control scenarios.

3.6.3 Comparison Parameters

To provide a quantitative means of cross-comparison between models and experiments, transition strains and moduli are extracted from all stress-strain curves. The are three “regions" present in the pseudo-elastic responses: the elastic response of 100% phase 1, the softened transition where both phases are present, and the elastic response of 100% phase 2. With this in mind, a tri-linear fit representing these states is applied to the full stress strain curve, allowing for the comparison of the response predicted by the models to the experimental results. It also gives a simple way to model the behavior, which can be described with only 5 parameters. The fit of the tri-linear model was computed by least-squares optimization.

The parameters of the tri-linear fit are two strains ε_1 (starting strain) and ε_2 (finishing strain), as well as 3 moduli (E_1, E_2, and E_3). The transition strains, ε_1 and ε_2, represent the points at which the phase transition begins and ends, respectively. The moduli E_1, E_2, and E_3 are the representative elastic moduli of the material in those regions. Figure 25 outlines the fitting results as well as the subsequent parameters.

3.6.4 Comparison with Experiments

To test the efficacy of the models, their predictions are compared to published experimental compression data of $CaFe_2As_2$ and $LaRu_2P_2$. Previous studies have experimentally investigated

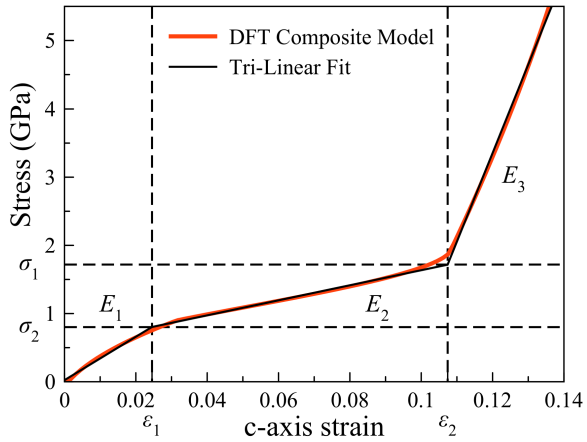

Figure 25: The tri-linear fit can be used to characterize the response of $ThCr_2Si_2$ crystals. Two transition strains: ε_1 and ε_2, and three moduli: E_1, E_2, and E_3, summarize the pseudo-elastic response for comparison.

the hydrostatic [44] and uniaxial [18] compression of $CaFe_2As_2$ as well as the hydrostatic compression of $LaRu_2P_2$ [19]. To the authors' knowledge, there are no published uniaxial compression experiments of pure $LaRu_2P_2$ (in Chapter 4 we present findings of investigations involving uniaxial compression of defected $LaRu_2P_2$). The outputs of the load control models are graphically compared to the experimental data in Figure 29 since the experiments were conducted in a load control setup. The models capture the general pseudo-elastic trends that are observed in the ex-

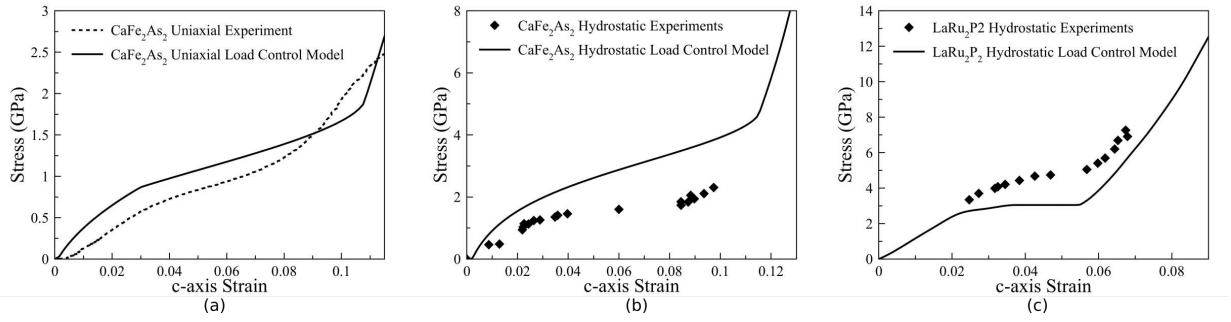

Figure 26: Comparison between experimental results and the DFT-based composite model of the uniaxial loading (a) and hydrostatic loading (b) of $CaFe_2As_2$, and the hydrostatic loading of $LaRu_2P_2$ (c).

periments. While the absolute stress values don't completely match, which is likely related to the perfect crystals simulated by DFT, the strains at which the transitions occur match reasonably well.

This qualitative comparison reveals interesting relationships, however, it s still desired to directly compare the experimental and computational results at this scale. The fitting procedure outlined in Section 3.6.3 performed for all response curves (model and experimental) and the calculated parameters are displayed in Table 5.

Table 5: Response characterization parameters for all loading scenarios calculated via the tri-linear fit. Stresses and elastic moduli are in units of GPa.

Compound	Loading	Control	ε_1	ε_2	σ_1	σ_2	E_1	E_2	E_3
$CaFe_2As_2$	hydrostatic	exp.	0.0290	0.0850	1.35	1.80	45.7	8.08	38.9
		disp.	3.40×10^{-3}	0.0973	0.246	0.755	86.0	5.43	229
		load	0.0210	0.113	1.87	4.39	80.5	27.4	276
	uniaxial	exp.	0.0270	0.0790	0.595	1.23	22.4	12.2	40.9
		disp.	0.0110	0.0940	0.414	0.456	38.5	0.502	106
		load	0.0250	0.107	0.802	1.72	31.8	11.0	129
$LaRu_2P_2$	hydrostatic	exp.	0.0240	0.0650	4.09	6.74	146	63.4	325
		disp.	0.0270	0.0570	3.01	2.70	114	-10.7	266
		load	0.0250	0.0580	2.95	3.10	117	4.68	270
	uniaxial	disp.	0.0310	0.0560	2.00	1.74	61.3	-10.7	132
		load	0.0300	0.0580	1.94	1.98	62.4	1.40	135

3.6.5 Discussion

With the as-determined transition strains from the continuum level models and experiments, it becomes possible to make quantitative comparisons between the models and experiments. The $LaRu_2P_2$ thermodynamic model simulations reveal displacement control critical c-axis strains of 2.7% and 5.7% for hydrostatic compression and 3.1% and 5.6% for uniaxial compression. These critical strains are similar to those calculated by the load control model, which are 2.5% and 5.8% for hydrostatic compression, and 3.0% and 5.8% for uniaxial compression. The experimental hydrostatic transition strains were found to be 2.4% and 6.5%, which are in reasonably good agreement with the modeling results despite the number of assumptions that were made in its development. This clearly demonstrates that a direct connection can be made between DFT simulations of a unit cell and the macroscopic observations made in experiments.

The numerical agreement between the thermodynamic model and the experiments for $CaFe_2As_2$ is less convincing, especially for the displacement control simulations. The hydrostatic displacement control simulations give a starting strain of 0.34% while the load control gives 2.1%, the uniaxial displacement control is 1.1% and the load control is 2.5%. The fits to experimental data give 2.9% for hydrostatic and 2.7% for uniaxial. This suggest that the load controlled models agree much better with experimental results than the displacement controlled results. However, the finishing strains exhibit trends that the experimental results are lower than the displacement controlled model which is lower than the load controlled model, suggesting the displacement controlled simulations better model the finishing strains. This suggests, as do the actual curves, that the experimental results lie between the two idealized models.

This comparison is, of course, between simulations at 0 K and experiments at room temperature. While the displacement control $CaFe_2As_2$ model predicts the phase transition stress at 0 K, experimental studies have shown that there is most certainly a relationship between σ_c and T [16]. Temperature dependence of critical stress is not addressed by this model, but will be discussed in Section 3.6.6.

It is worth noting that in $CaFe_2As_2$ there is a non-trivial difference in the starting and finishing strains between the uniaxial and hydrostatic loading cases from the modeling results. In every case, the starting strains are later and the finishing strains are earlier in the uniaxial cases as compared to the hydrostatic cases. This is likely a result of the c-axis gap, or forbidden zone, observed in the compression of the unit cells from DFT.

Comparing the models to each other, there are some parallels. For a given compound, the start and stop critical strains are similar. This trend is true for both compounds and both hydrostatic and uniaxial loadings. Even though the effective elastic moduli of the materials differed between hydrostatic and uniaxial loadings, the strains were consistent. In $CaFe_2As_2$ due to the phase change, there is more variability in the start and stop strains. However, these strains are still similar. This again indicates that the applied c-axis strain is the critical parameter in predicting the response of these materials. In fact, the c-axis strain is clearly evident in the $LaRu_2P_2$ results and can easily be

linked back to the compression of a single unit cell. Contrary to this, however, is the fact that it is difficult to unambiguously relate the c-strain at collapse observed in the DFT simulations to the starting and finishing strains of the thermodynamic composite model. This is because while c-axis collapse controls the phase transition and results in the energy landscape, it is the energetics of the systems that ultimately control the nature of the continuous phase transition, a clear conclusion one can make from this modeling effort.

The agreement of these models clearly shows the utility of this approach, despite the idealized crystals simulated by DFT. Evidence has been found for the propensity of these materials to form both point defects [46, 51] and twins [116] which are certain to alter the macroscopic material behavior in ways not accounted for here. Additionally, there is likely some coupling between temperature, the magnetic moments and the cell geometry that has not been directly accounted for here. Furthermore, these materials have been observed to undergo micaceous deformation at high strains [18] inducing some levels of plasticity. For these reason, it is not expected that the models perfectly predict the response of a real sample but through this analysis, their utility has been demonstrated. Finally, it is worth noting that these results clearly point to the fact that similar models can be developed by fitting directly to experimental data to obtain thermodynamic information of the constituent phases at room temperature, which will be quite beneficial for understanding these materials.

3.6.6 Effects of Temperature

So far, modeling the phase change and pseudo-elasticity of $ThCr_2Si_2$-type crystals has only been performed at 0 K. Relaxing crystals and finding their ground states only characterizes their low-temperature response and cannot predict the effects of finite temperature on the mechanical response. Since we know these crystals, particularly $CaFe_2As_2$, are subject to the effects of temperature ($CaFe_2As_2$ undergoes a phase transition above its Néel temperature of 170 K), the mechanical properties must be influenced by temperature. The mechanical responses of all materials are func-

tions of temperature. Furthermore, the compression of $CaFe_2As_2$ and $LaRu_2P_2$ performed for our comparison was performed at room temperature.

The Quasi-Harmonic Approximation

There are a limited number of methods for simulating the mechanical properties at temperature. Since there are no existing interatomic potentials for these materials, running classical molecular dynamics (MD) is not an option. Since *ab initio* molecular dynamics (AIMD) is extremely computationally costly, and the simulation cell size would require extremely long run times to reach thermodynamic averages of statistical accuracy (based on the ergodic principle), running thermodynamic integration (TI) to compute the free energy is not feasible.

Alternatively, these free energies can be calculated via the quasi-harmonic approximation (QHA). Through the QHA, we can calculate the free energies for each phase and see how they change over temperature. The pseudo-elastic composite model can be applied to the free energies calculated by the QHA. As with the 0 K pseudo-elastic models, the appropriate free energy is minimized based on the loading conditions. Minimization of the Helmholtz free energy (F) represents displacement control compression, while minimization of the Gibbs free energy (G) represents load control compression.

Model Results and Discussion

The QHA was run for $CaFe_2As_2$ under hydrostatic compression. Dynamical matrices of both phases, the orthorhombic (OR) and collapsed-tetragonal (cT), were computed for states in both tension and compression. The Helmholtz and Gibbs free energies were then computed for both phases as a function of temperature and pressure. In the same fashion as the zero-temperature pseudo-elastic models, the phase fraction is determined by minimizing the appropriate thermodynamic potential, calculated at finite temperature. A displacement-control model is achieved by minimizing the Helmholtz free energy, while a load-control model is constructed by minimizing the Gibbs free energy.

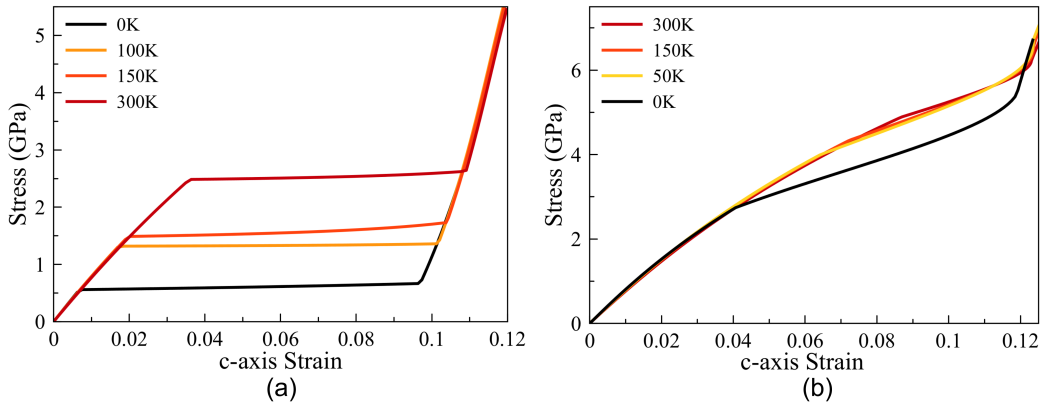

Figure 27: The responses of $CaFe_2As_2$ under hydrostatic compression at different finite temperatures. (a) The transition strains, and stress increase with increasing temperature for displacement-control simulation. (b) The transition stress and strains also increase with temperature for the load-control simulations.

Temperature-dependent models were constructed for temperatures of 50 K, 100 K, 150 K, and 300 K. The results of the models can be seen in Figure 27. For both control scenarios, the stiffness of both phases decreases with increasing temperature, which is consistent with most materials. The transition strains for both scenarios increase with temperature, both the onset transition strain (ε_1) and the offset transition strain (ε_2). In displacement control, the phase transition stress increases with temperature. In load control, the transition does occur at higher stresses with increasing temperature. However, the effective stiffness in the transition region decreases with increasing temperature.

Chapter 4

Defects in $ThCr_2Si_2$-type Crystals

Considering that the electronic properties of $ThCr_2Si_2$-type crystals are very sensitive to the presence of point defects, it is reasonable to suspect that defects may also alter the mechanical responses of these crystals. The responses of pure $ThCr_2Si_2$-type crystals are useful in their own rights. However, tunability in a material is highly coveted, and being able to expand the range of their mechanical responses could open up many doors to potential applications. In this chapter, we explore how point defects within materials with these crystal structures can affect their mechanical behavior in compression.

Recall from Chapter 3, the hydrostatic compression of a pure sample of $LaRu_2P_2$ induced an “S"-shaped pseudo-elastic stress-strain response. This was shown in experimental investigations [19], as well as DFT compression simulations (presented in Section 3.2). Although uniaxial compression experiments of pure $LaRu_2P_2$ have yet to be performed, the stress-strain response predicted by DFT exhibits similar pseudo-elasticity to hydrostatic simulations. These stress-strain responses are also similar to that observed in both hydrostatic and uniaxial compression investigations of $CaFe_2As_2$. In an effort to experimentally study uniaxial loading of $LaRu_2P_2$, a defected sample was inadvertently tested. In the following sections, we investigate how these defects influenced the mechanical response of the defected sample.

4.1 Investigations of Defected $LaRu_2P_2$

With $LaRu_2P_2$ as a case study, we aim to characterize the role point defects have on the mechanical response of $ThCr_2Si_2$-type crystals. Along with experimental collaborators at Ames Laboratory in Iowa, who fabricated the crystals, and at the University of Connecticut, who performed the compression tests and chemical analysis, we investigate point defects in $LaRu_2P_2$. To the authors’ knowledge, there have been no studies of point defects in $LaRu_2P_2$ at the time of this investigation and so we pose the following questions. What types of point defects might be expected to be

found in $LaRu_2P_2$? How likely are they to form? How do defects effect the mechanical response of $LaRu_2P_2$?

4.1.1 Fabrication of Defected $LaRu_2P_2$ and Experimental Micropillar Compression

Single crystals of $LaRu_2P_2$ were grown by our collaborators at Ames Laboratory in tin flux [19] producing bulk single-crystal samples of $400\,\mu m \times 300\,\mu m \times 100\,\mu m$ (Figure 28(a)). The chemical composition of the surface of the samples was investigated by our collaborators at the University of Connecticut using Energy Dispersive X-ray Spectroscopy (EDX) both in a scanning electron microscope (SEM) (Teneo LoVac, FEI, OR, USA) and a transmission electron microscope (TEM) (Talos, FEI, OR, USA). The chemical composition of La, Ru and P on the surface was probed at several randomly chosen locations (Table 6). Location 1 was the site of the micropillar, Location 2 was the site of the TEM specimen in Figure 28(b), and Locations 3-6 were chosen randomly on the surface of the crystal. Location 7 was $3\,\mu m$ below Location 6. We also obtained the depth profile of composition under Location 2 from the cross-sectioned TEM specimen (Figure 28(b) and 28(c)). The test sensitivity threshold of EDX data is approximately $\pm 5\%$ [117] and all of the composition data here is normalized by the composition of La. In general, the composition on or near the surface varied with position on the crystal and was typically either Ru or P deficient or deficient in both. Alternatively, the compounds could be La rich as the analysis can only determine the chemical composition, not the nature of the defected crystal. The concentrations of other elements were negligibly small, so our crystal consisted only of La, Ru and P. The discrepancy in the observed compositions at different locations highlights the presence of variations in local composition.

At Location 2, selected area diffraction was performed to investigate the lattice parameters of the crystal at this concentration. At the surface, the diffraction data shows that the crystal has lattice parameters of $a = 3.80$ Å, and $c = 10.12$ Å. The reported experimental lattice parameters are $a = 4.03$ Å, and $c = 10.68$ Å [19]. The c-axis of the non-stoichiometric sample in this work is significantly shorter than that observed in a pure sample of $LaRu_2P_2$.

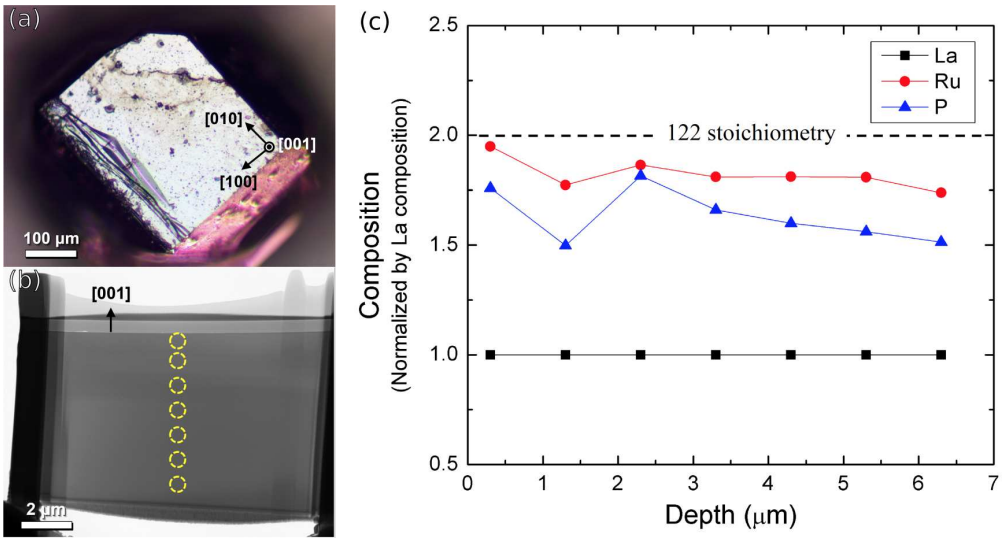

Figure 28: Solution-grown $LaRu_2P_2$ single crystal. (a) Optical micrograph of crystal, (b) Bright-field TEM image, (c) the depth profile of composition under Location 2 (Table 6) at the circled regions in (b).

Microcompression tests of this sample were performed by our collaborators at the University of Connecticut. Micropillars were milled out of the samples using a Focused Ion Beam (FIB) (HeliosNanolab 460F1, FEI, OR, USA) at Location 1 (La:Ru:P = 1:1.70:1.92) in Table 6 with currents ranging from 7.7-300 pA at 30 kV. The final milling was done with low current beam (7.7 pA) to minimize the ion beam damage on the surface. The ratio of height to diameter of micropillars is about 4 and the taper angle was approximately 2°, which is small enough to ensure that the taper effect on the stress distribution is not significant. The loading axis of the micropillars was oriented in the $[001]$ direction of the crystal (Figure 29(a)). The micropillars milled from the bulk crystals were compressed uniaxially with a nano-indenter (NanoFlipTM, Nanomechanics, TN, USA). The head of the nano-indenter was flat to provide a surface more conducive to pillar compression. The displacement rate was 10 nm/s, which corresponds to the strain rate of approximately 5×10^{-3}/s. Stress-strain data was calculated accurately with the Sneddon correction to remove the contribution of deformation at the micropillar base [118].

The stress-strain response of the defected $LaRu_2P_2$ micropillar at location 1 is nearly linear, as shown in Figure 29(b). There is a slight softening in the response at around 2.6% strain followed by a subsequent hardening around 5.7% strain. Also, the decrease in contact stiffness data in

Table 6: Chemical composition ratio at various positions. Location 1 was the micropillar; Location 2 is the surface of the depth profile in Figure 28. Locations 3-6 were randomly chosen on the surface of the sample, while Location 7 was $3\,\mu\mathrm{m}$ below Location 6. Note that the composition is normalized by the composition of La.

Position on Surface	Chemical Composition Ratio		
	La	Ru	P
Location 1 (Pillar)	1	1.70	1.92
Location 2 (TEM)	1	1.94	1.76
Location 3	1	1.40	1.76
Location 4	1	1.36	1.75
Location 5	1	1.60	2.18
Location 6	1	1.64	2.22
Location 7 ($3\,\mu\mathrm{m}$ Below Location 6)	1	1.76	1.92

the middle of deformation shows that some form of structural collapse does occur. Normally, a material which does not undergo either phase transition or structural collapse, exhibits a continuous increase in contact stiffness under uniaxial compression [119]. However, the inflections in stress-strain curve are nearly imperceptible compared to the pseudo-elastic response previously observed in the hydrostatic compression of $LaRu_2P_2$ [12, 19] and the uniaxial compression of a similar compound, $CaFe_2As_2$ [18]. It is worth noting that the hydrostatic response of $LaRu_2P_2$ reported by Drachuck et al. [19] is from a sample that was made by the same fabrication methods, with the same raw materials, as our sample. The surface of our crystal has shortened lattice parameters and deviations from stoichiometry, while the bulk lattice parameters of the crystal studied in [19] are in line with those of pure $LaRu_2P_2$.

In order to ensure that this response is representative, three additional pillars at various locations on the sample's surface were also compressed. The stress-strain curves are similar (Figure 30); however, the amounts and locations of softening do differ, presumably on account of the varying chemical composition.

The deviations from stoichiometry are not negligible. At certain locations, the composition data indicates that the sample is deficient in either ruthenium or phosphorus with deficiencies as high as 25%. Most sites that were tested were at least 12.5% deficient in either phosphorus or

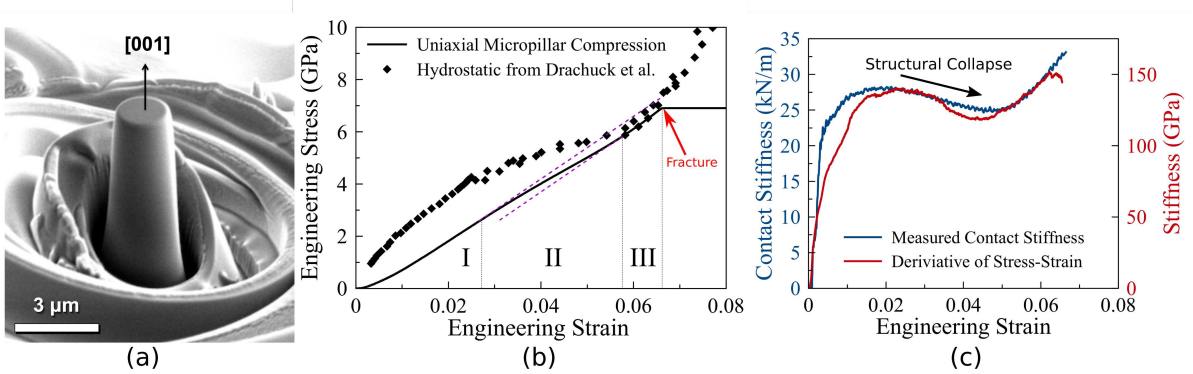

Figure 29: The uniaxial compression tests of defected $LaRu_2P_2$ micropillars. (a) SEM micrograph of one micropillar, (b) the engineering stress-strain curve from this micropillar compression test and hydrostatic compression data from Drachuck et al. [19]. (c) The contact stiffness (blue) and the tangent modulus computed from the stress-strain data (red) versus strain. Note that the decrease in contact stiffness implies the structural collapse during uniaxial compression, which matches the trends observed in the tangent modulus.

ruthenium. This deviation in stoichiometry would be manifested in the form of point defects, which at such concentrations, would undoubtedly affect the mechanical response of the crystal. In order to explain these effects, and the experimental observations, point defects in $LaRu_2P_2$ were investigated with DFT.

4.1.2 Computational Investigations of Isolated Defects

Since it has been demonstrated, through experiments on $CaFe_2As_2$ and modeling of both $CaFe_2As_2$ and $LaRu_2P_2$ [120], that hydrostatic and uniaxial compression give rise to similar behavior, the lack of a significant softening region in $LaRu_2P_2$ appears to be a consequence of composition. Therefore, we sought to investigate the nature of isolated point defects in this compound using DFT calculations.

To examine the nature of point defects in these materials using DFT, we use a hierarchy of supercells that are based on both the primitive unit cell, Figure 32(a), and the conventional tetragonal unit cell, Figure 1. The primitive unit cell of $LaRu_2P_2$ is triclinic and contains only five atoms (Figure 32(a)) [121] and is particularly is useful in understanding the crystal's symmetry and creating our special quasirandom structures (SQSs) discussed in Section 4.1.3.

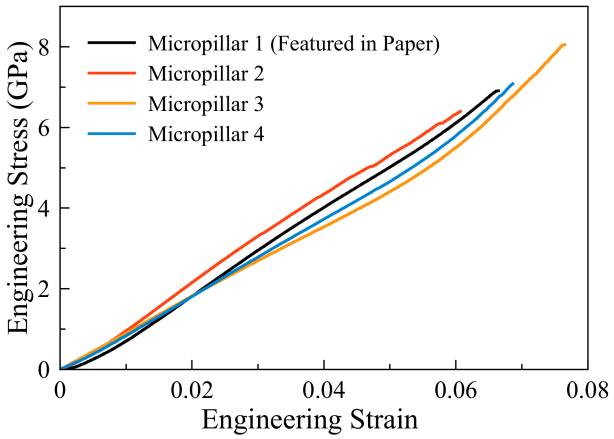

Figure 30: The four micropillar compression tests performed on various locations across the surface of the sample. All micropillars exhibited less softening than predicted by DFT simulations. The computational investigations of defected $LaRu_2P_2$ are compared to the compression results of micropillar #1.

In order to understand the nature of point defects in $LaRu_2P_2$, we first examine the formation energies of isolated defects. To this end, large supercells of $LaRu_2P_2$ containing single point defects were constructed. These supercells were composed of 8 ($2\times2\times2$) supercells of 20 atoms for a total of 160 atoms (without the defect). A supercell with one interstitial contained 161 atoms, while one with a vacancy contained 159 atoms. This size supercell was chosen since the defect energies did not vary more than 0.05 eV between subsequent doubling of the supercell. Supercells containing a single isolated vacancy or interstitial of each element were constructed and relaxed to an energy tolerance of 10^{-5} eV using the conjugate gradient method. Since there is only one lanthanum atom in the primitive unit cell, it is immediately obvious that all lanthanum sites are equivalent. It can also be shown that both ruthenium positions are symmetrically equivalent, as well as that both phosphorus positions are symmetrically equivalent. While all vacancy positions are symmetrically equivalent, there are, however, two different possible locations for interstitials (Figure 32(b)). The first is a space at the center of the base of the conventional unit cell, which is an octahedral space surrounded by four lanthanum atoms and two phosphorus atoms. The other is a pocket of space within the cage between the phosphorus and lanthanum atoms. Both interstitial sites were investigated for all chemical species (La, Ru, P). For ruthenium and phosphorus, the

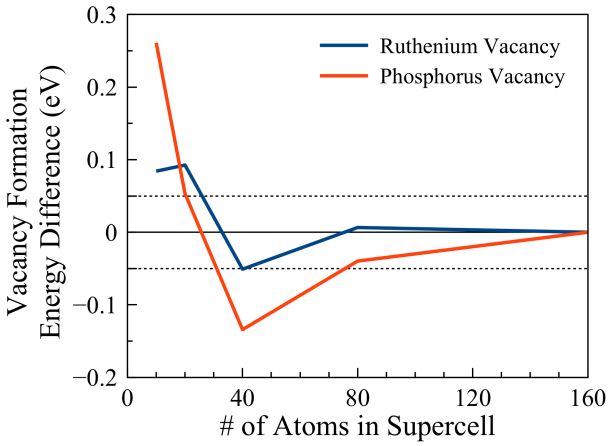

Figure 31: The difference in vacancy formation energy, calculated with supercells of varying sizes, compared to the vacancy formation energy calculated with a 160-atom supercell. By 80 atoms, the calculated energy varies by less than 0.5 eV, showing sufficient convergence by 160 atoms.

octahedral site was considerably more energetically favorable than the cage interstitial site, by about 1.4 eV and 1.8 eV (per defect), respectively. However, for lanthanum interstitials, we found that the cage site was more energetically favorable than the octahedral site by about 1.7 eV per defect.

In order to calculate the vacancy formation energies, the appropriate chemical potentials (μ_i) of each element are required. The work of Mishra et al. [122] outlines a method to approximate the chemical potentials of the different chemical species in these compounds. By relating the cohesive energies of a given compound to the compounds near it on the composition phase diagram, estimates of the elemental chemical potentials can be calculated. For this reason, we compiled a ternary phase diagram of the lanthanum–ruthenium–phosphorus system (Figure 33).

A survey of the known phases and hypothetical phases in this system was conducted to construct the phase diagram. The phases which were sampled are outlined in Table 7. In addition to compounds previously reported to exist in the La–Ru–P system and listed on the crystallography open database (COD) [123–127], compounds found in the analogous Ca–Fe–As system were investigated [128, 129], as well as compounds suggested by the AFLOWLIB database [130] and structures generated with the evolutionary algorithm USPEX [72, 73, 131–134]. USPEX was em-

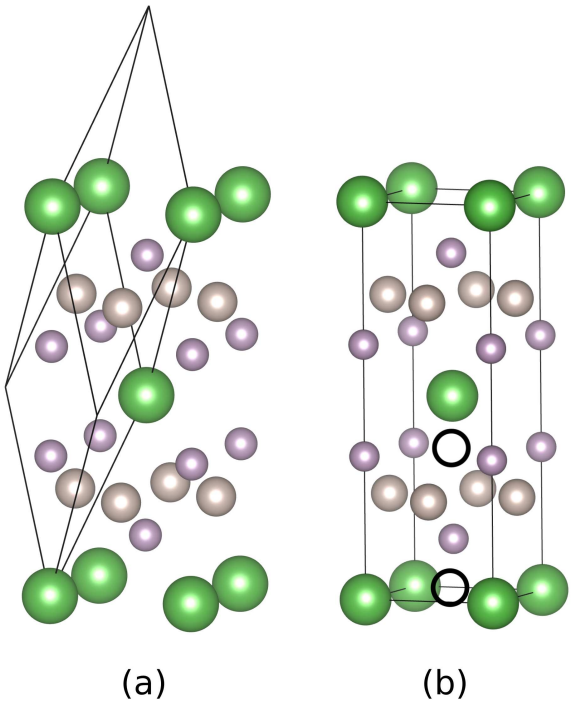

Figure 32: The (a) $LaRu_2P_2$ primitive unit cell is triclinic and contains only 5 atoms, (b) while the conventional body-centered tetragonal unit cell contains 10 atoms. The black circles represent the two possible interstitial locations: the “cage" location (higher) and the octahedral location (lower).

ployed to find the lowest-energy structure for compositions of: $La_2Ru_3P_4$, $La_2Ru_4P_3$, and $LaRu_2P$ to make sure we did not miss structures close to the $LaRu_2P_2$ compound that would have the most impact on our results. The investigations of the $La_2Ru_3P_4$ and $La_2Ru_4P_3$ compositions were seeded with the $LaRu_{1.5}P_2$ and $LaRu_2P_{1.5}$ vacancy structures described in Section 4.1.3, while the investigation of the $LaRu_2P$ composition was seeded with conventional unit cells with two phosphorus atoms removed. All three combinations of two phosphorus vacancies within a conventional unit cell were provided as seeds. For all stoichiometries investigated with USPEX, the algorithm failed to find a structure with lower energy than one which was provided as an initial seed.

To further round out this survey, two crystal structures, $CaFeAs_2$, and $CaFe_4As_3$, were taken from the analogous Ca–Fe–As system [128, 129]. The structure of $CaFeAs_2$ is monoclinic and can be related to the structure of $CaFe_2As_2$ by the removal of two iron atoms, causing layer pattern of: Ca, Fe_2As_2, Ca, As_2 [135]. $CaFe_4As_3$ forms an orthorhombic unit cell with space group symmetry

Pnma which is not related to the structure of $CaFe_2As_2$ [136]. More in-depth information on the investigated phases can be found in Appendix A.

Our analysis of the cohesive energies revealed that 14 phases lie on the convex hull. They are: gray phosphorus, dhcp lanthanum, hcp ruthenium, LaP, LaP_5, La_3Ru, La_5Ru_2, Ru_2P, RuP, RuP_2, RuP_3, RuP_4, $LaRu_4P_{12}$, and $LaRu_2P_2$. The Materials Project [137–139] provides a phase diagram of the La–Ru–P system with additional phases on their convex hull which we did not find to be on our convex hull. They are: $LaRu_2$, LaP_2, and LaP_7. Furthermore, we predict La_3Ru and La_5Ru_2 to appear on the convex hull, while phase diagram provided by the Materials Project does not. We predict phosphorus in the gray arsenic structure to be the lowest-energy allotrope of phosphorus, which is expected to be predicted by LDA [140], while the Materials Project predicts red phosphorus, which is consistent with the use of GGA/PBE. We calculated the difference between red phosphorus and gray phosphorus to be only 0.06 eV/atom and this discrepancy is not expected to affect the calculated defect energies. These discrepancies may be due to the differences in the calculations, including which exchange-correlation functional was employed.

With this phase diagram, we were able to calculate the isolated defect formation energies. The energy of a supercell, which was constructed of 32 formula units, with a defect (E_{SC}) is equal to the energy of 32 non-defected formula units (E_{122}), plus the defect formation energy (Δe_i^{def}), and the change in chemical potential due to the defect atom ($N_i\mu_i$), where $N_i = +1$ for an interstitial and $N_i = -1$ for a vacancy.

$$E_{\text{SC}} = 32E_{122} + \Delta e_i^{\text{def}} + N_i\mu_i \tag{4.1}$$

The effective chemical potential is calculated in reference to the compounds which surround it on the convex hull by assuming that the cohesive energy is equally distributed between all atoms [122]. Keep in mind that while the $LaRu_2P_2$ can be interpreted as having ionicity, it is indeed a conductor and therefore electrostatic potential effects do not need to be considered in point defect calculations. It is also important to note that the choice of chemical potential depends on the type (vacancy or interstitial) and chemistry of the defect. To make the calculation and use of the chemical potential concrete, we highlight its concept in the case of a phosphorous interstitial in $LaRu_2P_2$. The

Table 7: List of compounds tested to investigate the lanthanum–ruthenium–phosphorus system.

Compound	Structure	Space Group	E_{coh}/atom (eV)	ref
La	dhcp	*P6$_3$/mmc*	-5.17	[141]
Ru	hcp	*P6$_3$/mmc*	-8.78	[142]
P	gray phosphorus	*R$\bar{3}$m*	-4.45	[140]
$LaRu_2$	C15	*Fd-3m:1*	-7.65	[143]
La_5Ru_2	–	*C2/c*	-6.43	‡
La_3Ru	–	*Pnma*	-6.28	‡
LaP	–	*Fm3m*	-6.34	[144]
LaP_2	–	*C1c1*	-5.64	[145]
LaP_5	–	*P1 21/m1*	-5.15	[146]
LaP_7	–	*P2$_1$/c*	-4.80	‡
Ru_2P	–	*Pbnm*	-7.77	[141]
RuP	–	*Pnma*	-7.24	[147]
RuP_2	–	*Pnnm*	-6.59	[148]
RuP_3	–	*P$\bar{1}$*	-6.11	‡
RuP_4	–	*P$\bar{1}$*	-5.82	[149]
$LaRu_2P_2$	$ThCr_2Si_2$	*I4/mmm*	-7.40	[150]
$LaRu_4P_{12}$	–	*Im-3*	-6.27	[151]
$LaRuP_2$	–	*P2$_1$*	-6.75	[128]†
$LaRu_4P_3$	–	*Pnma*	-7.47	[129]†
$LaRu_2P$	–	*P 4/n 21/m 2/m*	-7.25	‡*
$LaRu_{1.5}P_2$	–	*P4m2*	-7.09	‡*
$LaRu_2P_{1.5}$	–	*P4mm*	-7.35	‡*
$La_{0.5}Ru_2P_2$	–	*P 4/m 2/m 2/m*	-7.23	‡
$La_{0.75}Ru_2P_2$	–	*P 4/m 2/m 2/m*	-7.32	‡

† Structures observed to form in the Ca–Fe–As ternary system;
‡ Structures which have not been previously reported, further information can be found in the supplemental attachment;
* Stoichiometries investigated with the USPEX evolutionary algorithm.

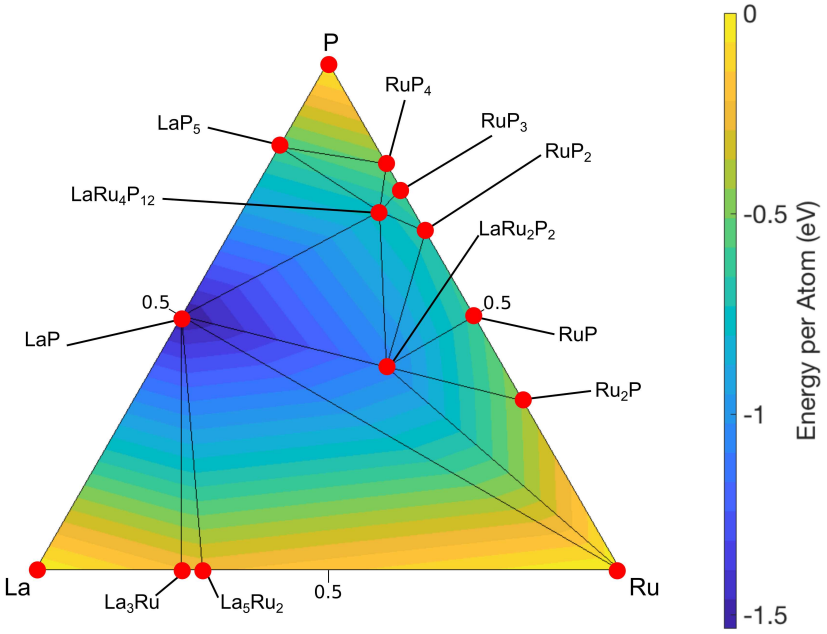

Figure 33: The lanthanum-ruthenium-phosphorus 0 K ternary phase diagram reveals that $LaRu_2P_2$ and $LaRu_4P_{12}$ are the only ternary compounds to exist on the convex hull. The red dots indicate compounds which were determined to be stable.

chemical potentials, μ_{La}, μ_{Ru} and μ_P can be found using the computed cohesive energies of LaP, $LaRu_2P_2$, and $LaRu_4P_{12}$ by solving the following simultaneous equations:

$$\begin{aligned} E_{LaP} &= \mu_{La} + \mu_P \\ E_{LaRu_2P_2} &= \mu_{La} + 2\mu_{Ru} + 2\mu_P \\ E_{LaRu_4P_{12}} &= \mu_{La} + 4\mu_{Ru} + 12\mu_P \end{aligned}$$

The extraction of the chemical potentials from these equations can then be used to compute the vacancy formation energy of P in $LaRu_2P_2$. Naturally, the chemical potentials may need to be re-evaluated for each point defect depending on the structure of the phase diagram.

Using this method, the vacancy formation energies were calculated to be 1.06 eV for lanthanum, 0.773 eV for ruthenium, and 1.59 eV for phosphorus, while the interstitial formation energies were calculated to be 5.87 eV for lanthanum, 2.48 eV for ruthenium, and 2.03 eV for phosphorus. All defect formation energies are tabulated in Table 10. Overall, the values of forma-

tion energies for interstitials are high, which is to be expected. Based on these formation energies, it is far more likely to form vacancies than interstitials in $LaRu_2P_2$. This suggests the deviations in the stoichiometry observed are far more likely to be the result of ruthenium and phosphorus vacancies rather than lanthanum interstitials.

Table 8: The calculated isolated defect energies of $LaRu_2P_2$ and the necessary reference structures used to calculate the defect energies.

		Lanthanum	Ruthenium	Phosphorus
Vacancies	Energy	1.06 eV	0.773 eV	1.59 eV
	Reference Structures	$LaRu_2P_2$, RuP	$LaRu_4P_{12}$, $LaRu_2P_2$, LaP	LaP, Ru, $LaRu_2P_2$
Interstitials	Cage Energy	5.87 eV	3.90 eV	3.83 eV
	Octahedral Energy	7.60 eV	2.48 eV	2.03 eV
	Reference Structures	LaP, Ru, $LaRu_2P_2$	$LaRu_2P_2$, Ru	$LaRu_4P_{12}$, $LaRu_2P_2$, LaP

From these defect energies, we can calculate the equilibrium concentration of defects at a given temperature [152] by:

$$\chi_v = \exp\left(\frac{S_v}{k_B}\right)\exp\left(\frac{-\Delta h}{k_B T}\right) \tag{4.2}$$

where χ_v is the equilibrium vacancy concentration, S_v is the vacancy formation entropy, Δh is the defect formation enthalpy, and k_B is the Boltzmann constant. Approximating that the entropy exponential term is on the order of unity, we calculated the equilibrium concentration of ruthenium and phosphorus vacancies at room temperature (300 K), and the pre-quench processing temperature (1053 K) [19]. The expected ruthenium and phosphorus equilibrium concentrations at room temperature are 1.03×10^{-13} and 1.94×10^{-27}, respectively. At the processing temperature, the expected equilibrium concentrations are 2.00×10^{-4} and 2.45×10^{-8}, respectively. Even if the entropy contribution is > 1, these equilibrium vacancy concentrations are many orders of magnitude smaller than that observed in our experiments. Thus, the observed composition is not due to the thermodynamic stabilization of vacancies, and is most likely due to processing.

4.1.3 Computational Investigations of Defects at High Concentrations

While the energetics of isolated defects provides insight into what defects are likely to form, the deviations in stoichiometry observed experimentally result in defects populations that are far from isolated. Additionally, the mechanical response of the micropillar deviates from the expected pseudo-elastic response significantly when compared to both experimental and modeling hydrostatic responses [12, 19] and modeling uniaxial response [120]. This deviation is likely a result of these concentrated or interacting defects. In this vein, we examine the crystal structure and mechanical properties of $LaRu_2P_2$ subjected to high concentrations of defects. We will achieve this by constructing small cells with vacancies or interstitials. However, our focus is refined to lanthanum interstitials, ruthenium vacancies, and phosphorus vacancies, since they would contribute to the experimentally observed compositions. It is important to be mindful that defects at high concentrations may result in crystals with mechanical instabilities, so this possibility must be considered.

Lanthanum Interstitials

First, we investigate lanthanum interstitials, remembering that the isolated lanthanum interstitial energy was very high (5.91 eV) which suggests their formation is likely unfavorable. Our initial investigation in lanthanum interstitials at high concentrations focuses on the standard tetragonal unit cell, Figure 1. The interstitial lanthanum atom could be in either the cage or octahedral location (Figure 32(b)) and unit cells for both locations were constructed. With the interstitial, each unit cell contained three lanthanum atoms, four ruthenium atoms, and four phosphorus atoms. The interstitial cells were relaxed and the resulting structures for the octahedral and cage interstitial locations are shown in Figure 35(a) and Figure 35(b), respectively. Elastic constants were then computed for both structures and it was found that C_{55} was negative for both interstitial cells, and thus both are mechanically unstable. The full elastic constants are tabulated in Table 9. Due to their high energetic cost and mechanical instability, the presence of a high concentration of lanthanum interstitials is unlikely and we do not consider them any further.

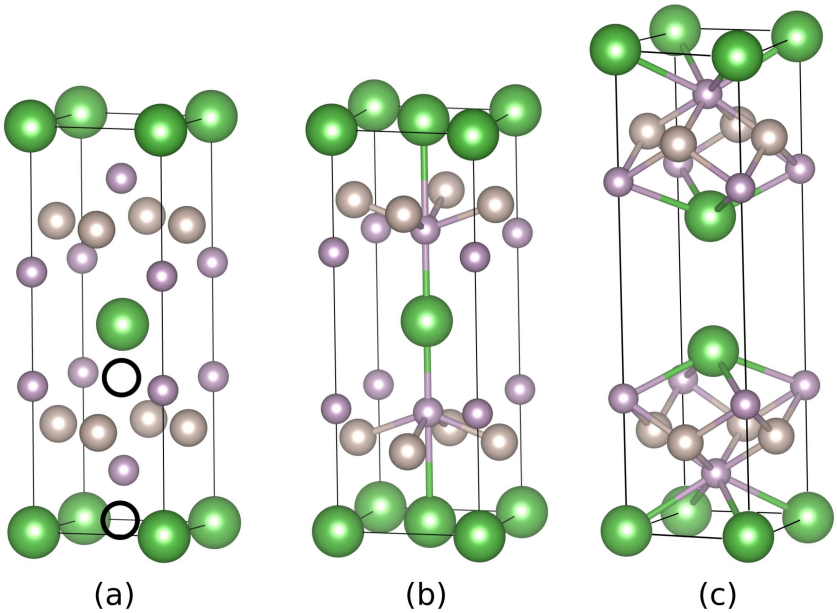

Figure 34: A lanthanum interstitial might exist at one of two possible locations within the unit cell (a), either in the lanthanum layer or stacked between the lanthanum layer and the Ru–P layer. The in-plane interstitial disrupts the cage by causing all the phosphorus atoms to be on the same side of the ruthenium layer (b). The stacked interstitial causes separation in the crystal between the interstitial and the La atom at the center of the unit cell.

Ruthenium or Phosphorus Vacancies

Conversely, we investigate ruthenium and phosphorus vacancies for their potential to contribute to the observed composition. Unit cells with a ruthenium vacancy or a phosphorus vacancy were constructed by removing a single atom from the unit cells. Since all ruthenium positions are equivalent, and all phosphorus positions are equivalent, removing any one ruthenium or phosphorus atom was adequate when creating the cell. Removing a ruthenium or phosphorus atom from the standard unit cell created a 1/4 ruthenium vacancy concentration (Figure 35(c)) or a 1/4 phosphorus vacancy concentration structure (Figure 35(d)), respectively. Likewise, removing one atom from a double cell created 1/8 vacancy concentration structures.

The 1/4 vacancy concentration structures, $LaRu_{1.5}P_2$ and $LaRu_2P_{1.5}$, were relaxed to determine lattice constants and crystal structure, and elastic constants were calculated to assess mechanical stability. The lattice constants of $LaRu_{1.5}P_2$ are $a = 4.05$ Å and $c = 9.50$ Å and the lattice constants

Table 9: Elastic constants (in GPa) of modeled possible defected structures.

Structure	La int 1	La int 2	$LaRuP_2$	Ru vac	P vac
C_{11}	260	192	195	278	185
C_{22}	–	–	177	–	–
C_{33}	148	133	151	155	122
C_{12}	102	52.1	57.4	123	143
C_{13}	65.3	-7.47	73.3	94.1	76.4
C_{23}	–	–	68.4	–	–
C_{44}	118	128	86.3	113	104
C_{55}	-69.6	-15.9	57.0	82.1	33.9
C_{66}	–	–	63.6	–	–

of $LaRu_2P_{1.5}$ are $a = 4.01$ Å and $c = 9.84$ Å. It is noteworthy that the a-axis lengths are very close to that of pure $LaRu_2P_2$ ($a = 3.99$ Å and $c = 10.52$ Å), while the c-axis lengths are significantly shorter. The elastic constant tensors are positive definite, and thus these crystals are mechanically stable (Table 9). The double-cell vacancy structures, $LaRu_{1.75}P_2$ and $LaRu_2P_{1.75}$, were also relaxed and had lattice constants of $a = 4.02$ Å, $c = 9.93$ Å, and $a = 4.02$ Å, $c = 10.06$ Å, respectively. These lattice constants demonstrate a similar reduction of the c-axis lengths. Elastic constants of these structures were not computed, since we already found higher vacancy concentrations to be mechanically stable, and thus high vacancy concentrations can indeed exist.

$LaRuP_2$

Another potential ruthenium deficient structure is the $LaRuP_2$ structure (shown in Figure 35(e)). This structure is known to exist in the analogous calcium−iron−arsenic system [135], but it has not yet been reported in the lanthanum–ruthenium–phosphorus system. A unit cell of $LaRuP_2$ has 2 fewer ruthenium atoms than $LaRu_2P_2$, both of which can be thought of as absent from the same cage. The elastic constants of calculated for this structure show it to be mechanically stable.

4.1.4 Simulation of Compression of Defected Structures

Since large concentrations of defects are present in the sample, we aim to explain the experimentally observed stress-strain response though the mechanical response of high-concentration

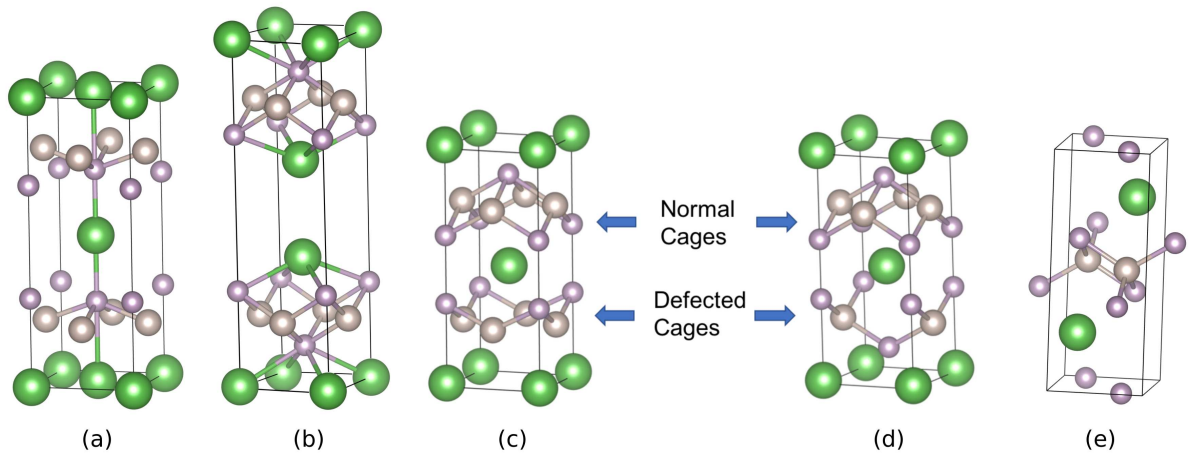

Figure 35: The structures of both lanthanum interstitials: (a) the octahedral site, and (b) the cage site after structural relaxation. Both of these unit cells are mechanically unstable. The structures of the standard tetragonal unit cells with (c) a single phosphorus vacancy, and (d) a single ruthenium vacancy. Both the ruthenium and phosphorus vacancies disrupt the Ru–P cage structure but are mechanically stable. (e) the 1:1:2-compound analogous to the Ca-Fe-As system.

defected structures introduced in the previous section. In order to understand how these vacancies affect the mechanical properties of $LaRu_2P_2$, we simulated the uniaxial compression the defected cells. In pure $LaRu_2P_2$, the softening in the pseudo-elastic response is associated with a large reduction (approximately 5%) of the c-axis length. However, the unstressed defected structures already have c-axis lengths at least that much shorter than pure $LaRu_2P_2$. The uniaxial compression of the $LaRu_{1.5}P_2$ and $LaRu_2P_{1.5}$ unit cells did not show any softening, in contrast to the response of pure $LaRu_2P_2$ which demonstrates a softening behavior (Figure 36). Similarly, hydrostatic compression of these defected cells also failed to show a softening in the mechanical response.

However, the $LaRu_{1.5}P_2$ and $LaRu_2P_{1.5}$ structures do not properly represent the composition observed in experiments, which was closer to 12.5% vacancy concentration. For this reason, the $LaRu_{1.75}P_2$ and $LaRu_2P_{1.75}$ vacancy structures were compressed uniaxially. Perhaps these structures, closer in concentration to the experimental micropillar, would have mechanical responses which better resemble the experimental response. However, there was no softening observed in the compression of these crystals (Figure 36) either. This suggests that evenly dispersed vacancies cannot be the cause of the experimentally observed stress-strain response. Instead, there are likely

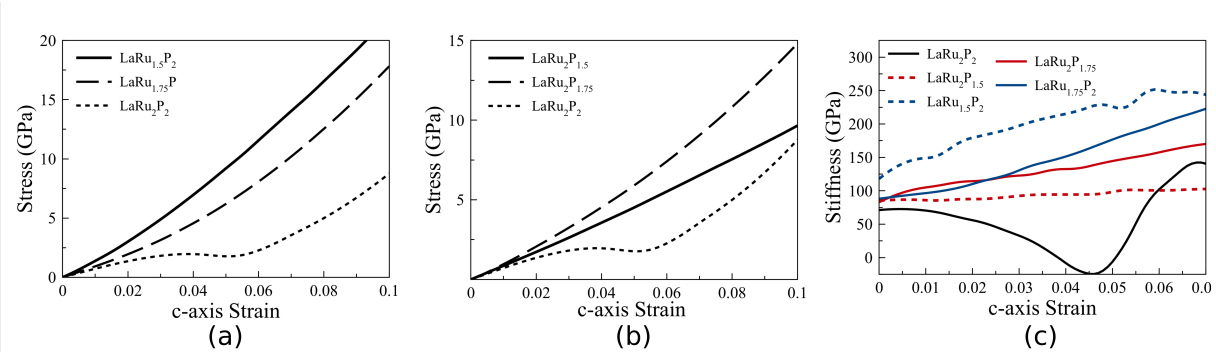

Figure 36: The stress-strain responses of (a) ruthenium vacancy structures and (b) phosphorus vacancy structures lack the softening regimes of pure $LaRu_2P_2$, which is highlighted by their stiffnesses (c).

regions of vacancy structures and regions of pure $LaRu_2P_2$. Furthermore, this demonstrates that vacancy concentrations of 1/4 and 1/8 are enough to cause the crystal to collapse under 0 applied stress. Naturally, this raises the question: what is the minimum vacancy concentration required to induce collapse?

Special Quasirandom Structures

To answer this question, and demonstrate the robustness of the previous results, we utilize special quasirandom structures (SQSs) to approximate the behavior of random point defects, specifically ruthenium and phosphorus vacancies, at various concentrations. SQSs are useful in representing substitutionally random structures by a relatively small, repeatable structure. In this case, phosphorus or ruthenium was “substituted" with vacancies. The SQSs were generated by the alloy theoretic advanced toolkit (ATAT) [76–89]. SQSs with phosphorus vacancy concentrations of 3.125%, 5%, 6.25%, 10%, 12.5%, 15%, and 25% were generated and SQSs with ruthenium vacancy concentrations of 5%, 6.25%, 10%, 12.5%, 15%, 20%, and 25% were generated. The method of generating SQSs took exorbitant amounts of time (several months) to generate SQSs for vacancy concentrations below 3.125% (for either element). Thus, SQSs for vacancy concentrations below 3.125% were not constructed for this study. Each SQS had only either ruthenium vacancies or phosphorus vacancies; structures containing both types of vacancies were not investigated.

The resulting SQSs have triclinic unit cells which are prohibitively difficult to compress uniaxially in VASP. For this reason, we resorted to compressing the cells hydrostatically as a representative investigation into the nature of collapse of the crystals, since the uniaxial and hydrostatic responses are similar. Furthermore, we monitored the c-axis lengths of the SQSs to provide insight into the collapsed, or uncollapsed state of the crystal at 0 stress.

The evolution of equilibrium c-axis lengths with vacancy concentration can be seen in Figure 37(c). From the c-axis lengths, we can see that all concentrations of phosphorus vacancies result in a collapsed crystal. The lowest P vacancy concentration, 3.125%, had a c-axis length of 10.1 Å, which is still significantly shorter than 10.52 Å of pure $LaRu_2P_2$. Ruthenium vacancy SQSs showed a more gradual lengthening in c-axis length with decreasing vacancy concentration. Compression tests revealed that no phosphorus vacancy SQSs exhibited softening (Figure 37(b)). However, ruthenium vacancy SQSs exhibited softening with concentrations of 6.25% and below (Figure 37(a)). The occurrence of collapse at low vacancy concentrations would suggest that the stability of the uncollapsed phase can be easily disrupted by electronic defects.

These SQS compression simulations confirm some of our observations from the $LaRu_{1.5}P_2$ and $LaRu_2P_{1.5}$, and $LaRu_{1.75}P_2$ and $LaRu_2P_{1.75}$ tetragonal vacancy structures created previously. Neither the SQSs nor the tetragonal vacancy simulation cells experienced softening for concentrations of 25% or 12.5%. This further backs our assertion that the response observed experimentally is due to the coexistence of defected and pure regions, or alternatively, gradients in the defect concentration. Presuming the response is a combination of the responses of two regions (defected and pure), we explore what this response might look like next.

4.2 Multi-Structure Composite Models

In Section 4.1.4, we showed that vacancy concentrations lower than those reported in experiments are required for softening. This suggests that perhaps the samples contain regions of high and low defect concentrations. To test if this hypothesis is reasonable, it is important to show that the combined response of the two regions resembles that observed in experiments. To this end, we

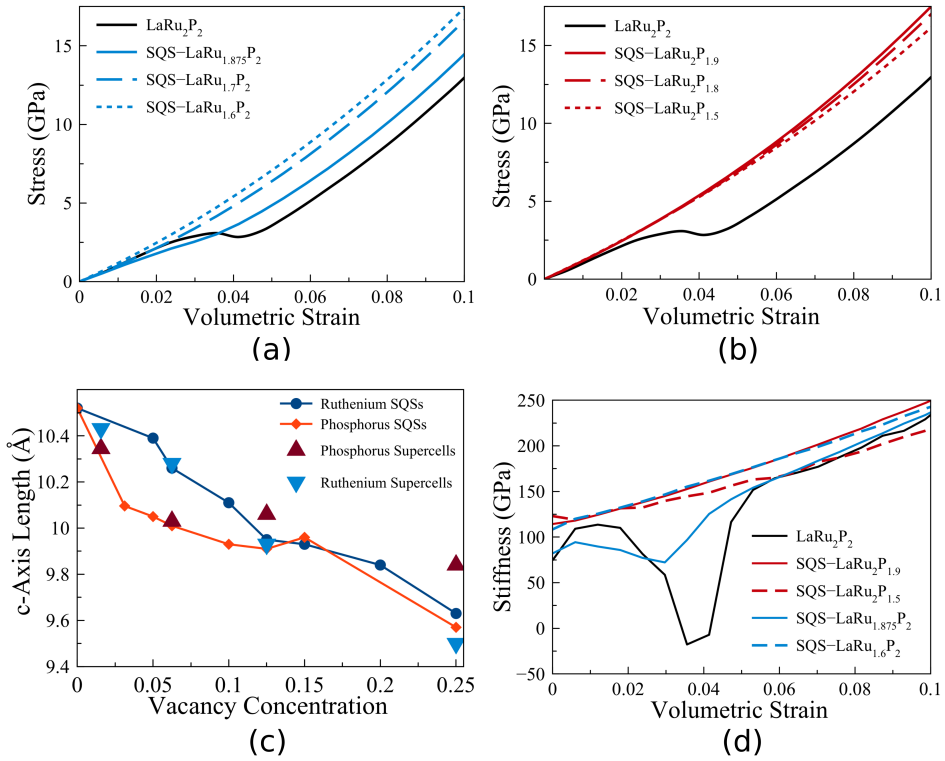

Figure 37: The hydrostatic compression of (a) SQSs with Ruthenium vacancies and (b) SQSs with P vacancies. For Ru concentrations of 20% and 15%, there is no observed softening of the volume-pressure curve while there is for 6.25%. However, the hydrostatic compression of SQSs with P vacancies for as small as 3.15% vacancies never shows softening. (c) A plot of the c-axis lengths of SQSs and defected supercells as a function of vacancy concentration for both Ru and P vacancies. (d) The stiffnesses of the SQSs as a function of strain. This confirms that the softening only occurs for Ru vacancy concentrations at or below 6.25%. Hydrostatic compression of pure $LaRu_2P_2$ is shown for comparison.

developed an iso-strain composite model, an iso-stress composite model, and an coherent inclusion model, where one region is a defected $LaRu_2P_2$ structure and the other region is stoichiometric $LaRu_2P_2$.

In order to understand how the various phase fractions might alter the mechanical properties, we examine the model for two cases: 12.5% phosphorus vacancies and 12.5% ruthenium vacancies. To arrive at these overall compositions, we use the stress-strain responses of the phases $LaRu_{1.5}P_2$ (one Ru vacancy per conventional unit cell) and $LaRu_2P_{1.5}$ (one P vacancy per conventional unit cell), in combination with pure $LaRu_2P_2$. The iso-stress and iso-strain composite models

of the stress-strain response can be found in Figure 36. The resulting composite stress-strain curves are shown in Figures 38(b) and 38(c), plotted against the pure phases and experimental data.

It is interesting to note that both the 12.5% ruthenium vacancy composite model and the $LaRu_{1.5}P_2$ stress-strain curves both represent compositions close to chemical analysis of the compound at the micropillar. The composition is not matched exactly by the composite model nor the ruthenium vacancy phase, since achieving that composition would require either a tri-phase model, or a phase that is both heavily Ru deficient and slightly P deficient. Additionally, the composition varied greatly across the sample, so it's unlikely that the composition is consistent throughout the micropillar. Furthermore, the goal of this study is to gain an understanding of how various point defects can influence the mechanical properties of $LaRu_2P_2$, instead of an investigation into how this specific composition led to the response of this specific micropillar.

To better understand whether a single phase or a two-phase composite model is more appropriate, we plot the derivative of all stress-strain curves, the tangent moduli, in Figure 38(d). From this, we see that the responses of $LaRu_{1.5}P_2$ and $LaRu_2P_{1.5}$ do not show softening, while the responses of the composite models, as well as the experimental results, clearly do. These results suggest that the experimental observations of small amounts of softening are a result of dispersed regions of high defect concentrations in a matrix of pure $LaRu_2P_2$.

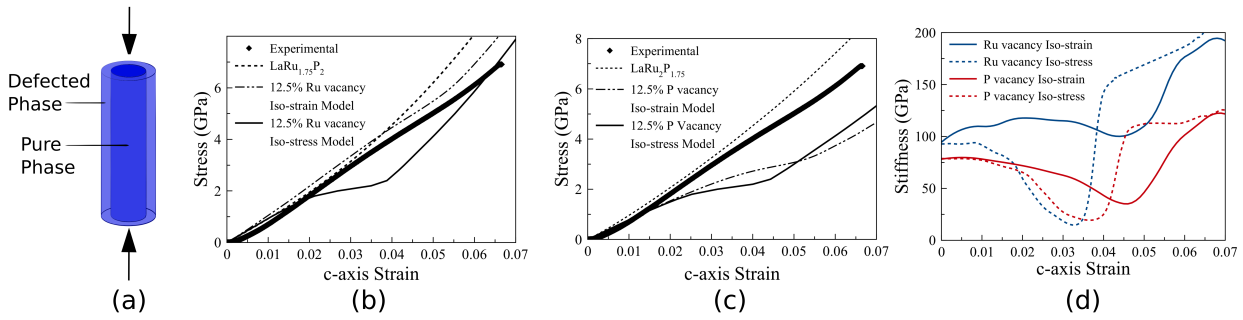

Figure 38: (a) The response of a defected micropillar of $LaRu_2P_2$ was modeled using an iso-strain model, which can conveniently be visualized as two concentric phases. (b) The stress-strain response of a composite of one half pure $LaRu_2P_2$ and one half of a 25% Ru vacancy structure. (c) The stress-strain response of a composite of one half pure $LaRu_2P_2$, and one half 25% P vacancy structure. The mechanical response of the pure defected structures exhibit no softening. However, the composite models show softening similar to that of the experimental results.

4.2.1 Eshelby's Inclusion Model

To further model the possible response of a two-phase sample, Eshelby's inclusion models were developed representing the same overall concentrations. Unlike the iso-stress and iso-strain models, Eshelby's Inclusion models take into account the effects of coherency between the two phases. We computed the response of the dilute limit, which assumes that the response of the matrix is not affected by the response of the inclusion. The inclusion was modeled as a coherent sphere of one phase embedded in a matrix of the other phase. The elastic stiffness tensors were homogenized based on a tangent homogenization model. In our problem, further complications arise since at least one of the materials is not linear elastic. The nonlinearity of the response of the pure $LaRu_2P_2$ was addressed by computing the full elastic constant tensor point-wise along the uniaxial stress strain curve. This was done by first computing the tangent elastic constants along the whole strain path, and splining the data to create a continuous set of elastic constants. Meanwhile, the elastic stiffness tensor of the defected phase was assumed to be constant with respect to strain (linear elastic). The Eshelby tensor in the pure-phase inclusion models was computed based on the elastic constants of the pure phase at that strain. These models show reduced (or eliminated) softening in the stress-strain curve and provide another set of bounds for the possible outcome of this composite.

As with the iso-strain models constructed for this study, the overall strain (ε^0) was specified, and the resulting stress in the composite was calculated. The model marches in overall strain, and the effective elastic tensor ($\bar{C}$) is calculated. This is done by first iteratively solving for the individual strains in each phase. Initial guesses were provided for the individual phases' strains. For the first strain step, the iso-strain condition was provided as the initial guess, while in subsequent strain steps, the previous solution was provided as an initial guess. These strains, particularly the strain in the pure $LaRu_2P_2$ phase were used to calculate the strain localization tensor ($\mathcal{A}^I$) which, in turn was used to calculate the strain in the inclusion by:

$$\varepsilon^I = \mathcal{A}^I : \varepsilon^0 \tag{4.3}$$

and the strain in the matrix was then be calculated by:

$$\varepsilon^M = \frac{1}{1-\phi}(\varepsilon^0 - \phi\varepsilon^I) \tag{4.4}$$

These individual strains were then used to calculate the strain localization in the inclusion, and thus the loop was repeated. The individual strains were considered converged when the difference in the individual strains calculated by successive iterations was less than 1×10^{-4}.

With the individual strains calculated, the effective stiffness tensor and the effective compliance tensor were calculated for a given total strain, and the uniaxial stress increment $d\sigma$ was calculated by:

$$d\sigma = \frac{1}{\bar{S}_{3333}(\varepsilon^0)} \tag{4.5}$$

which, due to the employment of tangent modulus homogenization, can be integrated up to the stress at a given strain by:

$$\sigma(\varepsilon^0) = \int_0^{\varepsilon^0} d\sigma \tag{4.6}$$

The dilute inclusion composite model was constructed for composites of pure $LaRu_2P_2$ and either the ruthenium vacancy structure or the phosphorus vacancy structure. The results of these models are shown in Figure 39.

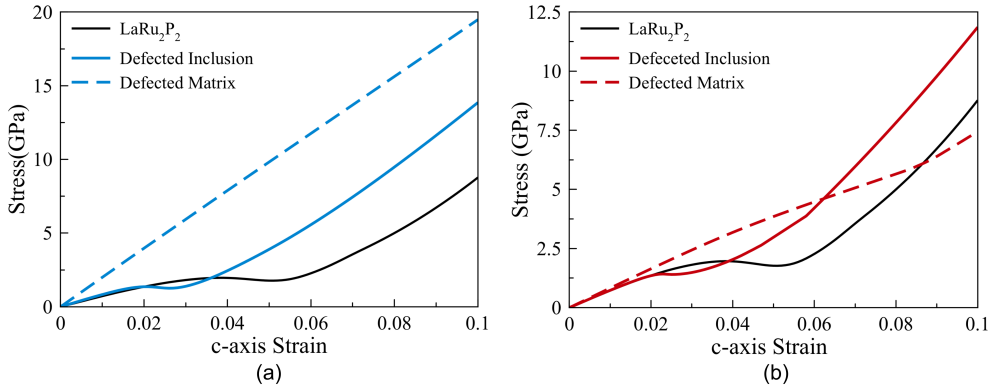

Figure 39: Dilute approximation composite model considering a spherical inclusion for ruthenium vacancies (a) and phosphorus vacancies (b). Both a defected inclusion and a defected matrix were considered for both investigated defect structures.

4.2.2 Discussion

These simulations offer insight into the nature of types, distributions, and mechanical responses of defected regions in $LaRu_2P_2$. Of the potential defected structures investigated that could give rise to the experimentally observed compositions, it is reasonable to rule out the potential presence of lanthanum interstitials since they are energetically unfavorable and mechanically unstable at high concentrations. The formation energies of vacancies in $LaRu_2P_2$ reveal that both phosphorus and ruthenium vacancies have significantly lower formation energies than lanthanum vacancies, about 2.0 eV and 2.3 eV lower, respectively. This indicates that forming ruthenium and phosphorus vacancies is easier than forming lanthanum vacancies. This also agrees with the compositions observed experimentally.

On one hand, this could be surprising. The Ru–P cage, considered the active unit in the facilitation of superconductivity [153], might be expected to be a difficult structure to damage. However, this is not uncommon; defected cages have been observed in other systems, including K-Fe-Se [154]. On the other hand, the $ThCr_2Si_2$ structure can also be thought of as alternating layers of La cations and $[Ru_2P_2]$ anions [17]. From that perspective, a cation vacancy from an ionic crystal would be expected to be very energetically expensive. It would appear from our calculations the ionic nature of the materials is more important, and thus the cage is easier to damage.

The introduction of point defects in the ruthenium-phosphorus cage also demonstrates the ability to alter the nature of collapse of the structure. It is clear from our supercell calculations, including the use of special quasirandom structures, that even small amounts of phosphorus defects cause the structure to collapse as none of our supercells with at least one phosphorus vacancy were un-collapsed. In contrast, it takes a ruthenium vacancy concentration of about 7% or more to collapse the structure. This transition, via vacancies, also alters the mechanical response creating a monotonically increasing stress-strain curve.

Since it is postulated that covalent bonds forming between the phosphorus atoms are responsible for the collapsed state, they also must impact the stiffness. This idea is supported by our stress-strain curves, which show that all the defected supercells are stiffer than stoichiometric $LaRu_2P_2$,

regardless of whether they are ruthenium or phosphorus vacancies. As more ruthenium vacancies are introduced into the structure, we see that the material becomes stiffer (Figure 36(a)). In this case, an increase in ruthenium vacancies pulls the structure into a more collapsed state, which further stiffens the structure. However, the opposite trend is observed for phosphorus vacancies (Figure 36(b)). This is likely due to competition between the collapsing nature of vacancies and fewer P–P bonds available to stiffen the structure.

While the introduction of a large fraction of point defects in the crystal prevents collapse completely, softening can be reintroduced by segregation of the same defects. Our composite models shows that a shallow softening region is possible when both pristine and defected regions coexist. Thus, one might expect more softening to exist as the crystal is annealed and the point defects cluster together. It is also worth pointing out that the composite model constructed with the ruthenium vacancy structure shows better agreement with experiments than the one constructed with the phosphorus vacancy structure. However, caution should be taken when arriving at this conclusion. One must account for the accuracy of DFT simulations, experimental uncertainty in measuring the stiffness, as well as compositional uncertainties and the models lack of representing the interaction of Ru and P defects present in the actual experiments.

The inclusion models also agree qualitatively with the simpler iso-strain and iso-stress models. They show reduced softening from the pure $LaRu_2P_2$ response. There are several approximations which limit this model, however. Firstly, the inclusion models assume a low inclusion fraction, and thus 50% inclusion phase fraction is pushing the limits of this theory. Furthermore, this inclusion model cannot simulate percolated inclusions, which are very likely present in the sample. Simulating such inclusions would require high-level numerical computational models, such as finite element simulation, which could be pursued in the future. Nevertheless, the model above supports our previous findings, that a composite model of pure and defected phases can explain the potential mechanisms behind the experimental results observed in the microcompression tests.

4.3 Investigations of Defected $CaFe_2As_2$

Like $LaRu_2P_2$, the presence of defects would be expected to have an impact on the mechanical response of $CaFe_2As_2$. These defects may be present in $CaFe_2As_2$ due to processing. Efforts to decrease the time of production of ternary iron-arsenides have led to production of crystals in FeAs flux, as opposed to standard Sn flux, which offers significant improvements in crystal growth time [155–157]. In this vein, crystals of $CaFe_2As_2$ were grown in FeAs flux at Ames Laboratory in Iowa. Micropillars were FIB milled from these crystals and uniaxial compression investigations of these crystals were performed by our experimental collaborators at the University of Connecticut.

Uniaxial compression tests of these micropillars revealed mechanical responses devoid of the characteristic pseudo-elastic response achieved with crystals grown in Sn flux, and the response predicted by DFT (Section 3.1). The responses of the micropillars did not have a softening region, which was present in the mechanical response of $CaFe_2As_2$ grown in Sn flux. These crystals were annealed, and compression of micropillars milled from the annealed crystal exhibited a pseudo-elasticity response which was very similar to the response from crystals grown in Sn flux. The uniaxial compression test results are plotted in Figure 40.

During the annealing process, a secondary phase precipitated out and formed coherent interface boundaries with the parent $CaFe_2As_2$ crystal. The measured composition of the precipitate is iron and arsenic at a ratio of 1:1, suggesting that it is most likely stoichiometric FeAs. This brings up some important questions worth investigating. Is the precipitate indeed FeAs, and if so what is the expected orientation of the two phases after annealing? What defects would contribute to the crystal precipitating FeAs upon annealing? How would these defects affect the mechanical response of $CaFe_2As_2$?

Coherency Between the Matrix and the Precipitate

The FeAs precipitate has an orthorhombic unit cell with experimental room temperature lattice constants of $a = 3.37$ Å, $b = 5.44$ Å, and $c = 6.03$ Å [158]. Investigations of FeAs at 4 K by Rodriguez et al. confirmed that FeAs is also antiferromagnetic at low temperatures with a Néel

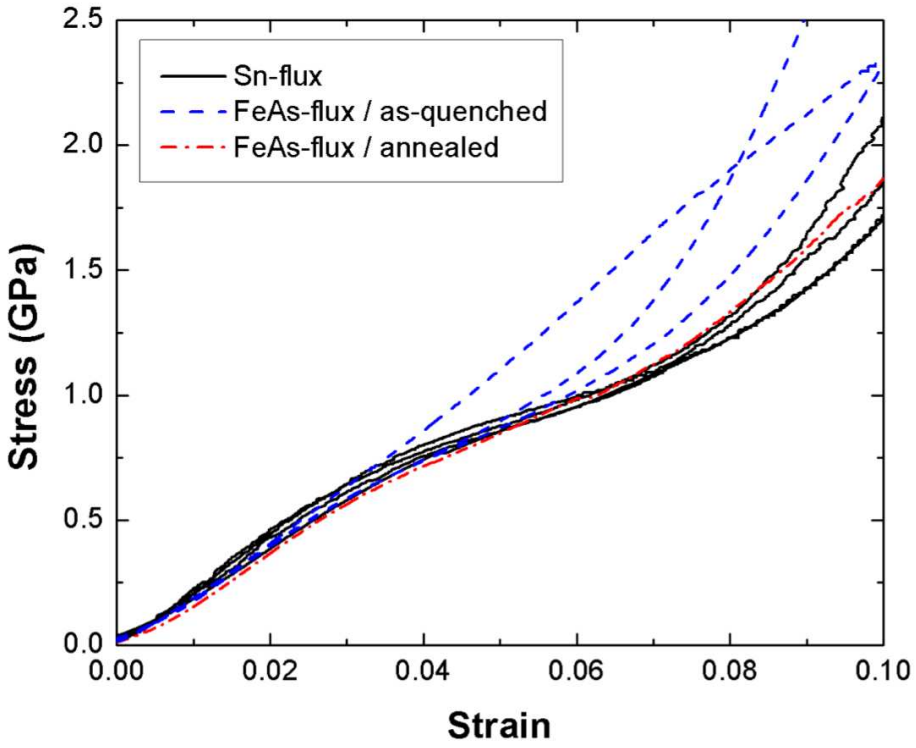

Figure 40: The stress-strain responses of $CaFe_2As_2$ crystals grown in FeAs flux when quenched do not exhibit the pseudo-elastic response of samples grown in Sn flux. However, they do exhibit pseudo-elasticity after annealing. Figure provided by Dr. Seok-Woo Lee of UCONN.

temperature of 69.6 K [159]. Our own DFT relaxation of antiferromagnetic FeAs was performed which confirmed the magnetic state of the phase as well as the lattice constants, which were computed to be: 3.38 Å, 5.31 Å, and 5.96 Å, respectively.

Since the interface between the precipitate FeAs and the parent $CaFe_2As_2$ was reported to be coherent, the two phases must be oriented in such a way that there is minimal lattice mismatch. There are two possible orientations between $CaFe_2As_2$ and the precipitated phase which could potentially create a coherent boundary. Both involve the c-axes of the phases being parallel. The first lines up the b-axes (Figure 41a and 41b), while the second lines up the a-axes (Figure 41c and 41d).

The first orientation has a DFT lattice constant mismatch of 3.0% in the b directions and a mismatch of 2.8% in the c directions (where one unit cell of $CaFe_2As_2$ is measured against 2

unit cells of FeAs). These lattice constant mismatches at 300 K are 1.0% and 2.5% respectively. For the second orientation, the lattice mismatch as predicted by DFT at 0 K in the a direction is 16.6%, while the 300 K experimental lattice mismatch would be 14.2%. The lattice mismatch in the c direction is the same for both orientations. The lattice mismatches for these orientations were computed for 300 K, in addition to 0 K, because the coherent boundary between the two phases was observed at room temperature. We believe the former relationship, since it is coherent regardless of temperature, was observed in the annealed sample grown in FeAs-flux (Figure 41e).

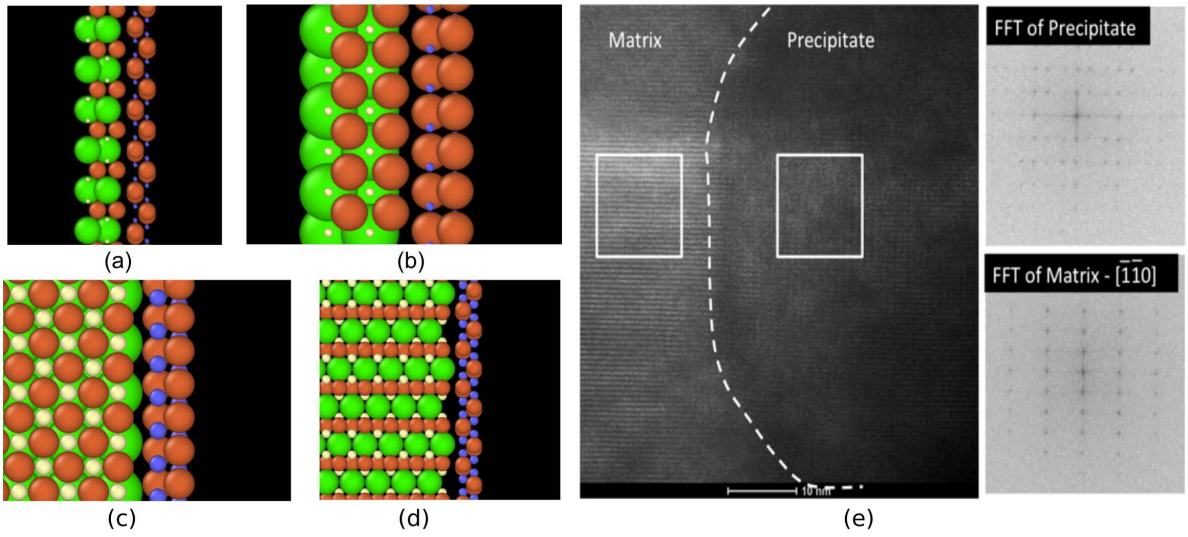

Figure 41: Potential coherent interfaces between $CaFe_2As_2$ and FeAs. Matching the [010] directions and the [001] directions (a) and (b), or matching the [100] directions and the [001] directions (c) and (d). (e) The observed coherent boundary between the parent $CaFe_2As_2$ and the FeAs precipitate (image provided by Dr. Seok-Woo Lee of UCONN).

EDX data of the composition of the sample was obtained to investigate which defects are present in the crystal and contributing to the precipitates observed upon annealing. Unfortunately, the data does not show definitive evidence of compositional deviations from stoichiometry. However, imaging of the sample revealed some clues as to the microstructures present. Prior to the annealing of the crystal, high resolution TEM images of the sample taken down the [001] direction show a tweed-like pattern (Figure 42(a)). This pattern was not observed in TEM images taken down the [110] axis. This pattern has been observed before in $CaFe_2As_2$ grown in FeAs

flux [156, 157]. It has been proposed that this pattern is indicative of the presence of calcium defects.

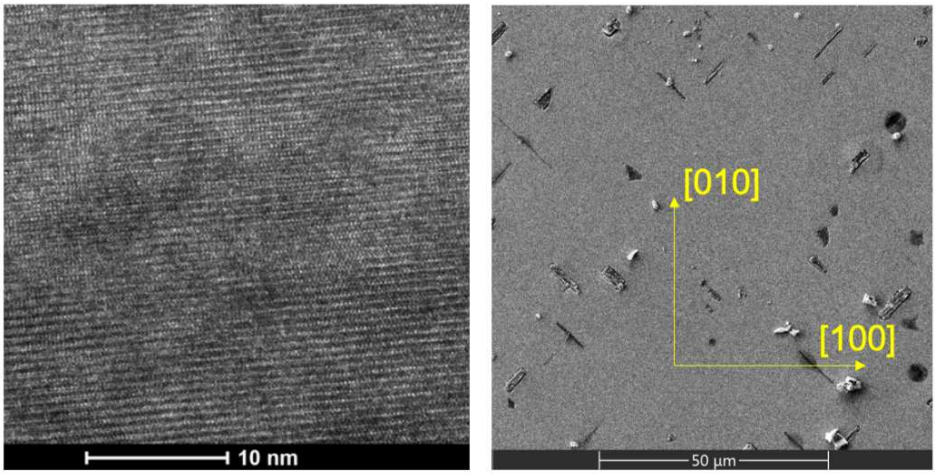

Figure 42: (a) Transmission electron microscope (TEM) images along the [001] direction show the tweed-like pattern on the surface. (b) Scanning electron microscope (SEM) images of the crystal along the [001] direction reveal that the FeAs precipitates are oriented along the $\langle 110 \rangle$ directions of the tetragonal phase ([100] and [010] directions of the orthorhombic phase). Images provided by Dr. Seok-Woo Lee of UCONN.

After annealing, SEM images show the presence of FeAs precipitates oriented exclusively along the $\langle 110 \rangle$ directions of the crystal (Figure 42(b)). Since these images were taken at room temperature, well above the Néel temperature of $CaFe_2As_2$, the crystal is in its paramagnetic tetragonal phase. Thus, the $\langle 110 \rangle$ direction in this image corresponds to the [100] direction or the [001] direction in the antiferromagnetic orthorhombic phase (without the distortion of the magnetic ordering, they are equivalent directions). This is congruent with orientation relationship for coherent boundaries between the matrix and the precipitate proposed earlier in this section. The c-axis length of the sample was measured prior to annealing to be shorter than the c-axis of $CaFe_2As_2$ grown in Sn flux and or the sample after annealing. This is consistent with other observations of FeAs-grown $CaFe_2As_2$ [160]. This suggests that the sample has a considerable number of vacancies quenched in.

From these experimental results, and conclusions of previous studies, we hypothesize that the as-quenched $CaFe_2As_2$ sample grown in FeAs flux is highly calcium-deficient, which is manifested in a large number of calcium vacancies which produce the observed tweed pattern and shortened c-axis length. Upon annealing, precipitates of FeAs form coherent boundaries with the now-pure $CaFe_2As_2$ along the [110] direction of the tetragonal unit cell, which agrees with the boundary orientation we proposed.

4.3.1 Computational Investigations of Isolated Defects

To investigate how the defects present in the sample contribute to the experimentally observed compression response, we performed a thorough study of defects in $CaFe_2As_2$. To provide insight into which defects should be expected to form, isolated defects energies were calculated for interstitials and vacancies of all elements: Ca, Fe, and As. Using the same methods as the investigations of isolated defects in $LaRu_2P_2$ (Section 4.1.2), the cohesive energies of all possible Ca–Fe–As compounds were computed and compiled into a ternary phase diagram (Figure 43). Several compounds were investigated for their stability, and due to the magnetic nature of iron, many needed to be investigated for their magnetic ordering.

There are a few interesting results from this phase diagram. The first is that no Ca–Fe structures are on the phase diagram. This is because iron and calcium are immiscible [161]. Secondly, $CaFe_2As_2$ is the only ternary compound to be stable at 0 K. However, several other ternary compounds had been previously reported. $CaFeAs_2$ [128], $CaFe_4As_3$ [129], and arrays of $CaFe_5As_3$ [162] have all been previously investigated experimentally. While these compounds are not stable at 0 K, they may be stable at higher temperatures.

With this ternary phase diagram, the isolated defect energies were calculated through the methods described in Section 4.1.2. Vacancy and interstitial formation energies were computed from supercells containing a single defect. If the supercells comprised of 160 atoms without a defect, and thus, with a vacancy were 159 atoms, and with an interstitial were 161 atoms. The chemi-

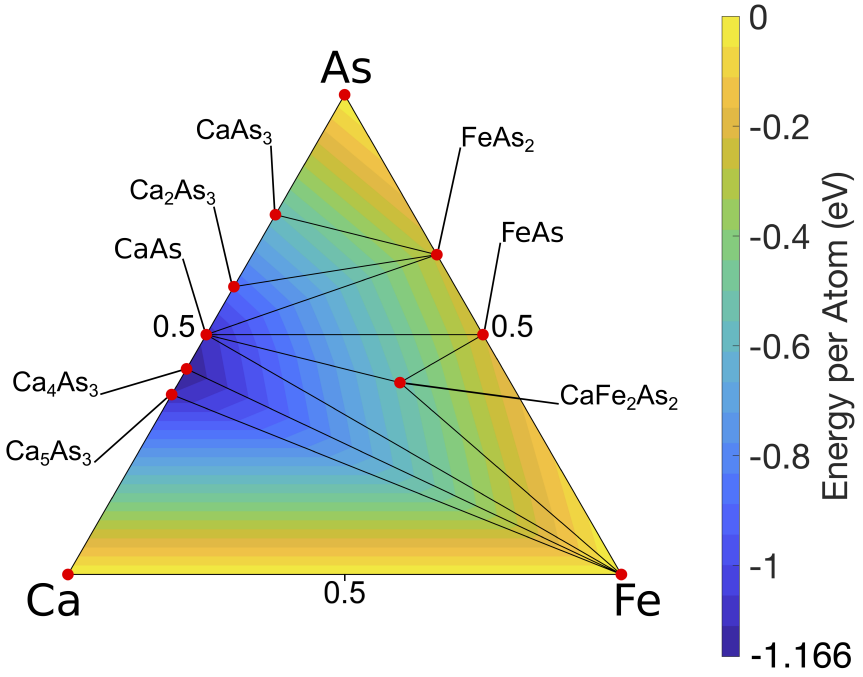

Figure 43: The calcium-iron-arsenic 0 K ternary phase diagram reveals that $CaFe_2As_2$ is the only ternary compound to exist on the convex hull. The red dots indicate compounds which were determined to be stable.

cal potentials computed from the convex hull assume a neutral chemical environment, which of course, is not the environment in which our sample was grown.

The computed defect energies are tabulated in Table 10. From this we learn that calcium vacancies, which have been proposed to be present in as-quenched FeAs-grown $CaFe_2As_2$ [156, 157], have a reasonably low formation energy in a neutral chemical environment. While they are not the lowest-energy vacancy in this environment, in a FeAs-rich chemical environment, it is likely that their formation is very favorable. Interestingly, iron has a vacancy formation energy of 0.233 eV in a chemically neutral environment, which is low. This may explain the observation of the phase $CaFeAs_2$, even though that phase does not lie on the convex hull.

The interstitial formation energies are generally higher than vacancy formation energies, with the exception of the iron interstitial (1.95 eV), which has a lower formation energy than an arsenic vacancy (2.09 eV). All elements have a preferred vacancy site. Calcium and iron prefer the cage

Table 10: The calculated isolated defect energies of $CaFe_2As_2$ and the necessary reference structures used to calculate the defect energies.

		Calcium	Iron	Arsenic
Vacancies	Energy	0.699 eV	0.233 eV	2.09 eV
	Reference Structures	$CaFe_2As_2$, FeAs	FeAs, $CaFe_2As_2$, CaAs	CaAs, Fe, $CaFe_2As_2$
Interstitials	Cage Energy	4.32 eV	1.95 eV	8.23 eV
	Octahedral Energy	7.70 eV	4.02 eV	2.71 eV
	Reference Structures	CaAs, Fe, $CaFe_2As_2$	$CaFe_2As_2$, Fe	CaAs, $CaFe_2As_2$, FeAs

site (4.32 eV and 1.95 eV, respectively) to the octahedral site (7.70 eV and 4.02 eV, respectively), while arsenic prefers the octahedral site (2.71 eV) to the cage site (8.23 eV).

4.3.2 Investigations of Defects at High Concentrations

Defects in the observed sample must be at much higher concentrations than those simulated in this isolated defect investigation in the previous section. For that reason, defects at high concentrations were studied for their potential contributions to observed response of the sample, and their potential to influence the response of other samples (perhaps containing different defects). Again, our hypothesis is that the experimentally observed crystal response can be explained by the effects of the presence of defects. We propose that the as-quenched crystal is defected, and when annealed, these defects are able to anneal out, resulting in a pure matrix with FeAs precipitates. We explored the mechanical properties of crystals with a high concentrations of a variety of possible defects.

Iron and Arsenic Interstitials

There are multiple explanations for which defects could contribute to this scenario. Specifically, iron and arsenic interstitials could stiffen the crystal and anneal out as the FeAs phase. These deviations in stoichiometry might be expected due to the nature of growth in FeAs flux. While there is no experimental evidence pointing to iron and arsenic interstitials (as there is for calcium

vacancies), this is still a possibility worth exploring. Similar to $LaRu_2P_2$, both arsenic and iron interstitials were found to be mechanically unstable at concentrations of one interstitial per conventional unit cell. This would produce stoichiometric ratios of 4:9:8 and 4:8:9, respectively. Both the cage and the octahedral site were found to be unstable, thus ruling out the possibility of a sample containing a large amount of these interstitials.

Calcium Vacancies

Conversely, calcium vacancies could contribute to a stoichiometry which would produce FeAs precipitates. Calcium vacancies, on the other hand, were found to be indeed stable. Removal of a single calcium atom from the conventional unit cell produced a 25% Ca vacancy structure. The 25% calcium vacancy structure, while stable, doesn't exhibit a response which could contribute to the experimental response observed in the sample. This vacancy concentration is achieved by removing one Ca from the orthorhombic unit cell (Figure 44(a)).

Based on our experience with defects in $LaRu_2P_2$, we look for markers which indicate the lack of a pseudo-elastic response. This would be an induced crystal collapse, which would present itself as a shorter c-axis length, and in the case of $CaFe_2As_2$ a collapse in the magnetic moments of the iron atoms. Calcium vacancies do not induce crystal collapse, nor do they induce collapse of the magnetism in the crystal. Under no applied pressure, the c-axis length is 11.55 Å, which is roughly the same as a unit cell of $CaFe_2As_2$ without a calcium vacancy, and the iron atoms preserve their magnetic moments. Under compression, the stress-strain response of the calcium vacancy structure has two distinct regions. The initial compression region, at the end of which, the magnetism gradually and smoothly reduces to 0. At this point, at a c-axis length of approximately 10.25 Å, the crystal becomes nonmagnetic and continues with a stiffer stress-strain response.

A second calcium can be removed from the unit cell producing 50% calcium vacancy structures. The second calcium vacancy can either be placed in the same plane as the first calcium vacancy, or in the other plane. The former produces a structure where every other Ca layer is vacant, while the latter produces a structure where all Ca layers are equally populated. The two structures can be seen in Figure 45(a) and (b).

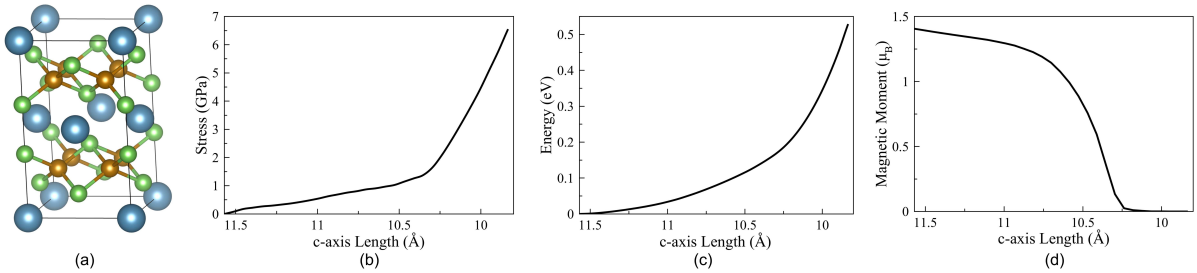

Figure 44: The 25% calcium vacancy structure (a), when compressed, exhibits two distinct nearly linear regions of the stress-strain response (b), and no local energy minimum (c). (d) unlike the compression of pure $CaFe_2As_2$, the magnetic moments smoothly drop to 0 as the crystal collapses.

Analysis of the ground states of these two structures reveals that removing half the calciums from each layer (uniform vacancy structure), as opposed to removing every other layer (layered structure), is energetically favorable. Furthermore, the antiferromagnetic stripe pattern found in pure $CaFe_2As_2$ (and other iron-arsenides as well) is the present in the ground state of both structures. The zero-stress c-axis length of the uniform two-calcium vacancy structure is 12.01 Å. Compression of this structure reveals a second stress minimum at a c-axis length of approximately 11.11 Å (Figure 45(c)). The stress at this minimum is only 38.2 MPa, which is very small in terms of DFT. It is very possible that this point is a local energy minimum, or even the true ground state. During the compression, the magnetic moments of the iron atoms gradually decrease (Figure 45(e)). The zero-stress nonmagnetic structure is indeed higher energy than the antiferromagnetic stressed state at that c-axis length, indicating that the crystal should exist in the magnetic state.

Iron Vacancies

Removing one of the eight iron atoms from the conventional unit cell yields a 12.5% iron vacancy concentration. According to the ternary phase diagram, iron vacancies would decompose into $CaFe_2As_2$, CaAs, and FeAs, so there is a possibility that upon annealing, $CaFe_2As_2$ with iron vacancies could decompose into a matrix of $CaFe_2As_2$ with the observed FeAs precipitates. Iron vacancies are the lowest-energy point defect (in a chemically neutral environment). The ground

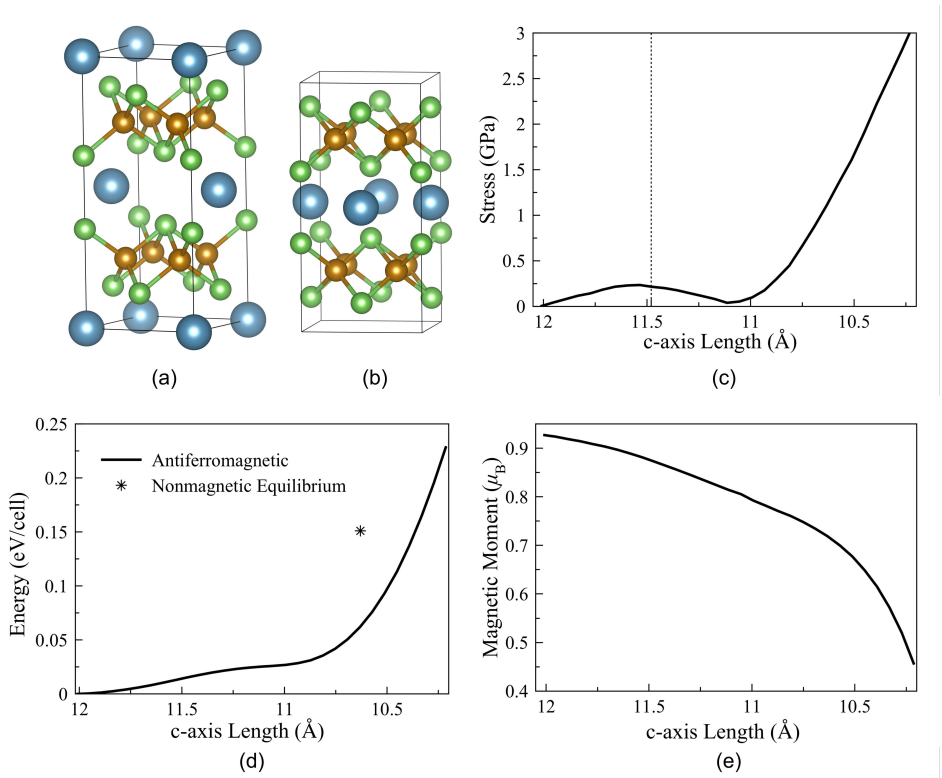

Figure 45: The 50% calcium vacancy structures: (a) one vacancy in each calcium layer, and (b) every other calcium layer removed. The former has an extended c-axis, a lower overall energy, and preserves its antiferromagnetic state. (b) Compressed uniaxially about the c-axis, the crystal reaches a local stress minimum around $c = 11.11$ Å, with a nearly zero stress. (d) The energy curve of the compression of the antiferromagnetic phase shows that it is energetically favorable compared to the nonmagnetic state at that strain. (d) During compression, the magnetic moments of the iron atoms gradually decrease.

state magnetic configuration of this structure is ferrimagnetic. The removal of one iron (Figure 46(a)) doesn't significantly affect the magnetism exhibited by the other iron atoms. Since there are an odd number of iron atoms in this structure, the magnetic moments do not completely cancel out, and there is a net magnetism.

When compressed uniaxially, the crystal undergoes a magnetic and structural collapse at approximately 2% c-axis strain. Upon collapse, the crystal is in a state of tension, and continues to compress with an elastic response, through the 0-stress point. This response is shown in Figure 46(b). The energy-strain response Figure 46(c) clearly shows two phases, with a transition at approximately 2% c-axis strain.

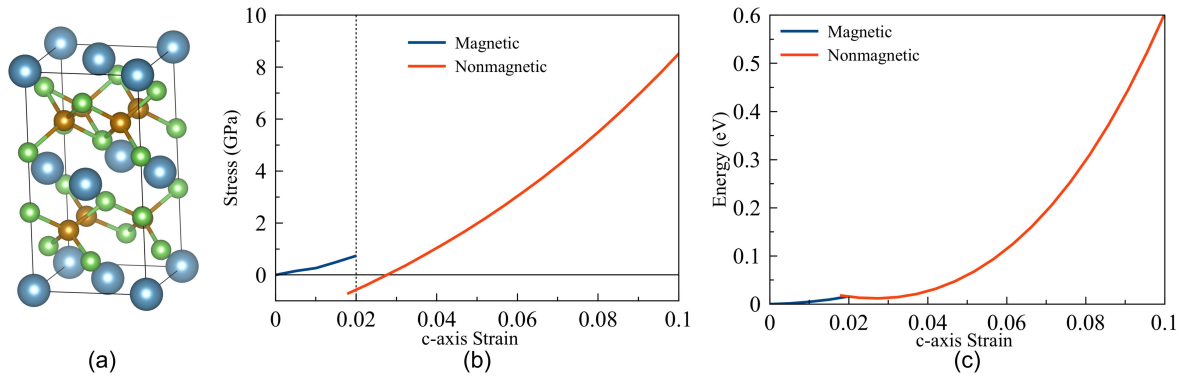

Figure 46: (a) The 12.5% iron vacancy structure collapses structurally and magnetically at approximately 2% c-axis strain (b). The energy-strain response shows two distinct magnetic phases.

Arsenic Vacancies

Based on the Ca–Fe–As convex hull, arsenic vacancies cannot contribute to the observed precipitation during annealing. However, it is still interesting to investigate what the effect of such vacancies might be. Arsenic vacancies are the most energetically costly to produce, roughly 3 times the formation energy of calcium vacancies, the next highest-energy vacancy. At concentrations of 12.5%, they do not interrupt the antiferromagnetic ordering of the crystal. The horizontal stripe AF ordering is still the most energetically favorable.

When compressed, the crystal undergoes a magnetic collapse at approximately 10% c-axis strain. This is associated with a clear second phase, with a different energy and stress-strain curve. It is interesting to note that this magnetic collapse occurs only in the non-defected cage. The magnetic moments of the iron atoms in the defected cage do not collapse. The crystal was strained out to 15% c-axis strain and a magnetic collapse of the defected cage was not observed.

This defect structure has a particularly interesting mechanical and magnetic response to compression. While there have been reports of iron arsenides with the $ThCr_2Si_2$-type structure, specifically $CaKFe_4As_4$ exhibiting a “half-collapsed" phase (see Section 5.1.2), those phases are not truly “half-collapsed" since the magnetic moments of all iron atoms collapse simultaneously. The presence of arsenic vacancies, however, causes only one half of the iron atoms to lose their magnetic

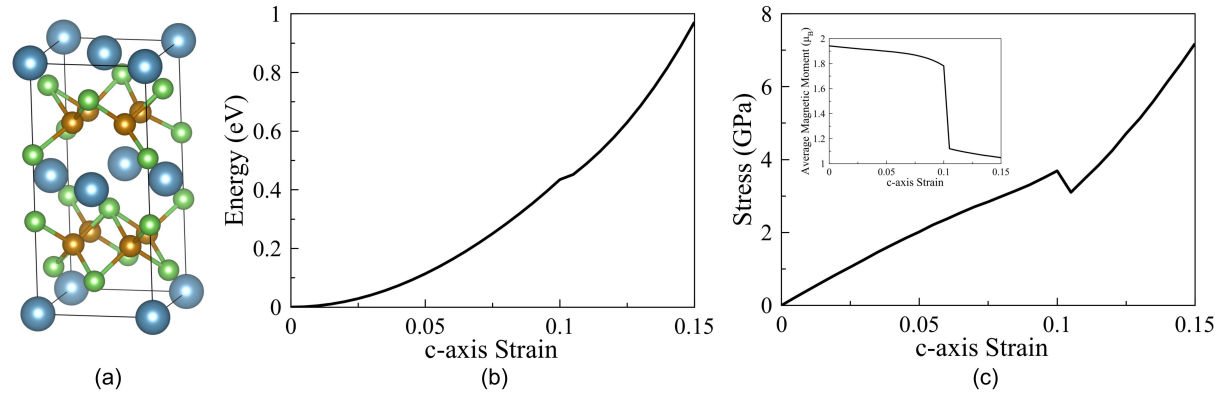

Figure 47: Compression of the 12.5% arsenic vacancy structure (a) shows a mostly elastic response, with a crystal collapse at approximately 10% c-axis strain. This is associated with an abrupt drop, but not elimination, of the magnetism.

moments at a critical strain. This behavior is unique for defected structures of $CaFe_2As_2$ and may be important for future investigations.

4.3.3 Composite Models of Defected $CaFe_2As_2$

The responses of the high-concentration defected structures from Section 4.3.2 revealed several unique mechanical responses. Some defected structures exhibit phase changes which could be useful in explaining the experimentally-observed uniaxial stress-strain curves. Since we do not have any composition data to aim for, we will consider the possibility of segregated regions of defected and pure $CaFe_2As_2$. This was accomplished by the same approach as the defected composite models constructed in the investigation of defected $LaRu_2P_2$ in Section 4.2. Iso-strain models were produced to simulate the potential response of such configurations, as a means of describing a sample with segregated defects.

For this investigation, four such models were constructed. The models constructed were composites of pure $CaFe_2As_2$ and single calcium vacancy structure, double calcium vacancy structure, or iron vacancy structure. These structures were chosen since they could contribute to the observed FeAs precipitation. Three of the models were simple iso-strain, one for each of the investigated structures.

The iso-strain model of 50% Fe vacancy structure was constructed with the nonmagnetic Fe vacancy phase. Since the energy difference between the 0-stress points of the magnetic and nonmagnetic phases is only 0.01 eV/atom, it is reasonable to approximate the response of the Fe vacancy structure to be only its nonmagnetic response. The model of 50% Fe vacancy structure exhibits no softening through 12% c-axis strain (Figure 48(a)).

Additionally, an iso-strain model of 50% single-Ca vacancy structure was constructed. The calcium vacancy structure exhibits 2 phases, each with a nearly linear stress-strain response. The initial response is softer than that of pure $CaFe_2As_2$, while the latter response is similar to that of the cT phase of pure $CaFe_2As_2$. The composite response of pure $CaFe_2As_2$ and the Ca vacancy structure was soft, but nearly linear until approximately 11% c-axis strain, and then stiffer beyond that strain (Figure 48(b)).

A model was constructed with the double-calcium vacancy structure. This structure has a second stress minimum at a c-axis off 11.11 Å. The model was constructed considering this second minimum to be the equilibrium point of this double calcium vacancy structure. This model was another simple iso-strain model, half pure $CaFe_2As_2$ and half double calcium vacancy structure. The resulting stress-strain response of this model is nearly linear, until the pure $CaFe_2As_2$ is entirely the collapsed tetragonal phase (approximately 11% c-axis strain), when the stress-strain response of the model stiffens (Figure 48(c)).

4.3.4 Discussion

This investigation into defected $CaFe_2As_2$ structures sought to explain the observed response of the FeAs-grown $CaFe_2As_2$. Prior to annealing, the uniaxial compression response exhibited none of the softening characteristic of the pseudo-elastic response expected from $CaFe_2As_2$. Upon annealing however, FeAs precipitated out, and the pseudo-elastic response was observed. Based on the convex hull computed for the Ca–Fe–As ternary system, the sample must be either calcium deficient, iron deficient, or arsenic rich to decompose into $CaFe_2As_2$ and FeAs upon annealing. An arsenic rich or iron deficient sample would decompose into $CaFe_2As_2$, FeAs, and CaAs. Since

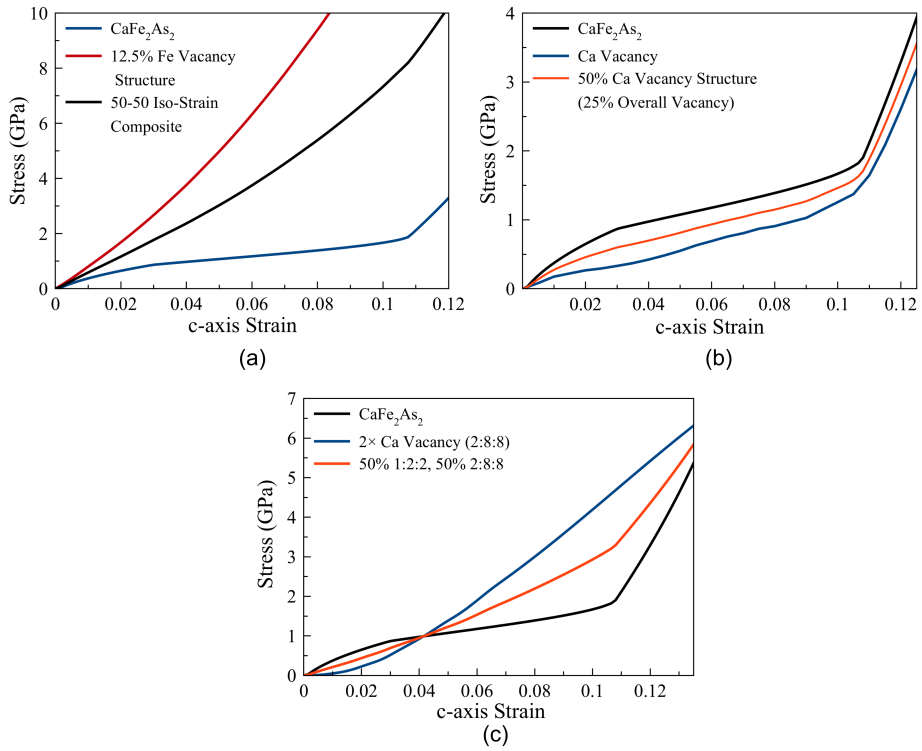

Figure 48: The iso-strain composite models of defected $CaFe_2As_2$. (a) The composite model of 50% $CaFe_2As_2$ and 50% Fe-vacancy could explain the observed response. (b) A composite model built with the single Ca vacancy structure. (c) A composite model built with the collapsed phase of the half-plane 2 Ca vacancy structure.

$CaFe_2As_2$ and FeAs form a coherent boundary, it may be possible that CaAs is kinetically limited in precipitating out, due to it not forming a coherent boundary with $CaFe_2As_2$.

However, a calcium deficient sample would decompose into only $CaFe_2As_2$ and FeAs. Furthermore, calcium vacancies have been previously reported in samples of $CaFe_2As_2$ grown in FeAs flux. The tweed-like pattern observed on the sample is indicative of calcium vacancies, which also corresponds to a shortened c-axis. The double calcium vacancy structure has a second minimum in stress, which is very close to 0 stress. It is possible that this second minimum, which has a c-axis length somewhat shorter than pure $CaFe_2As_2$ (11.11 Åvs. 11.52 Å), may be an equilibrium point which is also the initial point in the compression of the micropillar. Furthermore, the compression response of the double calcium vacancy structure exhibits no softening beyond the second mini-

mum point. Thus, this structure can contribute to the observed response of the micropillar, which is exemplified by the iso-strain composite model.

With knowledge of the composition of the lone precipitate (FeAs), observations of this sample and previous samples grown in FeAs flux, and experimental compression data of the sample and simulated compression data of defected structures, we propose that the sample grown in FeAs flux is calcium deficient. Prior to annealing, the sample contains a large concentration of calcium vacancies, which contribute to a visual tweed-like array. These vacancies most likely form the double calcium vacancy structure described in Section 4.3.2, which contributes to the suppression of the pseudo-elastic response. The shorter c-axis length of this structure, along with the compression response agree with experimental observations. Upon annealing, the sample decomposes into its stable phases: $CaFe_2As_2$ and FeAs. From our ternary phase diagram (Figure 43), this is the expected decomposition of a calcium deficient structure. After annealing, the pseudo-elastic response of $CaFe_2As_2$ is indeed observed. We conclude that this defected structure is responsible for the observed behavior of the FeAs flux-grown sample.

Chapter 5

Effects of Doping on $CaFe_2As_2$

$ThCr_2Si_2$-type crystals, up to this point, have been generously studied for their superconductive properties. The search for high-temperature superconductivity has led to investigations of alloying and doping these crystals. This is, in part, motivated by the notion that the presence of isovalent dopants can impart an intrinsic hydrostatic pressure on the microstructure-level, which could stabilize a superconductive state at zero applied stress. Other efforts to dope these crystals aimed at disrupting the magnetic ordering of the iron atoms, which could also stabilize superconductivity. If the presence of substitutional point defects can have such a strong effect on the electronic properties, it is worth investigating how these defects could effect the mechanical properties.

5.1 Calcium, Strontium, and Barium Iron Arsenides

Several studies have shown that the iron arsenides with alkaline earth metal A-type atoms (specifically Ca, Sr, and Ba) all have strikingly different mechanical responses, even though they are chemically similar. These three materials are a prime example of the variability in mechanical response with respect to chemistry. In contrast to the response of $CaFe_2As_2$, which has a single phase change, $BaFe_2As_2$ has been reported to exhibit 2 phase changes at very high pressures [20]. These phase changes are significantly weaker than the phase change of $CaFe_2As_2$. As re-examined by this work, these phase changes can be seen in Figure 49(a). The first phase transition, around 15% volumetric strain and 15 GPa, is associated with a collapse of the magnetic moments on the iron atoms. The second phase change is more subtle. This is associated with a change in the c-axis strain response to applied stress. This Further studies have shown, similar to investigations of $CaFe_2As_2$, that these phase changes can occur at much lower uniaxial stresses [30].

Meanwhile, $SrFe_2As_2$ has one phase change, similar to $CaFe_2As_2$, but has been described as a weaker phase change than that of $CaFe_2As_2$ [3, 163]. This was reproduced for our work and shown in Figure 49(b). The energy of the magnetic and nonmagnetic phases do not show evidence

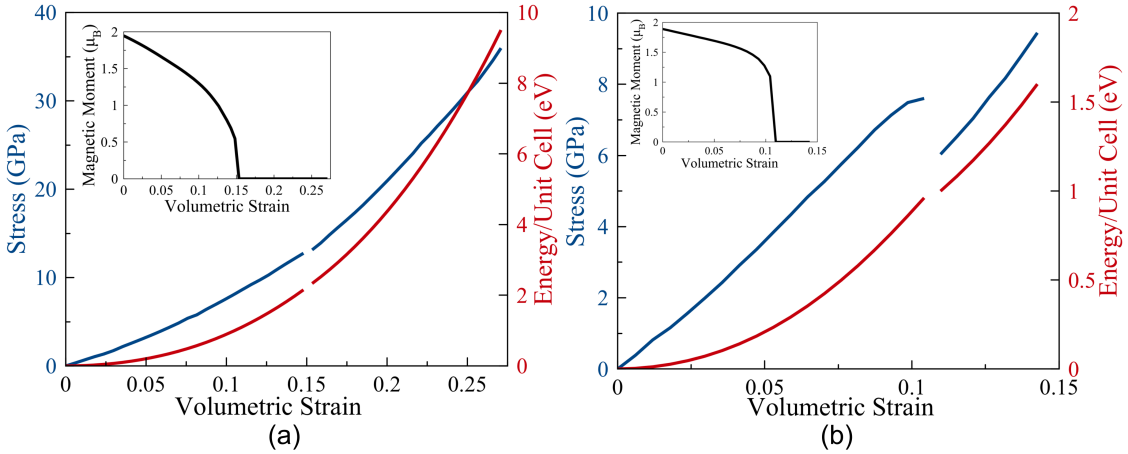

Figure 49: The response of $BaFe_2As_2$ (a), and $SrFe_2As_2$ (b), to applied hydrostatic pressure. Both compounds experience a magnetic collapse at a critical volumetric strain. $SrFe_2As_2$ experiences one phase transition, while $BaFe_2As_2$ experiences a second phase transition at a hydrostatic pressure around 30 GPa. Neither compound shows evidence of an energy barrier in unloading, it is unlikely that either experiences shape memory effects.

of a local energy minimum. It is therefore unlikely that the crystak will remain in the secondary phase upon unloading. Therefore, shape memory effects should not be expected. In some ways this is unexpected; since calcium, strontium, and barium are all alkaline earth metals, it would be reasonable to expect them all to have similar mechanical responses. However, since the phase change, and crystal collapse are the result of $[Fe_2As_2]$ layers bonding across A-type planes, the atomic radii of the A atoms would be of significant importance.

This presents an important question: how does doping $CaFe_2As_2$ with either barium of strontium affect its mechanical response? To address this question, simulations of compression of doped $CaFe_2As_2$ were performed. Different structural orderings were and varying concentrations of dopant (e.g. $Ca_{1-x}Ba_xFe_2As_2$) were investigated. The results of which are presented in the following sections.

5.1.1 Disordered Alloying

Presuming these materials would alloy in a similar fashion to common metallic alloys, there would be a random ordering of the A-type metal atoms throughout the material. To simulate this

random ordering with relatively small simulation cells, we again employ special quasi-random structures (SQSs) as we did in Section 4.1.4. SQSs were generated for dopant concentrations of 5%, 10%, 12.5%, 15%, 20%, 25%, 50%, 75%, 80%, 85%, 87.5%, 90% and 95%. In this work, A-type dopants are only considered to be present on A-type crystallographic sites, and dopant concentration is defined by the percentage of applicable A-type sites are occupied by dopant atoms as:

$$\chi_{\text{dop}} = \frac{N_{\text{dop}}}{N_{\text{dop}} + N_{\text{Ca}}} \tag{5.1}$$

Since we are interested in how the mechanical properties, particularly the phase change, might change or blend with concentration of dopant, these SQSs were relaxed and important phase-change parameters, such as c-axis length and transition strains, were extracted. First observed is effect of the alloying on the average c-axis of the crystal. The c-axis lengths, shown in Figure 50, change nearly linearly with dopant concentration between 100% $CaFe_2As_2$ and 100% A'Fe_2As_2, where A'=Ba, Sr. In other words, in these alloys, we see good agreement with Vegard's Law, which relates the lattice parameters of an alloyed solid to the linear interpolation between the two parent solids [164]:

$$a_{(A_{1-\chi}B_{\chi})} = (1-\chi)a_A + \chi a_B \tag{5.2}$$

While this doesn't tell us much, it does suggest that there may not be a critical concentration in which the properties shift between the two compounds. Perhaps some blending of the mechanical properties does occur with this type of doping.

To investigate this, select SQSs, with dopant concentrations 25%, 50%, and 75%, were compressed hydrostatically. The observed stress-strain curves revealed an interesting evolution of transitions. As the concentration of the dopant is increased, the transition strains also increased, approaching the behavior of the parent dopant compound. The stresses at which the the transition occurs also increase, approaching that of the parent dopant compound. This interpolating behavior occurs for doping with both barium and strontium. The stress-strain results can be seen in Figure 51.

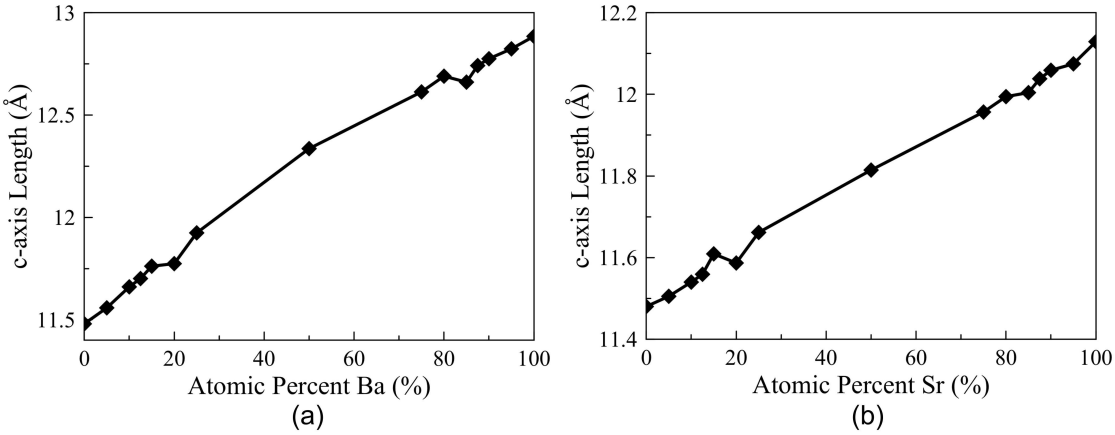

Figure 50: The average c-axis lengths of SQSs of $CaFe_2As_2$ alloyed with barium (a) or strontium (b) vary nearly linearly with concentration, blending between the c-axis lengths of $CaFe_2As_2$ and $BaFe_2As_2$ or $SrFe_2As_2$.

The transition strain and stresses, which can be used to describe the transition, were extracted and plotted in Figure 52. The volumetric strain at which the transition occurs varies almost linearly with the composition of the alloy for both Ca–Ba and Ca–Sr (Figure 52(a)). Likewise, the stresses at the onset and offset of the transition vary in a nearly linear fashion for both alloys of barium (Figure 52(b)) and alloys of strontium (Figure 52(c)). This suggests that in a disordered arrangement of A-type atoms, the properties of the transition can be tuned directly by the composition.

5.1.2 Ordered Structures

In the previous section, we explored the mechanical responses of potential randomly-ordered alloys of $CaFe_2As_2$ with Ba or Sr. This is not the only possible ordering of these alloys, however. There is also potential for doped compounds of this sort to form highly-ordered layered superstructures. This ordering would consist of entire layers of calcium replaced by the dopant metal. This structure has been observed and studied in $CaKFe_4As_4$ [165–168], which is $CaFe_2As_2$ doped with 50% potassium. In this structure, every other calcium layer in $CaFe_2As_2$ is instead a layer of potassium, forming the ordered superstructure (Figure 53(a)). For dopant concentrations other than 50% an appropriate fraction of calcium layers would be replaced by the dopant. For example,

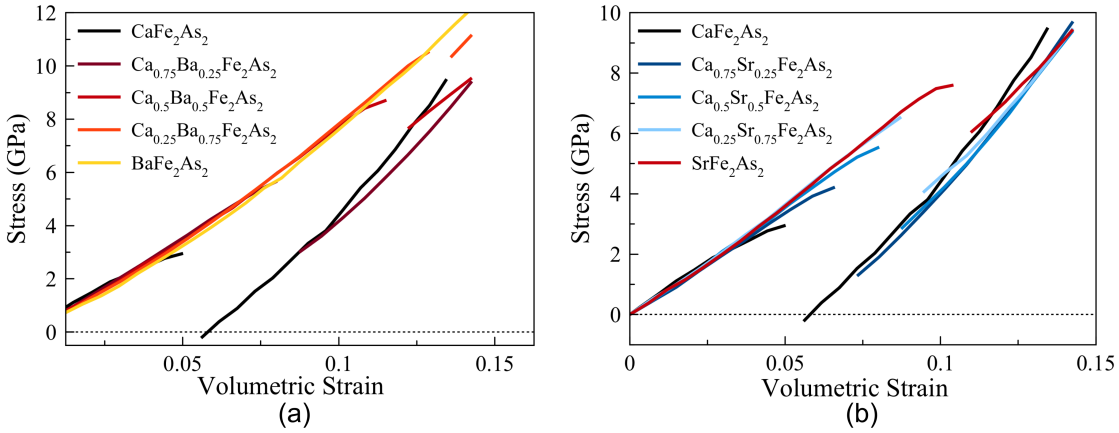

Figure 51: The doping of $CaFe_2As_2$ with barium (a) and strontium (b) in random ordering results in a blending of the mechanical properties.

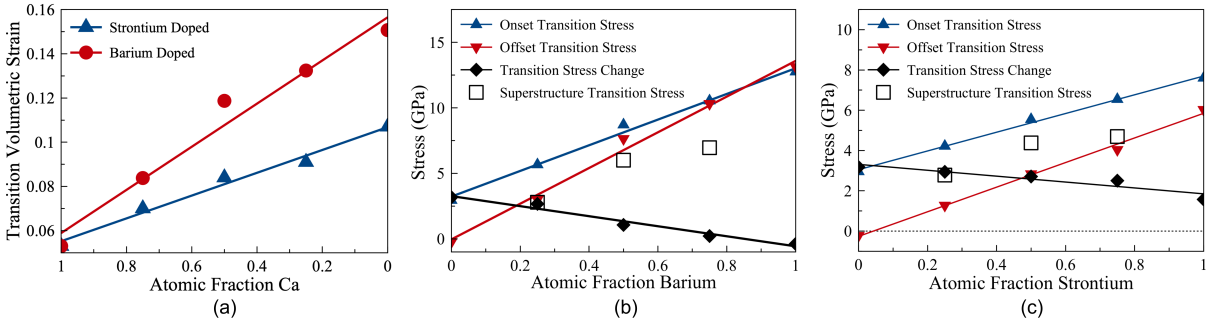

Figure 52: (a) The transition volumetric strains of both randomly-alloyed structures vary nearly linearly with concentration for both barium and strontium doping. The transition stresses also vary nearly linearly with concentration for both barium (b) and strontium (c). Transition strains are compared to the transition strains of the ordered supercells discussed in Section 5.1.2.

a dopant concentration of 25% would have a superstructure in which every fourth calcium layer is, instead, the dopant (Figure 53(b)).

In the following sections, we will investigate the mechanical response of $CaKFe_4As_4$, a compound known to have this layered superstructure, to gain insight into the potential responses of these materials. Then we investigate the mechanical response of ordered superstructures formed by doping $CaFe_2As_2$ with either barium or strontium.

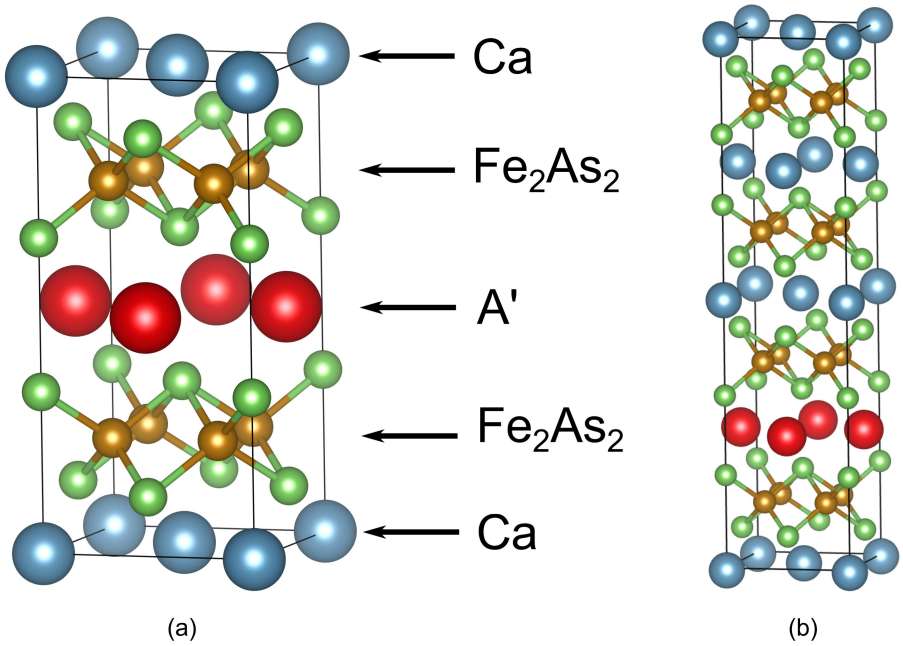

Figure 53: (a) The structure of $CaKFe_4As_4$ has a modified $ThCr_2Si_2$-type crystal structure where every other layer of calcium atoms is replaced by a layer of A' atoms, which in this case, are potassium atoms. This is the preferred structure for $BaCaFe_4As_4$ and $SrCaFe_4As_4$, which will be discussed in following sections. (b) In the layered superstructure containing 25% dopant, every fourth calcium layer is, instead, a layer of dopant.

Mechanical Response of $CaKFe_4As_4$

A compound with an example of an ordered superstructure which has garnered interest in recent years is $CaKFe_4As_4$. This compound has a $ThCr_2Si_2$-type derived structure. Unlike pure $CaFe_2As_2$ or pure KFe_2As_2, every other A layer is composed of a different element. The ordering of this structure can be seen in Figure 53. It has been described in the literature that $CaKFe_4As_4$ exhibits a “half-collapsed" phase under pressure [166]. This terminology is derived from the idea that the collapse occurs across the calcium layers, but not across the potassium layers, since the distance across potassium layers is greater than the distance across calcium layers. While this is true in a sense, this phenomenon, is not associated with a “half-collapse" of the magnetic moments. Upon collapse, like $CaFe_2As_2$, all magnetic moments vanish (Figure 54(a)). This does result in a discontinuity in the stress-strain response, as the stress in the crystal decreases after the collapse.

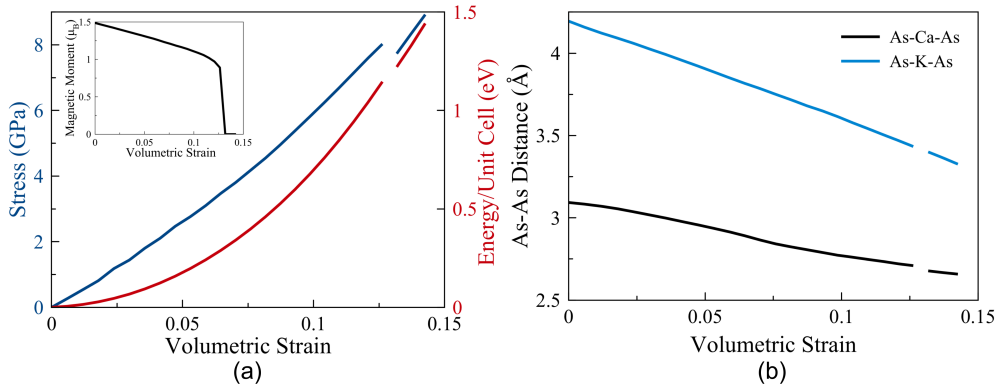

Figure 54: (a) The hydrostatic compression of $CaKFe_4As_4$ exhibits a magnetic collapse at approximately 12.5% volumetric strain, which is associated with a small crystal collapse. (b) The distance drop during the collapse between arsenic atoms across calcium planes is roughly the same as those across potassium planes.

However, while the vertical distance between arsenic atoms does drop suddenly, there isn't a significant difference in the magnitudes of the drops across calcium and potassium (Figure 54(b)). That is, the crystal doesn't collapse about the calcium plane *more* than it collapses about the potassium plane. Upon collapse, the drop in the arsenic-arsenic distances are 0.032 Å and 0.033 Å about the calcium planes and the potassium planes, respectively.

While the compression of $CaKFe_4As_4$ does not reveal a true "half-collapse," it does show a magnetic collapse which is significantly different from the response of pure $CaFe_2As_2$. With this in mind, superstructures with layered ordering were investigated for alloys of $CaFe_2As_2$ and barium or strontium in the following section.

Superstructures of $CaFe_2As_2$ Doped with Barium or Strontium

The superstructures inspired by the ordering of $CaKFe_4As_4$ are potential structures for alloys of $CaFe_2As_2$ and barium or strontium. These superstructures have ordered layers of A-type planes, where specific concentrations of dopant can be achieved by varying the frequency of the dopant plane. Superstructures of 50% barium or strontium concentration simply take the $CaKFe_4As_4$ crystal structure. Other concentrations can be achieved by repeating this structure in the c-direction, and replacing an appropriate number of calcium layers with layers of the dopant metal. For example, in a 25% strontium structure, $SrCa_3Fe_8As_8$, every fourth calcium layer would be a strontium

layer instead and the repeatable c-axis distance would be twice as tall as a conventional $CaFe_2As_2$ unit cell (Figure 53(b)).

Superstructures of 25%, 50% and 75% dopant (both barium and strontium) were constructed and compressed hydrostatically. The resulting stress-strain curves, along with those of their parent compounds, can be seen in Figure 55. The mechanical response of the 50% dopant superstructures

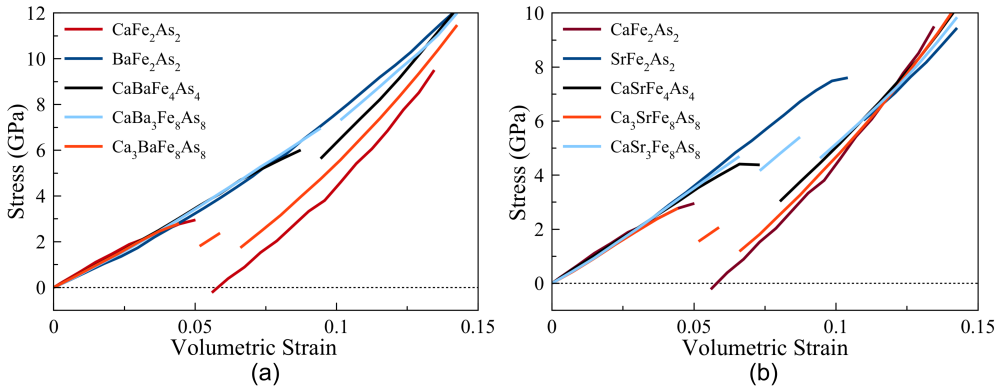

Figure 55: Compression of the superstructures of $CaFe_2As_2$ alloyed with barium (a) and strontium (b) shows an interesting evolution of mechanical properties with dopant concentration. The 25% dopant superstructures of both species exhibit two crystal collapses, while both 50% dopant superstructures exhibit only one crystal collapse. The 75% strontium superstructure also shows two crystal collapse points, while the 75% barium superstructure only shows one in our range of investigated compression.

to hydrostatic compression is similar to the response of $CaKFe_4As_4$. The structures experienced a single structural collapse (Figure 55), which is associated with a collapse of the magnetic moments (Figure 56).

The 25% and 75% superstructures exhibited responses with multiple phase transitions. Both the 25% and 75% strontium superstructures, as well as the 25% barium superstructure exhibited two magnetic and structural transitions. These stress-strain responses are shown in Figure 55, and the evolution of the magnetic moments are shown in Figure 56. It is clear that this superstructure ordering provides different material properties than the random alloying described in Section 5.1.1. However, which is more likely to form? We address this question in the following section.

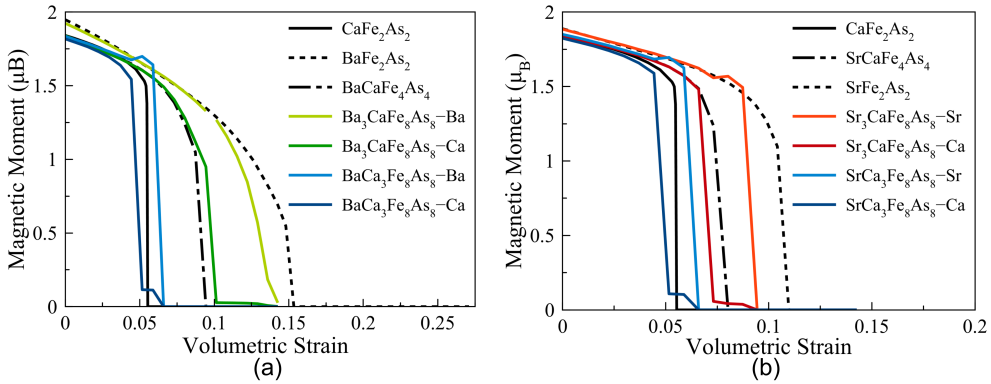

Figure 56: The evolution of the magnetic moments in the superstructures alloyed with barium (a) and strontium (b). Superstructures containing either 25% or 75% alloyed species have multiple magnetic collapses.

5.1.3 Ordering Preference

These two possible orderings, random and layered, were investigated for their possible mechanical responses. However, do these alloys have a preference to either order? An energetic preference to one of these orderings could potentially render the other ordering very difficult to synthesize. To answer this question, all structures, SQSs and superstructures, were investigated for their thermodynamic stability. Their cohesive energies (per formula unit) we calculated and plotted against composition. The resulting convex hulls can be seen in Figure 57. None of the SQSs lie

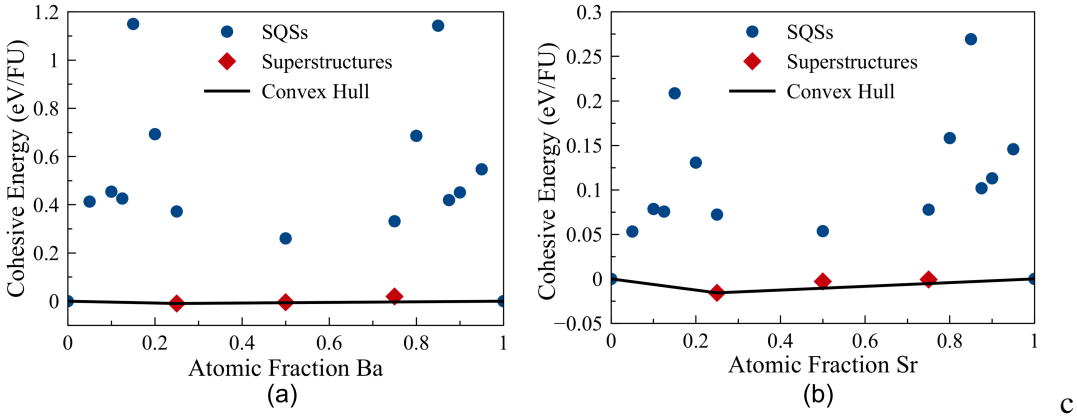

Figure 57: The convex hulls of $Ba_xCa_{(1-x)}Fe_2As_2$ (a) and $Sr_xCa_{(1-x)}Fe_2As_2$ (b) show that no SQS is thermodynamically stable. However, it is feasible that random structures with Sr could be quenched in. Some superstructures, on the other hand, do indeed lie on the convex hull. A formula unit (FU) is 5 atoms: 1 Ca/Ba/Sr, 2 Fe, and 2 As.

on the convex hull, which means that energetically speaking, these structures are unlikely to form. The best strontium-doped SQSs are approximately 0.05 eV/Formula Unit above the convex hull, while the best barium-doped SQSs are roughly 0.3 eV/Formula Unit above. These structures are not very far off of the convex hull and perhaps are stable at finite temperature. At 0 K, the layered superstructures do lie either on the convex hull, or very close. Thus, it is clear that these alloys favor order at low temperatures. However, they may have an order-disorder transition at higher temperatures. Further investigations are needed to understand the possible coupling between temperature and order.

5.1.4 Discussion

The possible mechanical properties of $CaFe_2As_2$ doped with strontium or barium were investigated through DFT compression simulations. Both randomly-ordered structures and layered superstructures were studied for various concentrations of dopant. Our results show that the transition stresses and strains of randomly-ordered alloys can be controlled directly by the concentration of dopants (Figure 52).

The magnetic behavior of the superstructures (shown in Figure 56) is particularly exciting. Unlike the 50% structures, including $CaKFe_4As_4$, where all iron atoms lose their magnetic moments simultaneously, Half of the irons lose their magnetism in the first collapse, while the second half of irons lose their magnetism in the second half. This implies that the superstructure *truly* forms a "half-collapsed" intermediate phase, before fully collapsing. This is exemplified in Figure 58(b), which highlights the distances between iron atoms in the crystal. First, it is interesting to note that the initial distances between irons is mostly a function of which species of atom is between them. Regardless of overall composition, irons straddling a calcium have nearly the same distance in an unstressed state, the same goes for strontium.

Upon first collapse, it can be seen that the irons entirely surrounded by calcium layers collapse, exhibiting a great shortening of distance. Meanwhile, the iron atoms straddling the strontium layer hardly experience a change in distance, and the distance between iron atoms across a calcium

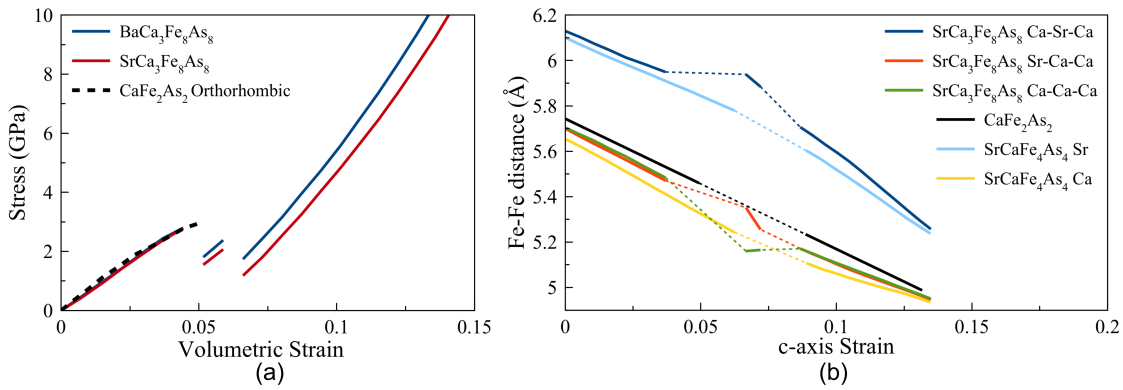

Figure 58: (a) Both the barium and strontium 25% dopant superstructures exhibit similar compression responses with two phase changes. The initial phases of both superstructures have very similar mechanical responses to each other, and orthorhombic $CaFe_2As_2$. (b) The Fe–Fe distances highlight where in the crystal, and at which strains, does each collapse occur.

layer which borders a strontium layer decrease slightly. At the point of second collapse, the Fe–Fe distance across the strontium layer decreases intensely while the distance between the iron atoms embedded in calcium layers remains roughly the same across the collapse. Again the third set of iron atoms get closer together during the phase change, however not as intensely as the irons which, at this point, are actively part of the collapse. The evolution of this collapse is depicted in Figure 59.

This behavior can be explained, in part, by the evolution of magnetic moments in the crystal. In the first phase change, the iron atoms embedded in calcium layers collapse, and also lose their magnetic moments. This can be understood since in their immediate vicinity (only nearest neighboring layers), the crystal may appear to be pure $CaFe_2As_2$. The iron atoms surrounding the strontium layer keep their magnetic moments until the second collapse, where they experience their large jump in distance. In the intermediate phase, there are calcium layers bordered on one side with magnetic iron cages, and on the other side with nonmagnetic iron cages. This intermediate phase can most appropriately be described as “half collapsed."

The multiple phase-change points may be useful in designing and tuning the response of these materials. A crystal with 3 (or more) preferred lengths may be used as a solid-state actuator. Furthermore, the Néel temperatures of all three materials differ. In contrast to $CaFe_2As_2$, which

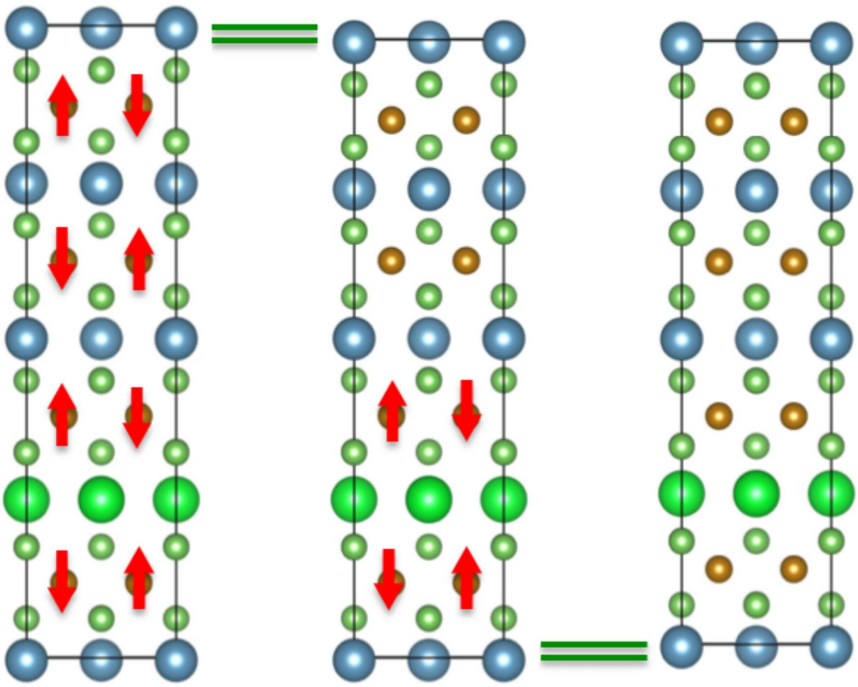

Figure 59: Under loading, the 25% superstructure (a) will collapse, both structurally and magnetically in the Ca-rich regions of the crystal (b).

has a Néel temperature of 170 K, $BaFe_2As_2$ has a Néel temperature of 143 K [169] and $SrFe_2As_2$ has a Néel temperature of 190 K [170].

If these random structures can be somehow be quenched in, then these materials can perhaps be tuned by manipulating the concentration in processing. This should not be out of the realm of possibility considering that other metastable compounds with similar cohesive energies are often stabilized in quenching. For example, cementite, an iron-carbon compound which is a major phase within steels, has a cohesive energy of 0.051 eV/atom [171]. This is comparable to the cohesive energies of the $Sr_xCa_{(1-x)}Fe_2As_2$ structures (Figure 57(b)) and, to a lesser extent, those of the $Ba_xCa_{(1-x)}Fe_2As_2$ structures (Figure 57(a)).

However, it does seem that the crystal has a high affinity to forming an ordered structure. This can be easily rationalized by geometry. We can think of the crystal as layers of 2-dimensional structures, the [Fe_2As_2 cages and the A-atom layers. Having a mix of A atoms in each layer breaks the planar nature of those structures. Since the A atoms species have different atomic radii, the new

topography of a mixed A layer should induce some inherent strain on the cage layers. Meanwhile, the more ordered superstructures do not have this problem. Since the entirety of each layer is composed of only one atom (and thus one atomic radius), the layers' thicknesses do not vary in-plane. Furthermore, at least come combinations of these superstructure alloys are predicted to be thermodynamically stable, while the others are very close to the convex hull. This suggests that these crystal structures can transcend theory and be studied experimentally.

To what extent does the long range ordering of the superstructures play a role in the mechanical response? Would reducing the number of dopant layers increase the number of magnetic collapse steps, and thus phase transitions? Could we engineer these materials to respond to c-axis stress in an accordion-like fashion? Alternatively, the cage layers may not be affected by atoms beyond the next cage layer. In that scenario, perhaps two magnetic collapse steps is the maximum possible.

5.2 Cobalt Doping of $CaFe_2As_2$

Doping of $ThCr_2Si_2$ crystals for the purpose of increasing the superconductive critical temperature is an active area of research. One common approach is to electron-dope these materials by replacing some of the iron atoms with cobalt atoms, which has been investigated in $BaFe_2As_2$ [47, 172, 173]. These studies have found that cobalt doping decreases the c-axis length of the $BaFe_2As_2$ crystal. The effects of cobalt doping on the collapsed state of $CaFe_2As_2$ have yet to be investigated; however, compression experiments of doped $CaFe_2As_2$ are pending. How does the presence of cobalt affect the mechanical response of $CaFe_2As_2$?

To investigate this, simulation cells of cobalt-doped $CaFe_2As_2$ with varying cobalt concentrations were constructed and relaxed. Their c-axis lengths and magnetism were evaluated to gauge crystal collapse. The various concentrations of cobalt were obtained through the use of both special quasirandom structures (SQSs) and cobalt-doped supercells were constructed. SQSs with Co concentrations of 50%, 25%, and 10% were studied, and supercells of 50%, 6.25% (1/16) and 3.125% (1/32) were studied. The SQSs were used to gain insight to a high concentrations with a random ordering, while the supercells at low concentrations were presumed to be sufficient in

simulating low concentrations. This presumption was made based on the performance of SQSs in the study of defected $LaRu_2P_2$ (Section 4.1).

The supercells of high concentration (50%) were constructed to represent possible ordering of the cobalt and iron atoms which were not captured by the SQSs. Special attention was given to these orderings because of the magnetic ordering of the iron atoms (and the doping cobalt atoms). While cobalt is also a magnetic element, it has one more valence electron than iron, and its presence has been shown to disrupt the magnetism of ternary iron arsenides [47]. The Co–Fe orderings simulated with supercells were the checkered pattern, the horizontal layer pattern, the vertical stripe pattern, and the vertical layer pattern. The resulting order of the SQS was the horizontal stripe pattern. These orderings have been previously visualized in the discussion of magnetic ordering in $CaFe_2As_2$ (Section 3.1.1) and can be seen in Figure 11.

Relaxation of these SQSs and supercells provided the magnetic moments of the iron/cobalt atoms and the relaxed c-axes of the structures. This can be seen in Figure 60. At cobalt concentrations above 6.25% the crystal is nonmagnetic, and the c-axis lengths are shortened (consistently below 10.75 Å). At concentrations at or below 6.25%, the magnetism is not eliminated, and the c-axis lengths are near that of pure $CaFe_2As_2$ (approximately 11.5 Å).

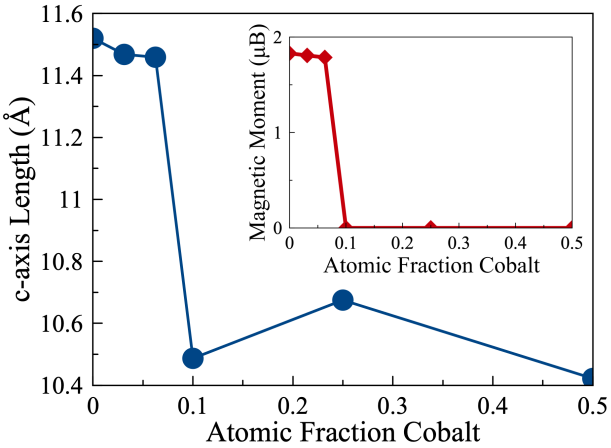

Figure 60: The c-axis lengths and magnetic moment of the Fe/Co atoms (insert) of $CaFe_2As_2$ doped with cobalt as a function of cobalt concentration. Concentrations as low as 10% collapse the crystal along the c-axis.

5.2.1 Discussion

Doping $CaFe_2As_2$ with cobalt in place of iron has a significant effect on the magnetic and structural properties of the crystal. The presence of cobalt in concentrations higher than 6.25% destabilizes the magnetic ordering of the iron and cobalt atoms. This destabilization is accompanied by a crystal collapse, which is apparent due to the decrease in c-axis length. It is interesting to note that this transition to a collapsed state occurs at similar concentrations to that of vacancies in $LaRu_2P_2$ (Section 4.1.4).

Chapter 6

Cleavage Simulations of $ThCr_2Si_2$-type Crystals

The emergence of pseudo-elasticity in $ThCr_2Si_2$-type crystals, along with their fatigue resistance, has led to their potential as structural materials. As such, it is important to investigate the inelastic behavior, such as fracture and plastic deformation, of these materials. As intermetallic compounds, materials with the $ThCr_2Si_2$-type crystal structure are expected to be relatively brittle [26].

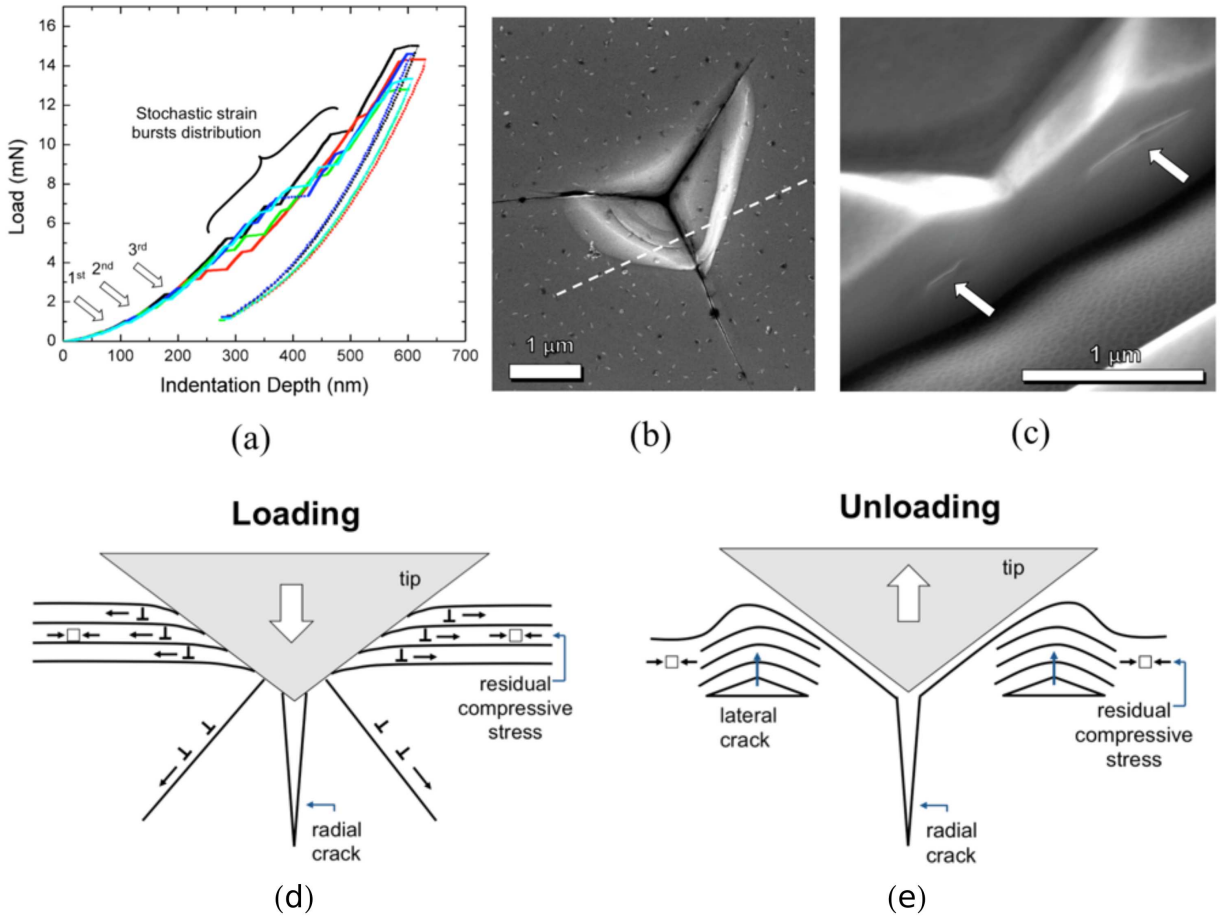

Figure 61: (a) A load-displacement curve with indentation depth of 600 nm. SEM images of (b) an indent before FIB milling and of (c) lateral cracks for the indentation depth, 600 nm. Schematics of the indentation deformation and fracture for (d) loading and (e) unloading conditions. Reproduced from Frawley et al. [26].

While loading along the c-axis results in a pseudo-elastic mechanical response, experimental investigations of $CaFe_2As_2$ have shown that in off-axis compression, the crystal easily slips along its (001) plane via micaceous deformation [18]. Micaceous deformation occurs when a material has a predisposition to shearing and fracturing on a favored crystallographic plane [174]. This highlights that this crystal structure is highly anisotropic, and off-axis loading can result in inelastic deformation. Since these crystals are potential replacements for conventional SMAs, knowledge of their fatigue life and failure mechanisms would assist designing with these materials.

Nanoindentation experiments are ideal for investigating inelastic deformation, since these experiments can induce fracture and plastic deformation simultaneously. From such experiments, we can observe a material's propensity to slip and fracture, and which deformation mode might be activated during loading. Nanoindentation investigations of $CaFe_2As_2$ by Frawley et al. revealed both radial and lateral cracking in the material. This cracking was also associated with strain bursts. Upon loading (Figure 61(a)), several instances of strain bursts were observed. Unloading revealed both radial cracking (Figure 61(b)) and lateral cracking along the walls of the nanoindent (Figure 61(c)). This is due to the accumulation of lateral compressive stress and dislocations within the crystal during loading (Figure 61(d)), which upon unloading, contribute to the lateral cracking between layers. Lateral cracking is a common phenomenon in thin films or multi-layered materials [175, 176], which makes sense considering the layered nature of $ThCr_2Si_2$-type crystals.

6.1 Cleavage Simulations of $CaFe_2As_2$

The plastic deformation observed in the nanoindentation experiments was complimented by DFT cleavage simulations. Simulations of the cleaving of $CaFe_2As_2$ were performed to investigate the energy and stress required to fracture the material, and which planes would be the easiest to fracture during loading. This was motivated, in part, by the observations of micaceous deformation in crystals of $CaFe_2As_2$ [18]. To complement nanoindentation experiments, cleavage simulations were performed to investigate the potential planes upon which this fracture may occur.

6.1.1 Methodology

Cleavage simulations of $CaFe_2As_2$ were performed by first creating a periodic simulation cell which is large in the direction normal to the cleavage plane, and sufficiently periodic in the cleavage plane. A rift is created along the cleavage plane, between the desired layers upon which the crystal is being cleaved. The atoms on one side of the rift are incrementally shifted away from the atoms on the other side. This creates an incrementally widened vacuum space between the two sides of the crystal. As this rift is widened, the energy of the simulation cell is computed without relaxing the ionic positions. This setup is depicted in Figure 62(a). The energy increases as the gap is widened until the two surfaces created are sufficiently far such that they no longer interact. At this point, the cleavage energy has asymptotically approached the energy of two free surfaces.

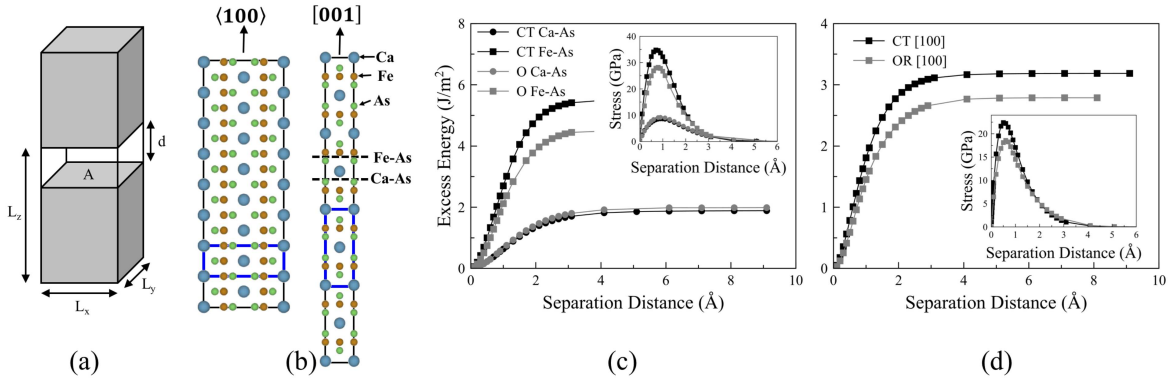

Figure 62: (a) Depiction of the simulation method performed to calculate the cleavage response. (b) $CaFe_2As_2$ was cleaved on the (100) plane (left) and the (001) plane (right). (c) Energy and stress response of $CaFe_2As_2$ cleaved on the (001) plane in the orthorhombic phase (OR) and collapsed tetragonal phase (CT), with both possible chemistries. (d) Energy and stress response to cleavage on the (100) plane for both the OR and CT phases.

Cleavage of $CaFe_2As_2$ was simulated on two planes, (100) and (001). On the (001) plane, two cleavage chemistries were investigated, the Ca–As chemistry, and the Fe–As chemistry (Figure 62(b)), while on the (100) plane, there is only one possible chemistry to cleave. Furthermore, cleavage on these planes and chemistries was investigated for both the orthorhombic and collapsed-tetragonal phases of $CaFe_2As_2$. While the (100) and (010) planes of the orthorhombic phase aren't

exactly equivalent, as they are in the collapsed-tetragonal phase, they are very similar planes crystallographically speaking. The (100) direction has a slightly wider spacing than the (010) plane, and thus we would expect this to be the easier plane for cleavage to occur.

The simulation cells for the (001) cleavage were 1×1 unit cells in-plane and 4 unit cells in the direction normal to the cleavage plane. Simulation cells for (100) cleavage were, again, 1×1 unit cells in-plane, and 8 unit cells in the direction normal to the cleavage plane. The Monkhorst-Pack k-point mesh was $9 \times 9 \times 1$ for (001) cleavage, and was scaled appropriately for the (100) simulation cells. Since the simulation cell was very long in the direction normal to the cleavage plane, only one k-space integration point is needed in that direction.

6.1.2 Results and Discussion

Cleavage on the (001) plane (Figure 62(c)) with Ca–As chemistry is significantly favorable when compared to the Fe–As chemistry. This agrees with our intuition, since cleaving the Fe–As chemistry plane breaks the cage, while the Ca–As chemistry plane is between layers. The resulting cleavage energy of the Ca–As (001) plane is very similar for both the orthorhombic and collapsed-tetragonal phases, 1.99 J/m^2 and 1.89 J/m^2, respectively. These cleavage energies are both less than half of those from the Fe–As plane, which are 4.57 J/m^2 and 5.51 J/m^2, respectively. Likewise, the stresses required to cleave on the Ca–As (001) planes is roughly a third of those required to cleave on the Fe–As (001). The stresses to cleave the Ca–As chemistry are 9.21 GPa and 8.61 GPa for the orthorhombic and collapsed-tetragonal phases, respectively. The stresses required to cleave the Fe–As chemistry are 28.2 GPa and 34.8 GPa for the orthorhombic and collapsed-tetragonal phases respectively. Interestingly, while the energy and stress required to cleave on the Ca–As plane is slightly easier for the collapsed-tetragonal phase than orthorhombic, cleaving the Fe–As plane is easier in the orthorhombic phase.

There is only one possible chemistry for the (100) plane. Cleavage on this plane was simulated for both the orthorhombic and collapsed tetragonal phases. In a similar fashion to the (001) plane, the collapsed tetragonal phase is harder to cleave than the orthorhombic phase (Figure 62(d)). The

(100) cleavage energy of the collapsed-tetragonal phase is 3.19 J/m^2 while for the orthorhombic phase, it is 2.79 J/m^2. The stress required to cleave the collapsed-tetragonal phase (22.4 GPa) is greater than the stress required to cleave the orthorhombic phase (18.6 GPa).

Overall, the (100) plane requires a higher stress to cleave, and results in a higher cleavage energy, than the (001) Ca–As plane, regardless of phase. However, the Fe–As (001) planes require the most energy and highest stress to cleave. Thus, fracture on this chemistry is highly unlikely. We can expect that fracture is likely to occur with the (001) planes, which is consistent with the observed micaceous deformation [18].

6.2 Cleavage Simulations of $LaRu_2P_2$

If $LaRu_2P_2$ is to be used as either a solid-state actuator, or a pseudo-elastic mechanical component, knowledge of its fracture mechanisms is important. In this vein, similar cleavage simulations were performed for $LaRu_2P_2$ crystals. The methodology performed in Section 6.1.1 was repeated for $LaRu_2P_2$. However, since $LaRu_2P_2$ does not have a collapsed-tetragonal phase which can be stabilized at zero applied stress, only cleavage of the tetragonal phase was investigated. Cleavage on both the (100) and (001) planes were simulated. We know from the cleavage simulations of $CaFe_2As_2$, in addition to intuition, the (001) plane is far more likely to cleave between layers of lanthanum and phosphorus than layers of phosphorus and ruthenium. To confirm, cleavage on both (001) plane chemistries was simulated.

The results of these simulations can be seen in Figure 63. The simulation results reveal similar trends to cleavage in $CaFe_2As_2$. Cleavage on the La–P (001) plane has the lowest required stress (13.7 GPa) and the lowest cleavage energy (2.74 J/m^2). Cleavage on the Ru–P chemistry of the (001) plane has the highest required stress (42.9 GPa) and the highest cleavage energy (6.63 J/m^2). Cleavage on the {100} planes requires a stress of 29.8 GPa, which is in between the two (001) chemistries. The resulting cleavage energy of the {100} plane is 4.25 J/m^2, which is also between the energies of the two (001) chemistries.

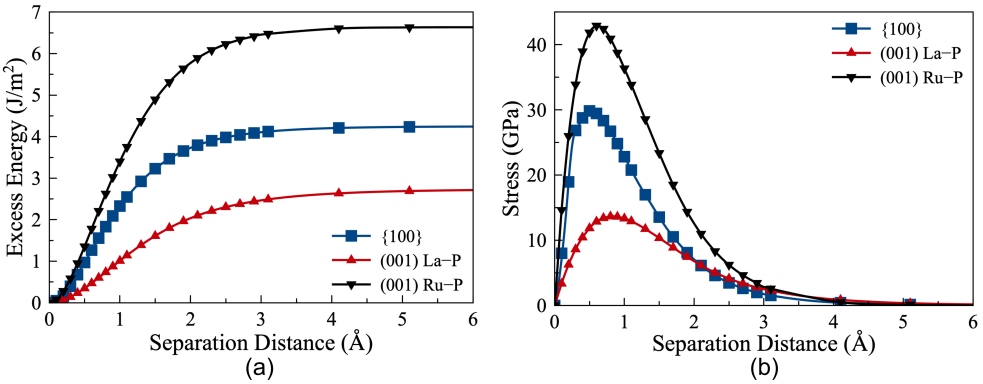

Figure 63: (a) Energy-displacement and (b) stress-displacement curves for cleave simulations of $LaRu_2P_2$. The cleavage energy and max stress are significantly lower for cleave on the (001) planes than on the {100} planes. This is congruent with the results from $CaFe_2As_2$, and make makes sense considering the layered nature of the $ThCr_2Si_2$-type crystals.

This preference is similar to that shown in the $CaFe_2As_2$ cleavage simulations. Like $CaFe_2As_2$, we would expect $LaRu_2P_2$ to cleave on its (001) planes. Specifically, the La–P chemistry (001) plane is the easiest to cleave. If nanoindentation experimental studies were to be conducted on $LaRu_2P_2$, it would be reasonable to expect fracturing similar to that observed in $CaFe_2As_2$ nanoindentation experiments. Furthermore, it is also likely for $LaRu_2P_2$ to deform micaceously under off-axis loading conditions. Knowledge of these failure mechanisms and anisotropic deformation behavior can help future engineers better design with these materials.

Chapter 7

Conclusions and Future Work

As is the nature of most investigations, more new questions presented themselves than were answered. This study exhibited exhausting depth in certain areas but left several fields open to more scientific investigation. The unique mechanical properties of $ThCr_2Si_2$-type crystal lend themselves to a wide range of future uses. The properties appear to be tunable through defects and processing, as well as through overall composition and superstructure. Furthermore, the unique origins of the shape-memory effects of these crystals allows for increased fatigue resistance over conventional SMAs.

Compression along the c-axis of these crystals often results in a phase change, which facilitates a pseudo-elastic response. If the material's ground state is magnetic, as is $CaFe_2As_2$'s, then the phase change can be both magnetic and structural. Nonmagnetic compounds with this crystal structure, such as $LaRu_2P_2$, can also exhibit a phase change. These phase changes can be more subtle; in $LaRu_2P_2$, the phase change is characteristically second-order, as some elastic constants are discontinuous in strain.

The pseudo-elastic responses of $CaFe_2As_2$ and $LaRu_2P_2$ were modeled by continuum-scale composite models built with data from DFT simulations of single unit cells. The pseudo-elastic response of $CaFe_2As_2$ is a result of a phase transition between two distinct magnetic phases, while in $LaRu_2P_2$, there is no distinct phase change. Strain-controlled DFT simulations gave more complete insight into the mechanical response of these compounds than previously reported in literature. The stress-strain predictions of the models agreed with experimental stress-strain trends of $CaFe_2As_2$ and $LaRu_2P_2$ but differ modestly in the magnitude of the stress response. For a given compound and loading control mechanism, the models predict similar transition strains for hydrostatic and uniaxial compression states. This indicates that c-axis strain is the controlling factor of the pseudo-elastic response.

Point defects in $ThCr_2Si_2$-type crystals were shown to reduce the characteristic pseudo-elastic softening in the stress-strain response. Here, these defects and their effects were well-studied in $LaRu_2P_2$ and $CaFe_2As_2$. From experimental observations and models, it is likely that these defects segregate to form pure and defected regions, allowing for a blending of mechanical properties between the pure response and the defected response. Ruthenium and phosphorus vacancies at high concentrations were shown to induce crystal collapse. The presence of these point defects, most importantly, vacancies, can be used to tune the response of the sample, and may be a point of control for future material designers.

The alloying of the $CaFe_2As_2$, $BaFe_2As_2$, and $SrFe_2As_2$ in a random distribution reveals a nearly linear evolution of phase-transition properties between the parent compounds. However, they are not thermodynamically stable, as they are off the convex hull. Ordered superstructures of alternating layers of A-type atoms, similar to the crystal structure of $CaKFe_4As_4$, are more likely to lie on the convex hull. The mechanical responses of these structures can exhibit multiple phase changes with cascading magnetic collapses.

It is the hope of this work that this analysis has opened the door to a new tunability of these materials. Future materials engineers may expand on some of the principles exposed and explored in this work to design small-scale solid-state actuators with tuned $ThCr_2Si_2$-type crystals. A great deal more research is required to bridge the gap between this theoretical study and practical application. The following sections highlight some of the next areas of research in this investigation.

7.1 Mechanical Response of Alloyed $ThCr_2Si_2$-type Superstructures

The alloys of $CaFe_2As_2$, $BaFe_2As_2$, and $SrFe_2As_2$ have been predicted by this work to have interesting and perhaps valuable mechanical properties. While inspiring, there are some areas that need more in-depth investigation.

7.1.1 Uniaxial Compression

Thus far the investigations of the mechanical responses of these alloys, both ordered and disordered, have been limited to hydrostatic stress. We have been able to show that the primary consideration for crystal collapse is c-axis strain, and thus similar mechanical responses occur to both hydrostatic and uniaxial loadings. However, since these materials, especially the superstructures, are particularly sensitive in their c-axis strain, it would be useful to investigate them in uniaxial stress states.

7.1.2 Predicting the Pseudo-Elastic Response

Analysis of the mechanical responses of single unit cells of the alloyed superstructures revealed interesting mechanical response, especially in regards to the critical stresses and strains of their phase changes. However, how do these differences in phase change properties translate into the mechanical response of a sample of these materials? In a similar manner to the pure 1:2:2 compounds, the pseudo-elastic response can be constructed from energetic data of the possible phases. These models will predict how samples of these materials would respond in actual compression experiments. This will be especially interesting for superstructures which exhibit a third "half-collapsed" phase. Compression data from each phase can be gleaned from DFT simulations. The models will predict the mechanical response by minimizing the appropriate thermodynamic potential (internal energy for displacement-control, enthalpy for load-control).

7.1.3 Can These Compounds Be Fabricated?

The evolution of mechanical properties with concentration is distinctly different when the structures are ordered vs. when they are disordered. While some of the ordered structures lie on the convex hull, all of the disordered structures are off the convex hull. The disordered structures are only off the convex hull by a few hundreths of an electron volt per formula unit in Sr alloys, and a few tenths of an electron volt per formula unit in Ba alloys. While strictly speaking, these are

not thermodynamically stable, it may be possible top quench in these structures. Whether these structures can be fabricated is a point that should be investigated in the future.

Likewise, the ordered superstructures, which are predicted to be thermodynamically stable, have yet to be synthesized experimentally. The synthesis of these structures should also be investigated. While theoretically expected to exist, synthesis may prove to be tricky. Once these crystals can be grown or synthesized, their mechanical properties can be investigated experimentally. Both hydrostatic and uniaxial microcompression tests can be performed to observe how these materials behave. These results can be compared to our theoretical predictions.

7.1.4 Investigations of Superstructures with Different Alloy Concentrations

In this work, it was proposed that alloys of $CaFe_2As_2$ and either $BaFe_2As_2$ or $SrFe_2As_2$ would energetically prefer to form layered superstructures. Compression of these superstructures revealed that alloys of 25% and 75% strontium concentration, and alloys of 25% barium concentration, exhibited two cascading magnetic collapses. These arose from the apparently different character of two regions of the crystal. Lower concentrations of the alloyed compound, in the superstructure ordering, would have a repeatable structure which was even longer in the c direction. Would this produce more distinct regions in the crystal, with perhaps more cascading magnetic collapses and phase changes? Alternatively, is there a limit to the number of distinct regions possible? This would all depend on how important long-range order is in the crystal. In $SrCa_3Fe_8As_8$, two [Fe_2As_2] cages are sandwiched between calcium layers, while two cages are flanked by a calcium layer on one side, and the strontium layer on the other. If only the nearest A-type layer is important, than two cages would be part of a $CaFe_2As_2$ region, while the other two layers would comprise a $SrCaFe_2As_2$ region. However, if longer-range effects are important, a taller crystal with a different concentration would have more distinct regions.

7.1.5 Effects of Temperature on the Mechanical Response

Another interesting question that presents itself in this work is: how do these superstructures respond to temperature? The individual compounds, $BaFe_2As_2$, $CaFe_2As_2$, and $SrFe_2As_2$

have all been reported to have different Néel temperatures. The Néel temperature of $CaFe_2As_2$ is 170 K [16]; the Néel temperature of $BaFe_2As_2$ is 143 K [169], and the Néel temperature of $SrFe_2As_2$ is 190 K [170]. As evidenced by the predicted cascading magnetic collapse, the iron atoms in these superstructures have distinct character. It would be interesting to see if different regions of these structures have different Néel temperatures. Furthermore, it would be interesting to see how the mechanical responses of these structures evolve with temperature, especially through the temperature transition regions between Néel temperatures (if it is revealed that the material has multiple Néel temperatures).

7.2 Plasticity in $ThCr_2Si_2$-type Crystals

Studies of $ThCr_2Si_2$-type crystals have revealed their potential plastic deformation mechanisms and their micaceous nature. However, crystal plasticity of these crystals has only been computationally investigated in $CaFe_2As_2$ [18]. Nanoindentation studies have been performed in other compounds, such as $BaFe_2As_2$ [177]. Along these lines, there are several areas of research which could be investigated in the near future.

7.2.1 Study of Slip Mechanisms in $LaRu_2P_2$

To round out the study of plasticity in $LaRu_2P_2$, micaceous behavior, and slip on the (001) planes should be investigated. Slip along this plane can be simulated via in-plane displacement and generalized stacking fault (GSF) surfaces, as well as curves of $\langle a \rangle$-type slip, can be generated. These investigations would shed light onto the potentially active slip mechanisms in $LaRu_2P_2$, and the strength it has in off-axis loading.

7.2.2 Studies of Plasticity in Other Compounds

As the battery of research into the mechanical properties of compounds with the $ThCr_2Si_2$-type crystal structure accumulates, more information on the plasticity of these compounds will prove useful. Cleavage simulations, as well as GSF surfaces and curves can be computed for other

$ThCr_2Si_2$-type compounds as they are explored for their pseudo-elastic properties. Furthermore, the plasticity of the alloyed superstructures can also be studied. Since there are more complicated chemistries involved in those structures, it is likely that some (001) planes slip more easily than others.

Bibliography

[1] Marianne Rotter, Marcus Tegel, and Dirk Johrendt. Superconductivity at 38 K in the iron arsenide ($Ba_{1-x}K_x$)Fe_2As_2. *Physical Review Letters*, 101(10):107006, 2008.

[2] Chen Gen-Fu, Li Zheng, Li Gang, Hu Wan-Zheng, Dong Jing, Zhou Jun, Zhang Xiao-Dong, Zheng Ping, Wang Nan-Lin, and Luo Jian-Lin. Superconductivity in hole-doped ($Sr_{1-x}K_x$)Fe_2As_2. *Chinese Physics Letters*, 25(9):3403, 2008.

[3] MS Torikachvili, SL Bud?ko, N Ni, and PC Canfield. Effect of pressure on the structural phase transition and superconductivity in ($Ba_{1-x}K_x$)Fe_2As_2 ($x = 0$ and 0.45) and $SrFe_2As_2$ single crystals. *Physical Review B*, 78(10):104527, 2008.

[4] Z Ban and M Sikirica. The crystal structure of ternary silicides ThM_2Si_2 (M = Cr, Mn, Fe, Co, Ni and Cu). *Acta Crystallographica*, 18(4):594–599, 1965.

[5] P Villars Pearson's Handbook and Desk Edition. Crystallographic data for intermetallic phases. *Amsterdam: ASM International*, 1997.

[6] WB Pearson. The most populous of all crystal structure types−the tetragonal $BaAl_4$ structure. *Journal of Solid State Chemistry*, 56(3):278–287, 1985.

[7] Frank Steglich, J Aarts, CD Bredl, W Lieke, D Meschede, W Franz, and H Schäfer. Superconductivity in the presence of strong pauli paramagnetism: $CeCu_2si_2$. *Physical Review Letters*, 43(25):1892, 1979.

[8] W Jeitschko, R Glaum, and L Boonk. Superconducting $LaRu_2P_2$ and other alkaline earth and rare earth metal ruthenium and osmium phosphides and arsenides with $ThCr_2Si_2$ structure. *Journal of Solid State Chemistry*, 69(1):93–100, 1987.

[9] Pan Zhang and Hui-fei Zhai. Superconductivity in 122-type pnictides without iron. *Condensed Matter*, 2(3):28, 2017.

[10] RN Shelton, HF Braun, and E Musick. Superconductivity and relative phase stability in 1:2:2 ternary transition metal silicides and germanides. *Solid State Communications*, 52(9):797–799, 1984.

[11] Yu-Zhong Zhang, Hem C Kandpal, Ingo Opahle, Harald O Jeschke, and Roser Valentí. Microscopic origin of pressure-induced phase transitions in the iron pnictide superconductors AFe_2As_2: An ab-initio molecular dynamics study. *Physical Review B*, 80(9):094530, 2009.

[12] Baoxuan Li, Pengchao Lu, Jianzhong Liu, Jian Sun, Sheng Li, Xiyu Zhu, and Hai-Hu Wen. Pressure induced enhancement of superconductivity in $LaRu_2P_2$. *Scientific Reports*, 6:24479, 2016.

[13] Neda Foroozani, Jinhyuk Lim, James Schilling, Roxanna Fotovat, Chong Zheng, and Roald Hoffmann. Hydrostatic high-pressure studies to 25 GPa on the model superconducting pnictide $LaRu_2P_2$. In *Journal of Physics: Conference Series*, volume 500, page 032007. IOP Publishing, 2014.

[14] Yoichi Kamihara, Takumi Watanabe, Masahiro Hirano, and Hideo Hosono. Iron-based layered superconductor $La[O_{1-x}F_x]FeAs$($x = 0.05$–0.12) with $T_c = 26$ K. *Journal of the American Chemical Society*, 130(11):3296–3297, 2008.

[15] JJ Ying, YJ Yan, RH Liu, XF Wang, AF Wang, M Zhang, ZJ Xiang, and XH Chen. Isotropic superconductivity in $LaRu_2P_2$ with the $ThCr_2Si_2$-type structure. *Superconductor Science and Technology*, 23(11):115009, 2010.

[16] PC Canfield, SL Bud'ko, N Ni, A Kreyssig, AI Goldman, RJ McQueeney, MS Torikachvili, DN Argyriou, G Luke, and W Yu. Structural, magnetic and superconducting phase transitions in $CaFe_2As_2$ under ambient and applied pressure. *Physica C: Superconductivity*, 469(9):404–412, 2009.

[17] R Hoffman and C Zheng. Making and breaking bonds in the solid state: The $ThCr_2Si_2$ structure. *The Journal of Physical Chemistry*, 89:4175–4181, 1985.

[18] John T Sypek, Christopher R Weinberger, Sriram Vijayan, Mark Aindow, Sergey L Bud'ko, Paul C Canfield, and Seok-Woo Lee. Superelastic and micaceous deformation in the intermetallic compound $CaFe_2As_2$. *Scripta Materialia*, 141:10–14, 2017.

[19] Gil Drachuck, Aashish Sapkota, Wageesha T Jayasekara, Karunakar Kothapalli, Sergey L Bud'ko, Alan I Goldman, Andreas Kreyssig, and Paul C Canfield. Collapsed tetragonal phase transition in $LaRu_2P_2$. *Physical Review B*, 96(18):184509, 2017.

[20] Milan Tomić, Harald O Jeschke, Rafael M Fernandes, and Roser Valentí. In-plane uniaxial stress effects on the structural and electronic properties of $BaFe_2As_2$ and $CaFe_2As_2$. *Physical Review B*, 87(17):174503, 2013.

[21] Kazuyuki Matsubayashi, Naoyuki Katayama, Kenya Ohgushi, Atsushi Yamada, Koji Munakata, Takehiko Matsumoto, and Yoshiya Uwatoko. Intrinsic properties of AFe_2As_2 (A = Ba, Sr) single crystal under highly hydrostatic pressure conditions. *Journal of the Physical Society of Japan*, 78(7):073706, 2009.

[22] JK Dong, SY Zhou, TY Guan, H Zhang, YF Dai, X Qiu, XF Wang, Y He, XH Chen, and SY Li. Quantum criticality and nodal superconductivity in the FeAs-based superconductor KFe_2As_2. *Physical review letters*, 104(8):087005, 2010.

[23] SW Zhang, L Ma, YD Hou, J Zhang, T-L Xia, GF Chen, JP Hu, GM Luke, and W Yu. A 75 s NMR study of single crystals of the heavily overdoped pnictide superconductors $Ba_{(1-x)}K_xFe_2As_2$($x = 0.7$ and 1). *Physical Review B*, 81(1):012503, 2010.

[24] WC Li, JJ Feng, MH Qin, YL Xie, ZB Yan, XT Jia, and J-M Liu. Phase transitions in classical biquadratic Heisenberg model for strained iron pnictides. *Journal of Applied Physics*, 117(17):17E302, 2015.

[25] Jun Zhao, DT Adroja, Dao-xin Yao, R Bewley, Shiliang Li, XF Wang, G Wu, XH Chen, Jiangping Hu, and Pengcheng Dai. Spin waves and magnetic exchange interactions in $CaFe_2As_2$. *Nature Physics*, 5(8):555, 2009.

[26] Keara G Frawley, Ian Bakst, John T Sypek, Sriram Vijayan, Christopher R Weinberger, Paul C Canfield, Mark Aindow, and Seok-Woo Lee. A nanoindentation study of the plastic deformation and fracture mechanisms in single-crystalline $CaFe_2As_2$. *JOM*, pages 1–7, 2018.

[27] Filip Ronning, T Klimczuk, Eric D Bauer, H Volz, and Joe D Thompson. Synthesis and properties of $CaFe_2As_2$ single crystals. *Journal of Physics: Condensed Matter*, 20(32):322201, 2008.

[28] N Ni, S Nandi, A Kreyssig, AI Goldman, ED Mun, SL Bud'ko, and PC Canfield. First-order structural phase transition in $CaFe_2As_2$. *Physical Review B*, 78(1):014523, 2008.

[29] RS Dhaka, Rui Jiang, S Ran, Sergey L Bud'ko, Paul C Canfield, Bruce N Harmon, Adam Kaminski, Milan Tomić, Roser Valentí, and Yongbin Lee. Dramatic changes in the electronic structure upon transition to the collapsed tetragonal phase in $CaFe_2As_2$. *Physical Review B*, 89(2):020511, 2014.

[30] Milan Tomić, Roser Valentí, and Harald O Jeschke. Uniaxial versus hydrostatic pressure-induced phase transitions in $CaFe_2As_2$ and $BaFe_2As_2$. *Physical Review B*, 85(9):094105, 2012.

[31] Xiangyang Huang, Graeme J. Ackland, and Karin M. Rabe. Crystal structures and shape-memory behaviour of NiTi. *Nature Materials*, 2003.

[32] K Enami, T Tomie, Khandros LG, and S Nenno. Deformation behaviour of Ni–Al L10 (3R) martensite. *Transactions of the Japan Institute of Metals*, 22(5):357–366, 1981.

[33] S Miyazaki, S Kimura, K Otsuka, and Y Suzuki. The habit plane and transformation strains associated with the martensitic transformation in Ti-Ni single crystals. *Scripta metallurgica*, 18(9):883–888, 1984.

[34] Kazuhiro Otsuka and Clarence Marvin Wayman. *Shape memory materials*. Cambridge university press, 1999.

[35] Thomas W Duerig, KN Melton, and D Stöckel. *Engineering aspects of shape memory alloys*. Butterworth-Heinemann, 2013.

[36] N B Morgan and Cm Friend. A review of shape memory stability in NiTi alloys. *J. Phys. IV France*, 11:8–325, 2001.

[37] Clarence Marvin Wayman. *Introduction to the crystallography of martensitic transformations*. Macmillan, 1964.

[38] AG Khachaturyan. Theory of structural phase transformations in solids. *John Willey, New York, NY*, 17(1983):1733–1743, 1983.

[39] Milton S Torikachvili, Sergey L Bud'ko, Ni Ni, and Paul C Canfield. Pressure induced superconductivity in $CaFe_2As_2$. *Physical review letters*, 101(5):057006, 2008.

[40] A Kreyssig, MA Green, Y Lee, GD Samolyuk, P Zajdel, JW Lynn, SL Bud'ko, MS Torikachvili, N Ni, S Nandi, et al. Pressure-induced volume-collapsed tetragonal phase of $CaFe_2As_2$ as seen via neutron scattering. *Physical Review B*, 78(18):184517, 2008.

[41] Nicola Colonna, Gianni Profeta, Alessandra Continenza, and Sandro Massidda. Structural and magnetic properties of $CaFe_2As_2$ and $BaFe_2As_2$ from first-principles density functional theory. *Physical Review B*, 83(9):094529, 2011.

[42] Michael Widom and Khandker Quader. First-principles study of $CaFe_2As_2$ under pressure. *Physical Review B*, 88(4):045117, 2013.

[43] John T Sypek, Hang Yu, Keith J Dusoe, Gil Drachuck, Hetal Patel, Amanda M Giroux, Alan I Goldman, Andreas Kreyssig, Paul C Canfield, Sergey L Bud'ko, Christopher R. Weinberger, and Seok-Woo Lee. Superelasticity and cryogenic linear shape memory effects of $CaFe_2As_2$. *Nature Communications*, 8(1):1083, 2017.

[44] A.I. Goldman, A. Kreyssig, K. Prokeš, D.K. Pratt, D.N. Argyriou, J.W. Lynn, S. Nandi, S.A.J. Kimber, Y. Chen, Y.B. Lee, G. Samolyuk, S.J. Leão, S.L. Poulton, N. Bud'ko, P.C.

Canfield, B.N. Harmon, and R.J. McQueeny. Lattice collapse and quenching of magnetism in $CaFe_2As_2$ under pressure: A single-crystal neutron and X-ray diffraction investigation. *Physical Review B*, 79(2):024513, 2009.

[45] G Wu, H Chen, T Wu, YL Xie, YJ Yan, RH Liu, XF Wang, JJ Ying, and XH Chen. Different resistivity response to spin-density wave and superconductivity at 20 K in $Ca_{1-x}Na_xFe_2As_2$. *Journal of Physics: Condensed Matter*, 20(42):422201, 2008.

[46] N Haberkorn, B Maiorov, IO Usov, M Weigand, W Hirata, S Miyasaka, S Tajima, N Chikumoto, K Tanabe, and Leonardo Civale. Influence of random point defects introduced by proton irradiation on critical current density and vortex dynamics of $Ba(Fe_{0.925}Co_{0.075})_2As_2$ single crystals. *Physical Review B*, 85(1):014522, 2012.

[47] Athena S Sefat, Rongying Jin, Michael A McGuire, Brian C Sales, David J Singh, and David Mandrus. Superconductivity at 22 K in Co-doped $BaFe_2As_2$ crystals. *Physical review letters*, 101(11):117004, 2008.

[48] Neeraj Kumar, R Nagalakshmi, R Kulkarni, PL Paulose, AK Nigam, SK Dhar, and A Thamizhavel. Anisotropic magnetic and superconducting properties of $CaFe_{2-x}Co_xAs_2$ ($x = 0, 0.06$) single crystals. *Physical Review B*, 79(1):012504, 2009.

[49] J-Ph Reid, MA Tanatar, XG Luo, H Shakeripour, N Doiron-Leyraud, Ni Ni, SL Bud'ko, PC Canfield, R Prozorov, and Louis Taillefer. Nodes in the gap structure of the iron arsenide superconductor $Ba(Fe_{1-x}Co_x)_2As_2$ from c-axis heat transport measurements. *Physical Review B*, 82(6):064501, 2010.

[50] Kazutaka Kudo, Keita Iba, Masaya Takasuga, Yutaka Kitahama, Jun-ichi Matsumura, Masataka Danura, Yoshio Nogami, and Minoru Nohara. Emergence of superconductivity at 45 K by lanthanum and phosphorus co-doping of $CaFe_2As_2$. *Scientific reports*, 3, 2013.

[51] Yasuyuki Nakajima, Toshihiro Taen, Yuji Tsuchiya, Tsuyoshi Tamegai, Hisashi Kitamura, and Takeshi Murakami. Suppression of the critical temperature of superconduct-

ing $Ba(Fe_{1-x}Co_x)_2As_2$ by point defects from proton irradiation. *Physical Review B*, 82(22):220504, 2010.

[52] Y Nakajima, Y Tsuchiya, T Taen, T Tamegai, S Okayasu, and M Sasase. Enhancement of critical current density in Co-doped $BaFe_2As_2$ with columnar defects introduced by heavy-ion irradiation. *Physical Review B*, 80(1):012510, 2009.

[53] David Sholl and Janice A Steckel. *Density functional theory: a practical introduction*. John Wiley & Sons, 2011.

[54] Feliciano Giustino. *Materials modelling using density functional theory: properties and predictions*. Oxford University Press, 2014.

[55] Christopher R Weinberger and Garritt J Tucker. *Multiscale Materials Modeling for Nanomechanics*, volume 245. Springer, 2016.

[56] Georg Kresse and Jürgen Furthmüller. Efficiency of ab-initio total energy calculations for metals and semiconductors using a plane-wave basis set. *Computational Materials Science*, 6(1):15–50, 1996.

[57] Georg Kresse and Jürgen Furthmüller. Efficient iterative schemes for ab-initio total-energy calculations using a plane-wave basis set. *Physical Review B*, 54(16):11169, 1996.

[58] Ramamurti Shankar. *Principles of quantum mechanics*. Springer Science & Business Media, 2012.

[59] Walter Kohn and Lu Jeu Sham. Self-consistent equations including exchange and correlation effects. *Physical review*, 140(4A):A1133, 1965.

[60] Walter Wolf and Peter Herzig. First-principles investigations of transition metal dihydrides, TH_2: T= Sc, Ti, V, Y, Zr, Nb; energetics and chemical bonding. *Journal of Physics: Condensed Matter*, 12(21):4535, 2000.

[61] John P Perdew, Kieron Burke, and Matthias Ernzerhof. Generalized gradient approximation made simple. *Physical Review Letters*, 77(18):3865, 1996.

[62] V Milman, B Winkler, and MIJ Probert. Stiffness and thermal expansion of ZrB_2: an ab-initio study. *Journal of Physics: Condensed Matter*, 17(13):2233, 2005.

[63] John P Perdew, Adrienn Ruzsinszky, Jianmin Tao, Viktor N Staroverov, Gustavo E Scuseria, and Gábor I Csonka. Prescription for the design and selection of density functional approximations: More constraint satisfaction with fewer fits. *The Journal of Chemical Physics*, 123(6):062201, 2005.

[64] C Fonseca Guerra, JG Snijders, G te Velde, and EJ Baerends. Towards an order-n dft method. *Theoretical Chemistry Accounts*, 99(6):391–403, 1998.

[65] PJ De Pablo, F Moreno-Herrero, J Colchero, J Gómez Herrero, P Herrero, AM Baró, Pablo Ordejón, José M Soler, and Emilio Artacho. Absence of dc-conductivity in λ-DNA. *Physical review letters*, 85(23):4992, 2000.

[66] Peter E Blöchl. Projector augmented-wave method. *Physical Review B*, 50(24):17953, 1994.

[67] Hendrik J Monkhorst and James D Pack. Special points for Brillouin-zone integrations. *Physical Review B*, 13(12):5188, 1976.

[68] Richard Phillips Feynman. Forces in molecules. *Physical Review*, 56(4):340, 1939.

[69] William H Press, Saul A Teukolsky, William T Vetterling, and Brian P Flannery. *Numerical recipes 3rd edition: The art of scientific computing*. Cambridge university press, 2007.

[70] Jonathan Richard Shewchuk et al. An introduction to the conjugate gradient method without the agonizing pain, 1994.

[71] Reeves Fletcher and Colin M Reeves. Function minimization by conjugate gradients. *The computer journal*, 7(2):149–154, 1964.

[72] Colin W Glass, Artem R Oganov, and Nikolaus Hansen. USPEX—evolutionary crystal structure prediction. *Computer Physics Communications*, 175(11):713–720, 2006.

[73] Andriy O Lyakhov, Artem R Oganov, Harold T Stokes, and Qiang Zhu. New developments in evolutionary structure prediction algorithm USPEX. *Computer Physics Communications*, 184(4):1172–1182, 2013.

[74] Artem R Oganov, Yanming Ma, Colin W Glass, and Mario Valle. Evolutionary crystal structure prediction: overview of the USPEX method and some of its applications. *Psi-k Newsletter*, 84:142–171, 2007.

[75] Alex Zunger, S-H Wei, LG Ferreira, and James E Bernard. Special quasirandom structures. *Physical Review Letters*, 65(3):353, 1990.

[76] A. van de Walle. Multicomponent multisublattice alloys, nonconfigurational entropy and other additions to the Alloy Theoretic Automated Toolkit. *Calphad*, 33:266–278, 2009.

[77] A. van de Walle, M. D. Asta, and G. Ceder. The Alloy Theoretic Automated Toolkit: A user guide. *Calphad*, 26:539–553, 2002.

[78] A. van de Walle and G. Ceder. Automating first-principles phase diagram calculations. *J. Phase Equilib.*, 23:348–359, 2002.

[79] A. van de Walle and M. D. Asta. Self-driven lattice-model monte carlo simulations of alloy thermodynamic properties and phase diagrams. *Model. Simul. Mater. Sc.*, 10:521, 2002.

[80] A. van de Walle, P. Tiwary, M. M. de Jong, D. L. Olmsted, M. D. Asta, A. Dick, D. Shin, Y. Wang, L.-Q. Chen, and Z.-K. Liu. Efficient stochastic generation of special quasirandom structures. *Calphad*, 42:13–18, 2013.

[81] A. van de Walle. Methods for first-principles alloy thermodynamics. *JOM - J. Min. Met. Mat. S.*, 65:1523–1532, 2013.

[82] A. van de Walle. A complete representation of structure-property relationships in crystals. *Nat. Mater.*, 7:455–458, 2008.

[83] A. van de Walle and D. Ellis. First-principles thermodynamics of coherent interfaces in samarium-doped ceria nanoscale superlattices. *Phys. Rev. Lett.*, 98:266101, 2007.

[84] E. Cockayne and A. van de Walle. Building effective models from scarce but accurate data: Application to an alloy cluster expansion model. *Phys. Rev. B*, 81:012104, 2010.

[85] A. van de Walle, B. G. Chirranjeevi, S. Demers, Q.-J. Hong, A. Kowalski, L. Miljacic, G. S. Pomrehn, and P. Tiwary. *Ab initio* calculation of anisotropic interfacial excess free energies. *Phys. Rev. B*, 89:184101, 2014.

[86] A. van de Walle, Q.-J. Hong, S. Kadkhodaei, and R. Sun. The free energy of mechanically unstable phases. *Nature Commun.*, 6:7559, 2015.

[87] A. van de Walle, S. Kadkhodaei, R. Sun, and Q.-J. Hong. Epicycle method for elasticity limit calculations. *Phys. Rev. B*, 95:144113, 2017.

[88] R. Sun and A. van de Walle. Automating impurity-enhanced antiphase boundary energy calculations from *ab initio* monte carlo. *Calphad*, 53:20, 2016.

[89] A. van de Walle, R. Sun, Q.-J. Hong, and S. Kadkhodaei. Software tools for high-throughput calphad from first-principles data. *Calphad*, 58:70, 2017.

[90] Shaofan Li and Gang Wang. *Introduction to micromechanics and nanomechanics*. World Scientific Publishing Company, 2008.

[91] Siavouche Nemat-Nasser and Muneo Hori. *Micromechanics: overall properties of heterogeneous materials*, volume 37. Elsevier, 2013.

[92] Christopher R. Weinberger, Wei Cai, and David M. Barnett. Lecture notes–elasticity of microscopic structures. *ME340–Stanford University*, 2005.

[93] Vyacheslav Ivanovich Lebedev. Quadratures on a sphere. *USSR Computational Mathematics and Mathematical Physics*, 16(2):10–24, 1976.

[94] VI Lebedev. Spherical quadrature formulas exact to orders 25–29. *Siberian Mathematical Journal*, 18(1):99–107, 1977.

[95] VI Lebedev. A quadrature formula for the sphere of 59th algebraic order of accuracy. *Russian Academy of Sciences-Doklady Mathematics-AMS Translation*, 50(2):283–286, 1995.

[96] Vyacheslav Ivanovich Lebedev and DN Laikov. A quadrature formula for the sphere of the 131st algebraic order of accuracy. In *Doklady. Mathematics*, volume 59, pages 477–481. MAIK Nauka/Interperiodica, 1999.

[97] AI Goldman, DN Argyriou, B Ouladdiaf, T Chatterji, A Kreyssig, S Nandi, N Ni, SL Bud'ko, PC Canfield, and RJ McQueeney. Lattice and magnetic instabilities in $CaFe_2As_2$: A single-crystal neutron diffraction study. *Physical Review B*, 78(10):100506, 2008.

[98] Johannes Ferber, Yu-Zhong Zhang, Harald O Jeschke, and Roser Valenti. Analysis of spin-density wave conductivity spectra of iron pnictides in the framework of density functional theory. *Physical Review B*, 82(16):165102, 2010.

[99] Sinéad M Griffin and Nicola A Spaldin. A density functional theory study of the influence of exchange-correlation functionals on the properties of FeAs. *Journal of Physics: Condensed Matter*, 29(21):215604, 2017.

[100] SL Dudarev, GA Botton, SY Savrasov, CJ Humphreys, and AP Sutton. Electron-energy-loss spectra and the structural stability of nickel oxide: An LSDA+U study. *Physical Review B*, 57(3):1505, 1998.

[101] Richard FW Bader. *Atoms in molecules*. Wiley Online Library, 1990.

[102] Walter Gordy and WJ Orville Thomas. Electronegativities of the elements. *The Journal of Chemical Physics*, 24(2):439–444, 1956.

[103] Axel D Becke and Kenneth E Edgecombe. A simple measure of electron localization in atomic and molecular systems. *The Journal of Chemical Physics*, 92(9):5397–5403, 1990.

[104] Miroslav Kohout, Frank Richard Wagner, and Yuri Grin. Electron localization function for transition-metal compounds. *Theoretical Chemistry Accounts*, 108(3):150–156, 2002.

[105] Richard Dronskowski and Peter E Bloechl. Crystal orbital Hamilton populations (COHP): energy-resolved visualization of chemical bonding in solids based on density-functional calculations. *The Journal of Physical Chemistry*, 97(33):8617–8624, 1993.

[106] Volker L Deringer, Andrei L Tchougréeff, and Richard Dronskowski. Crystal orbital Hamilton population (COHP) analysis as projected from plane-wave basis sets. *The Journal of Physical Chemistry A*, 115(21):5461–5466, 2011.

[107] Stefan Maintz, Volker L Deringer, Andrei L Tchougréeff, and Richard Dronskowski. Lobster: A tool to extract chemical bonding from plane-wave based dft. *Journal of computational chemistry*, 37(11):1030–1035, 2016.

[108] Frank H Allen, Olga Kennard, David G Watson, Lee Brammer, A Guy Orpen, and Robin Taylor. Tables of bond lengths determined by X-ray and neutron diffraction. part 1. bond lengths in organic compounds. *Journal of the Chemical Society, Perkin Transactions 2*, (12):S1–S19, 1987.

[109] Robert D Shannon. Revised effective ionic radii and systematic studies of interatomic distances in halides and chalcogenides. *Acta crystallographica section A: crystal physics, diffraction, theoretical and general crystallography*, 32(5):751–767, 1976.

[110] Qi Guo, Bo-Jin Pan, Jia Yu, Bin-Bin Ruan, Dong-Yun Chen, Xiao-Chuan Wang, Qing-Ge Mu, Gen-Fu Chen, and Zhi-An Ren. Superconductivity at 7.8 K in the ternary $LaRu_2As_2$ compound. *Science bulletin*, 61(12):921–924, 2016.

[111] MA Hadi, MS Ali, SH Naqib, and AKMA Islam. New ternary superconducting compound $LaRu_2As_2$: Physical properties from density functional theory calculations. *Chinese Physics B*, 26(3):037103, 2017.

[112] Philip JW Moll, Jakob Kanter, Ross D McDonald, Fedor Balakirev, Peter Blaha, Karlheinz Schwarz, Zbigniew Bukowski, Nikolai D Zhigadlo, Sergiy Katrych, Kurt Mattenberger, et al. Quantum oscillations of the superconductor $LaRu_2P_2$: Comparable mass enhancement $\lambda \approx 1$ in Ru and Fe phosphides. *Physical Review B*, 84(22):224507, 2011.

[113] S Blackburn, B Prévost, M Bartkowiak, O Ignatchik, A Polyakov, T Förster, M Côté, G Seyfarth, C Capan, Z Fisk, et al. Fermi-surface topology of the iron pnictide $LaFe_2P_2$. *Physical Review B*, 89(22):220505, 2014.

[114] Simon Blackburn. Analyse des propriétés électroniques de supraconducteurs à l'aide de la théorie de la fonctionnelle de la densité. 2014.

[115] Jack Kiefer. Sequential minimax search for a maximum. *Proceedings of the American Mathematical Society*, 4(3):502–506, 1953.

[116] C Ma, HX Yang, HF Tian, HL Shi, JB Lu, ZW Wang, LJ Zeng, GF Chen, NL Wang, and JQ Li. Microstructure and tetragonal-to-orthorhombic phase transition of AFe_2As_2 (A=Sr, Ca) as seen via transmission electron microscopy. *Physical Review B*, 79(6):060506, 2009.

[117] Dale E Newbury and Nicholas WM Ritchie. Is scanning electron microscopy/energy dispersive X-ray spectrometry (SEM/EDS) quantitative? *Scanning*, 35(3):141–168, 2013.

[118] Seok-Woo Lee, Seung Min Han, and William D Nix. Uniaxial compression of fcc Au nanopillars on an MgO substrate: The effects of prestraining and annealing. *Acta Materialia*, 57(15):4404–4415, 2009.

[119] Julia R Greer, Warren C Oliver, and William D Nix. Size dependence of mechanical properties of gold at the micron scale in the absence of strain gradients. *Acta Materialia*, 53(6):1821–1830, 2005.

[120] Ian N Bakst, John T Sypek, James R Neilson, Seok-Woo Lee, and Christopher R Weinberger. Modeling pseudo-elastic behavior in small-scale $ThCr_2Si_2$-type crystals. *Computational Materials Science*, 150:86–95, 2018.

[121] Athena S Sefat, Michael A McGuire, Rongying Jin, Brian C Sales, David Mandrus, Filip Ronning, ED Bauer, and Yurij Mozharivskyj. Structure and anisotropic properties of $BaFe_{2-x}Ni_xAs_2$ ($x = 0$, 1, and 2) single crystals. *Physical Review B*, 79(9):094508, 2009.

[122] Rohan Mishra, Oscar D Restrepo, Patrick M Woodward, and Wolfgang Windl. First-principles study of defective and nonstoichiometric Sr_2FeMoO_6. *Chemistry of Materials*, 22(22):6092–6102, 2010.

[123] Andrius Merkys, Antanas Vaitkus, Justas Butkus, Mykolas Okulič-Kazarinas, Visvaldas Kairys, and Saulius Gražulis. COD:: CIF:: Parser: an error-correcting CIF parser for the Perl language. *Journal of applied crystallography*, 49(1):292–301, 2016.

[124] Saulius Gražulis, Andrius Merkys, Antanas Vaitkus, and Mykolas Okulič-Kazarinas. Computing stoichiometric molecular composition from crystal structures. *Journal of applied crystallography*, 48(1):85–91, 2015.

[125] Saulius Gražulis, Adriana Daškevič, Andrius Merkys, Daniel Chateigner, Luca Lutterotti, Miguel Quiros, Nadezhda R Serebryanaya, Peter Moeck, Robert T Downs, and Armel Le Bail. Crystallography Open Database (COD): an open-access collection of crystal structures and platform for world-wide collaboration. *Nucleic acids research*, 40(D1):D420–D427, 2011.

[126] Saulius Gražulis, Daniel Chateigner, Robert T Downs, AFT Yokochi, Miguel Quirós, Luca Lutterotti, Elena Manakova, Justas Butkus, Peter Moeck, and Armel Le Bail. Crystallography Open Database–an open-access collection of crystal structures. *Journal of Applied Crystallography*, 42(4):726–729, 2009.

[127] Robert T Downs and Michelle Hall-Wallace. The American Mineralogist crystal structure database. *American Mineralogist*, 88(1):247–250, 2003.

[128] Xianxin Wu, Congcong Le, Yi Liang, Shengshan Qin, Heng Fan, and Jiangping Hu. Effect of As-chain layers in $CaFeAs_2$. *Physical Review B*, 89(20):205102, 2014.

[129] P Manuel, LC Chapon, IS Todorov, DY Chung, J-P Castellan, S Rosenkranz, R Osborn, P Toledano, and MG Kanatzidis. Incommensurate spin-density wave and magnetic lock-in transition in $CaFe_4As_3$. *Physical Review B*, 81(18):184402, 2010.

[130] Stefano Curtarolo, Wahyu Setyawan, Shidong Wang, Junkai Xue, Kesong Yang, Richard H Taylor, Lance J Nelson, Gus LW Hart, Stefano Sanvito, Marco Buongiorno-Nardelli, et al. Aflowlib. org: A distributed materials properties repository from high-throughput ab initio calculations. *Computational Materials Science*, 58:227–235, 2012.

[131] Artem R Oganov and Colin W Glass. Crystal structure prediction using *ab-initio* evolutionary techniques: Principles and applications. *The Journal of chemical physics*, 124(24):244704, 2006.

[132] Artem R Oganov, Yanming Ma, Andriy O Lyakhov, Mario Valle, and Carlo Gatti. Evolutionary crystal structure prediction as a method for the discovery of minerals and materials. *Reviews in Mineralogy and Geochemistry*, 71(1):271–298, 2010.

[133] Andriy O Lyakhov, Artem R Oganov, and Mario Valle. How to predict very large and complex crystal structures. *Computer Physics Communications*, 181(9):1623–1632, 2010.

[134] Artem R Oganov, Andriy O Lyakhov, and Mario Valle. How evolutionary crystal structure prediction works–and why. *Accounts of chemical research*, 44(3):227–237, 2011.

[135] Guangtao Wang, Xianbiao Shi, Lin Zhang, and Xia Yi. The electronic structure and magnetism of $CaFeAs_2$: First principles calculations. *Solid State Communications*, 200:61–65, 2014.

[136] AB Karki, GT McCandless, S Stadler, YM Xiong, J Li, Julia Y Chan, and R Jin. Structural and physical properties of $CaFe_4As_3$. *Physical Review B*, 84(5):054412, 2011.

[137] Anubhav Jain, Shyue Ping Ong, Geoffroy Hautier, Wei Chen, William Davidson Richards, Stephen Dacek, Shreyas Cholia, Dan Gunter, David Skinner, Gerbrand Ceder, and Kristin a. Persson. The Materials Project: A materials genome approach to accelerating materials innovation. *APL Materials*, 1(1):011002, 2013.

[138] Anubhav Jain, Geoffroy Hautier, Shyue Ong, Charles Moore, Christopher Fischer, Kristin Persson, and Gerbrand Ceder. Formation enthalpies by mixing GGA and GGA+U calculations. *Physical Review B*, 84(4):045115, July 2011.

[139] Shyue Ping Ong, Lei Wang, Byoungwoo Kang, and Gerbrand Ceder. Li-Fe-P-O_2 Phase Diagram from First Principles Calculations. *Chemistry of Materials*, 20(5):1798–1807, March 2008.

[140] Frederik Bachhuber, Jörg von Appen, Richard Dronskowski, Peer Schmidt, Tom Nilges, Arno Pfitzner, and Richard Weihrich. The extended stability range of phosphorus allotropes. *Angewandte Chemie International Edition*, 53(43):11629–11633, 2014.

[141] Ralph Walter Graystone Wyckoff. Crystal structures. 1964.

[142] RG Ross and W Hume-Rothery. High temperature X-ray metallography: I. a new debye-scherrer camera for use at very high temperatures II. a new parafocusing camera III. applications to the study of chromium, hafnium, molybdenum, rhodium, ruthenium and tungsten. *Journal of the Less Common Metals*, 5(3):258–270, 1963.

[143] Marion Dewees, Janet S Henderson, Marie C Osmon, and AC Lawson. Superconductivity of (La, Th)Ru_2, (La, Th)Os_2 and La(Ru, Os)$_2$ alloys. *Journal of the Less Common Metals*, 86:L9–L11, 1982.

[144] Jian Meng and Yufang Ren. Studies on the electrical properties of rare earth monophosphides. *Journal of Solid State Chemistry*, 95(2):346–351, 1991.

[145] W Wichelhaus, M Schulze Nahrup, et al. On the chemistry and structural chemistry of phosphides and polyphosphides. xi. lanthanum phosphide LaP_2; representation, structure and properties. *Journal of Inorganic and General Chemistry*, 412(3):193–201, 1975.

[146] Xuean Chen, Liping Zhu, and Shoji Yamanaka. High-pressure synthesis and structural characterization of three new polyphosphides, α-SrP_3, BaP_8, and LaP_5. *Journal of Solid State Chemistry*, 173(2):449–455, 2003.

[147] Wilhelm Biltz, Hans-Joachim Ehrhorn, and Karl Meisel. Contribution to systematic kinship theory. 85. ü about the systems osmium / phosphorus and ruthenium / phosphorus. *Journal of Inorganic and General Chemistry*, 240(2):117–128, 1939.

[148] A Kjekshus, T Rakke, and AF Andresen. Compounds with marcasite type crystal-structure. 12. structural data for RuP_2, $RuAs_2$, $RuSb_2$, OsP_2, $OsAs_2$, and $OsSb_2$. *ACTA CHEMICA SCANDINAVICA SERIES A-PHYSICAL AND INORGANIC CHEMISTRY*, 31(4):253–259, 1977.

[149] DJ Braun and W Jeitschko. U about polyphosphides of chromium, manganese, ruthenium, and osmium, synthesis and crystal structure of RuP_4 and OsP_4. *Journal of Inorganic and General Chemistry*, 445(1):157–166, 1978.

[150] Ertuğrul Karaca, S Karadağ, HM Tütüncü, GP Srivastava, and S Uğur. First-principles investigation of superconductivity in the body-centred tetragonal. *Philosophical Magazine*, 96(19):2059–2073, 2016.

[151] HM Tütüncü, Ertuğrul Karaca, and GP Srivastava. Electron-phonon superconductivity in the filled skutterudites $LaRu_4P_{12}$, $LaRu_4As_{12}$, and $LaPt_4Ge_{12}$. *Physical Review B*, 95(21):214514, 2017.

[152] Wei Cai and William D Nix. *Imperfections in Crystalline Solids*. Cambridge University Press, 2016.

[153] JR Jeffries, NP Butch, K Kirshenbaum, SR Saha, G Samudrala, ST Weir, YK Vohra, and J Paglione. Suppression of magnetism and development of superconductivity within the collapsed tetragonal phase of $Ca_{0.67}Sr_{0.33}Fe_2As_2$ under pressure. *Physical Review B*, 85(18):184501, 2012.

[154] Xiaxin Ding, Delong Fang, Zhenyu Wang, Huan Yang, Jianzhong Liu, Qiang Deng, Guobin Ma, Chong Meng, Yuhui Hu, and Hai-Hu Wen. Influence of microstructure on superconductivity in $K_xFe_{2-y}Se_2$ and evidence for a new parent phase $K_2Fe_7Se_8$. *Nature Communications*, 4:1897, may 2013.

[155] Mark D Lumsden, Andrew D Christianson, Daniel Parshall, Matthew B Stone, Stephen E Nagler, GJ MacDougall, HA Mook, K Lokshin, T Egami, DL Abernathy, et al. Two-dimensional resonant magnetic excitation in $BaFe_{1.84}Co_{0.16}As_2$. *Physical Review Letters*, 102(10):107005, 2009.

[156] C Ma, HX Yang, HF Tian, HL Shi, JB Lu, ZW Wang, LJ Zeng, GF Chen, NL Wang, and JQ Li. Microstructure and tetragonal-to-orthorhombic phase transition of AFe_2As_2 (A = Sr, Ca) as seen via transmission electron microscopy. *Physical Review B*, 79(6):060506, 2009.

[157] S Ran, SL Bud?Ko, DK Pratt, A Kreyssig, MG Kim, MJ Kramer, DH Ryan, WN Rowan-Weetaluktuk, Y Furukawa, B Roy, et al. Stabilization of an ambient-pressure collapsed tetragonal phase in $CaFe_2As_2$ and tuning of the orthorhombic-antiferromagnetic transition temperature by over 70 K via control of nanoscale precipitates. *Physical Review B*, 83(14):144517, 2011.

[158] Kari Selte, Arne Kjekshus, Jorunn Sletten, Lena Torbjörnsson, Per-Erik Werner, Ulf Junggren, Bo Lamm, and Benny Samuelsson. The Crystal Structure of FeAs., 1969.

[159] E. E. Rodriguez, C. Stock, K. L. Krycka, C. F. Majkrzak, P. Zajdel, K. Kirshenbaum, N. P. Butch, S. R. Saha, J. Paglione, and M. A. Green. Noncollinear spin-density-wave anti-

ferromagnetism in FeAs. *Physical Review B - Condensed Matter and Materials Physics*, 83(13):1–6, 2011.

[160] Bayrammurad Saparov, Claudia Cantoni, Minghu Pan, Thomas C Hogan, William Ratcliff II, Stephen D Wilson, Katharina Fritsch, Makoto Tachibana, Bruce D Gaulin, and Athena S Sefat. Complex structures of different $CaFe_2As_2$ samples. *scientific reports*, 4:4120, 2014.

[161] Ortrud Kubaschewski. *Iron?Binary phase diagrams*. Springer Science & Business Media, 2013.

[162] Tobias Stürzer, Christine Hieke, Catrin Löhnert, Fabian Nitsche, Juliane Stahl, Christian Maak, Roman Pobel, and Dirk Johrendt. Framework structures of interconnected layers in calcium iron arsenides. *Inorganic chemistry*, 53(12):6235–6240, 2014.

[163] Marcus Tegel, Marianne Rotter, Veronika Weiss, Falko M Schappacher, Rainer Pöttgen, and Dirk Johrendt. Structural and magnetic phase transitions in the ternary iron arsenides $SrFe_2As_2$ and $EuFe_2As_2$. *Journal of Physics: Condensed Matter*, 20(45):452201, 2008.

[164] L Vegard. The constitution of the mixed crystals and the filling of space of the atoms, Z. *Physik*, 5:17–26, 1921.

[165] Sergey L Bud?ko, Tai Kong, William R Meier, Xiaoming Ma, and Paul C Canfield. 57Fe Mössbauer study of stoichiometric iron-based superconductor $CaKFe_4As_4$: a comparison to KFe_2As_2 and $CaFe_2As_2$. *Philosophical Magazine*, 97(29):2689–2703, 2017.

[166] Udhara S Kaluarachchi, Valentin Taufour, Aashish Sapkota, Vladislav Borisov, Tai Kong, William R Meier, Karunakar Kothapalli, Benjamin G Ueland, Andreas Kreyssig, Roser Valentí, et al. Pressure-induced half-collapsed-tetragonal phase in $CaKFe_4As_4$. *Physical Review B*, 96(14):140501, 2017.

[167] Kazuki Iida, Motoyuki Ishikado, Yuki Nagai, Hiroyuki Yoshida, Andrew D Christianson, Naoki Murai, Kenji Kawashima, Yoshiyuki Yoshida, Hiroshi Eisaki, and Akira Iyo. Spin

resonance in the new-structure-type iron-based superconductor $CaKFe_4As_4$. *Journal of the Physical Society of Japan*, 86(9):093703, 2017.

[168] Daixiang Mou, Tai Kong, William R Meier, Felix Lochner, Lin-Lin Wang, Qisheng Lin, Yun Wu, SL Bud?ko, Ilya Eremin, Duane D Johnson, et al. Enhancement of the superconducting gap by nesting in $CaKFe_4As_4$: A new high temperature superconductor. *Physical review letters*, 117(27):277001, 2016.

[169] Q Huang, Y Qiu, Wei Bao, MA Green, JW Lynn, YC Gasparovic, T Wu, G Wu, and XH Chen. Neutron-diffraction measurements of magnetic order and a structural transition in the parent $BaFe_2As_2$ compound of FeAs-based high-temperature superconductors. *Physical Review Letters*, 101(25):257003, 2008.

[170] Jason Neal Hancock, Seyed Iman Mirzaei, J Gillett, SE Sebastian, Jérémie Teyssier, Romain Viennois, Enrico Giannini, and Dirk Van Der Marel. Strong coupling to magnetic fluctuations in the charge dynamics of iron-based superconductors. *Physical Review B*, 82(1):014523, 2010.

[171] Kristin Persson. Materials data on Fe_3C (SG:62) by materials project, 2 2016. An optional note.

[172] Jiun-Haw Chu, James G Analytis, Chris Kucharczyk, and Ian R Fisher. Determination of the phase diagram of the electron-doped superconductor $Ba(Fe_{1-x}Co_x)_2As_2$. *Physical Review B*, 79(1):014506, 2009.

[173] S Lee, J Jiang, Y Zhang, CW Bark, JD Weiss, C Tarantini, CT Nelson, HW Jang, CM Folkman, SH Baek, et al. Template engineering of Co-doped $BaFe_2As_2$ single-crystal thin films. *Nature Materials*, 9(5):397–402, 2010.

[174] Jong-Sub Lee, Maria Guimaraes, and J Carlos Santamarina. Micaceous sands: Microscale mechanisms and macroscale response. *Journal of Geotechnical and Geoenvironmental Engineering*, 133(9):1136–1143, 2007.

[175] Ryan D Jamison and Yu-Lin Shen. Delamination analysis of metal–ceramic multilayer coatings subject to nanoindentation. *Surface and Coatings Technology*, 303:3–11, 2016.

[176] TA Prikhna, SN Dub, AV Starostina, MV Karpets, T Cabiosh, and P Chartier. Mechanical properties of materials based on MAX phases of the Ti-Al-C system. *Journal of superhard materials*, 34(2):102–109, 2012.

[177] Gelson B de Souza, Francisco C Serbena, Alcione R Jurelo, Simone A da Silva, Lincoln BLG Pinheiro, Fábio T Dias, Alexandre Mikowski, Sergey L Bud'ko, Alex Thaler, and Paul C Canfield. On the determination of hardness and elastic modulus in $BaFe_2As_2$ lamellar-like material. *Journal of Materials Research*, 31(10):1413–1422, 2016.

Appendix A

Other La–Ru–P Structures Investigated

Table A1: Lattice constants and atomic positions of all the structures investigated for the convex hull which have not previously been reported.

Compound	Space Group	Lattice Constants (Å)	Atom Positions (Wyckoff Positions)
La_5Ru_2	C 1 2/c 1	$a = 16.440$	La(8f) (0.408, 0.392, 0.408)
		$b = 6.483$	La(8f) (-0.215, 0.425, 0.317)
		$c = 7.177$	La(4e) (0.000, 0.419, 0.250)
		$\beta = 84.880°$	Ru(8f) (0.389, 0.210, 0.081)
La_3Ru	P 21/n 21/m 21/a	$a = 7.155$	La(8d) (-0.329, -0.067, 0.330)
		$b = 9.830$	La(4c) (0.456, 0.250, 0.151)
		$c = 6.327$	Ru(4c) (0.120, 0.250, -0.062)
LaP_7	P 1 21/c 1	$a = 7.245$	La(4e) (0.240, 0.375, -0.128)
		$b = 12.293$	P(4e) (0.387, 0.054, -0.016)
		$c = 7.321$	P(4e) (-0.344, -0.494, -0.215)
		$\beta = 74.320°$	P(4e) (-0.037, 0.160, -0.205)
			P(4e) (-0.183, 0.382, 0.082)
			P(4e) (0.028, -0.013, -0.159)
			P(4e) (0.479, 0.219, 0.006)
			P(4e) (-0.248, 0.210, 0.070)
RuP_3	P -1	$a = 5.831$	Ru(2i) (0.227, -0.372, -0.069)
		$b = 8.026$	Ru(2i) (-0.277, 0.044, -0.367)
		$c = 5.890$	P(2i) (0.342, -0.342, -0.217)
		$\alpha = 111.262°$	P(2i) (-0.322, -0.235, 0.335)

		$\beta = 107.504°$	P(2i) (-0.317, -0.060, -0.055)
		$\gamma = 70.246°$	P(2i) (0.152, -0.085, -0.318)
			P(2i) (-0.193, -0.448, -0.471)
			P(2i) (0.171, -0.318, 0.084)
$LaRuP_2$	P 1 21/m 1	$a = 3.996$	La(2e) (0.283, 0.250, -0.229)
		$b = 3.904$	Ru(2e) (-0.250, 0.250, 0.499)
		$c = 9.786$	P(2e) (0.235, 0.250, 0.378)
		$\beta = 92.899°$	P(2e) (-0.157, 0.250, -0.005)
$LaRu_4P_3$	P 21/n 21/m 21/a	$a = 11.784$	La(4c) (-0.166, 0.250, -0.075)
		$b = 3.825$	Ru(4c) (0.343, 0.250, 0.268)
		$c = 11.279$	Ru(4c) (0.280, 0.250, -0.110)
			Ru(4c) (-0.428, 0.250, 0.033)
			Ru(4c) (0.493, 0.250, -0.196)
			P(4c) (0.379, 0.250, 0.072)
			P(4c) (0.149, 0.250, 0.285)
			P(4c) (-0.411, 0.250, -0.368)

Compound	Space group	Lattice Constants (Å)	Atom positions (Wyckoff positions)
$LaRu_2P$	P 4/n 21/m 2/m	$a = 3.990$	La(2c) (0.250, 0.250, -0.218)
		$b = 3.990$	Ru(2a) (0.750, 0.250, 0.000)
		$c = 10.521$	Ru(2b) (0.750, 0.250, 0.500)
			P(2c) (0.250, 0.250, 0.388)
$La_2Ru_3P_4$	P4m2	$a = 4.050$	La(2g) (0.000, 0.500, -0.236)
		$b = 4.050$	Ru(1c) (0.500, 0.500, 0.500)
		$c = 9.496$	Ru(1a) (0.000, 0.000, 0.000)
			Ru(1d) (0.000, 0.000, 0.500)

			P(2g) (0.000, 0.500, 0.118)
			P(2g) (0.000, 0.500,0.377)
$La_2Ru_4P_3$	P4mm	$a = 4.012$	La(1a) (0.000, 0.000, -0.016)
		$b = 4.012$	La(1b) (0.500, 0.500, -0.485)
		$c = 9.841$	Ru(2c) (0.500, 0.000, -0.249)
			Ru(2c) (0.500, 0.000, 0.251)
			P(1a) (0.000, 0.000, -0.349)
			P(1a) (0.000, 0.000, 0.364)
			P(1b) (0.500, 0.500, 0.131)
$La_1Ru_4P_4$	P 4/m 2/m 2/m	$a = 3.990$	La(1d) (0.500, 0.500, 0.500)
		$b = 3.990$	Ru(4i) (0.000, 0.500, 0.234)
		$c = 10.521$	P(2g) (0.000, 0.000, -0.340)
			P(2h) (0.500, 0.500, 0.122)
$La_3Ru_8P_8$		$a = 5.364$	La(2e) (0.000, 0.500, 0.500)
		$b = 5.364$	La(1c) (0.500, 0.500, 0.000)
		$c = 11.732$	Ru(8r) (0.248, 0.248, -0.250)
			P(2g) (0.000, 0.000, -0.358)
			P(4i) (0.000, 0.500, -0.142)
			P(2h) (0.500, 0.500, -0.354)

Appendix B

SQS Compression Results

The special quasirandom structures (SQSs) were compressed hydrostatically to simulate the mechanical response of a region of material with a high concentration of vacancies. Only SQSs with a ruthenium vacancy concentrations of 6.25% and 5% showed any softening in their response. The stress-strain responses can be seen in Figure A1 and their derivatives can be seen in Figure A2.

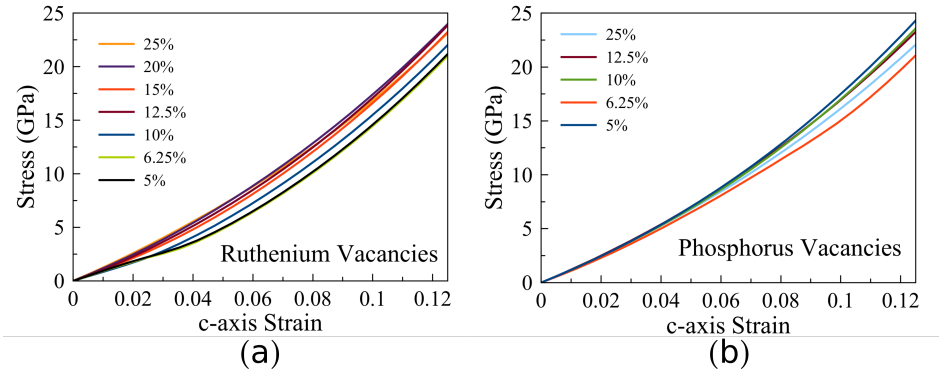

Figure A1: Hydrostatic compression stress-strain responses of SQSs at various vacancy concentrations

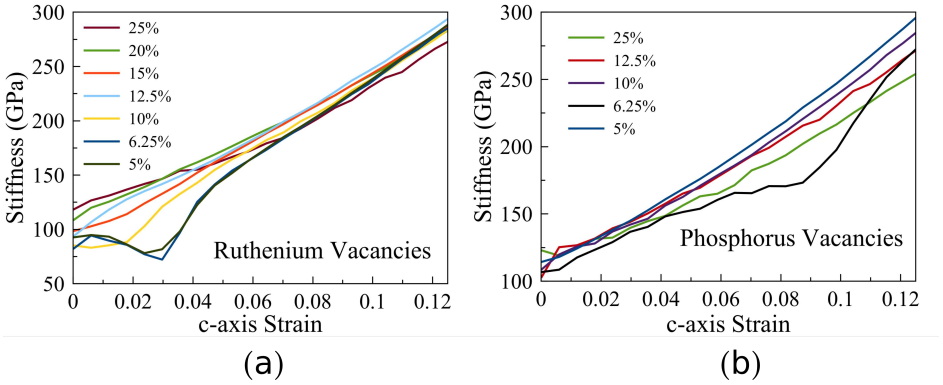

Figure A2: Stiffnesses of the SQSs computed from the derivatives of the SQS hydrostatic stress-strain curves.